UNIVERSITY OF BIRMINGHAM

SHEAR BEHAVIOUR OF CORRODED REINFORCED CONCRETE T-BEAMS REPAIRED WITH FIBRE REINFORCED POLYMER SYSTEMS

by

SHUNDE QIN

A Thesis Submitted to the University of Birmingham

for the degree of Doctor of Philosophy

School of Civil Engineering

University of Birmingham

February 2016

ABSTRACT

Annually, large amounts of money are spent on repairing corroded reinforced concrete (RC) structures. The use of de-icing salts in cold regions and/or windborne salts in coastal/marine environments are the main causes of chloride contamination of concrete. Chlorides break down the protective passive layer of iron oxides around the internal steel reinforcement and thereby facilitate the corrosion process. Internal steel shear links are susceptible to corrosion due to their proximity to the outer surfaces of concrete members. Corrosion of the internal steel shear links can have a detrimental impact on the shear strength of RC beams, and may lead to sudden and catastrophic brittle failure.

The aim of this study was to investigate the shear behaviour of uncorroded and corroded RC T-beams strengthened with carbon fibre reinforced polymer (CFRP) composites, using both physical testing and non-linear finite element (NLFE) analysis. A parametric study investigating the effect of critical parameters (corrosion level, concrete compressive strength, steel-to-CFRP shear reinforcement ratio, and shear span-to-effective depth ratio) on the shear contribution of deep embedded (DE) CFRP rods was carried out. Furthermore, both experimental and numerical results were used to investigate the accuracy of the Concrete Society Technical Report 55 (TR-55) of the DE CFRP rod shear contribution.

The physical testing results showed that the un-strengthened beams with shear link corrosion levels of 7% and 12% had shear strengths that were 11% and 14% respectively, less than the shear strength of the un-corroded un-

strengthened beam. Both the DE CFRP rods and externally bonded (EB) CFRP sheets were effective in enhancing the shear strength of tested beams, but the effectiveness of both strengthening systems decreased with increasing shear link corrosion levels. The shear strength enhancement provided by the DE CFRP rods and EB CFRP sheets decreased from 19% and 15% respectively, to 12% and 11% respectively, with the increase in shear link corrosion level from 7% to 12%. Corrosion of the shear links did not have a significant effect on T-beam stiffness. Premature debonding limited the effectiveness of the EB CFRP sheets, whereas the embedded CFRP rods did not exhibit signs of debonding and therefore showed higher effectiveness.

NLFE models were developed and validated using the experimental results. The FE –predicted shear capacity was in fair agreement with the experimental results. The mean experimental/predicted capacity ratios were 1.12, 1.13 and 1.19, with standard deviations of 0.02, 0.02 and 0.05 for the unstrengthened, DE strengthened and EB strengthened beams respectively. The FE-predicted un-cracked stiffness was higher than the experimental un-cracked stiffness. The FE models correctly captured the failure modes of the tested RC T-beams.

The parametric study was carried out only on the validated RC T-beams strengthened with DE CFRP rod models and suggested that the increase in concrete compressive strength from 25 N/mm^2 to 50 N/mm^2 did not increase the DE CFRP rod shear contribution to shear force significantly. The shear contribution of embedded CFRP rods decreased from 23.2 *kN* to 4.8 *kN* with the increase in steel-to-CFRP shear reinforcement ratio from 0.67 to 2.12. The shear contribution of embedded CFRP rods also decreased from 10.8 *kN*

to 0 *kN* with the increase in shear span-to-effective depth ratio from 2.59 to 3.70.

Comparison of the experimental and numerical results with TR-55 predictions showed that TR-55 overestimated both the experimental and numerical results, with mean predicted-to-experimental and predicted-to-numerical ratios of 1.92 and 3.96 respectively, and standard deviation of 0.84 and 2.07, respectively. TR-55 does not consider the effects of concrete compressive strength and shear span-to-effective depth ratio.

As a matter of interest to owners, managers, and designers of concrete infrastructure, the investigated CFRP systems show potential for enhancing the shear strength of corroded concrete structures.

ACKNOWLEDGEMENTS

Special thanks to Dr Samir Dirar for his guidance and advice throughout this long journey. I truly appreciate everything he has done for me as a lecturer, supervisor and friend.

I also would like to thank Prof Andrew Chan and Dr Jian Yang for their invaluable support, guidance, discussion, comments and advice throughout the study.

In addition, I would like to thank Mr David Cope and my colleagues, especially Mr Haolin Su and Mr Wenxin Zuo, who spent significant amounts of time helping me prepare and test the specimens in the laboratory. Without their help, I could not have completed the experimental work.

Thanks should also go to those who helped and advised me on the use of TNO DIANA, especially Drs Ayad Aldeka, Michael Qapo, Ridwan and Mosleh Tohidi. Thank you for your suggestions and help.

Special thanks to the Engineering and Physical Sciences Research Council (EPSRC) for funding my research.

Last but not least, I would like to thank my family. Thank you for your understanding and support. Without you, I would not have had enough strength to complete this research.

CONTENTS

LIST OF FIGURES

LIST OF TABLES

CHAPTER 1: INTRODUCTION

1.1. Background

Annually, large amounts of money are spent on repairing corroded reinforced concrete (RC) structures. In the United Kingdom (UK) alone, it has been estimated that the cost of repairing corroded RC bridges is about £616.5 million (Broomfield, 2007). In the United States, the situation is even worse as the annual estimated direct cost of replacing or repairing corroded bridges is $8.3 billion (Koch et al., 2001). Other countries in North America and Europe are faced with the same challenge, thus emphasizing the global significance of the issue.

The use of de-icing salts in cold regions and/or windborne salts in coastal/marine environments are the main causes of chloride contamination of concrete (El-Maaddawy and Chekfeh, 2013). Chlorides break down the protective passive layer of iron oxides around the internal steel reinforcement and thereby facilitate the corrosion process. The volume of the corrosion products, which is larger than that of the steel consumed in the corrosion process, stresses the surrounding concrete and initiates cracking and spalling of the concrete cover (El Maaddawy and Soudki, 2007).

Internal steel shear links are susceptible to corrosion due to their proximity to the outer surfaces of concrete members. Corrosion of the internal steel shear links can have a detrimental impact on the shear strength of RC beams, and may lead to sudden and catastrophic brittle failure (Xia et al., 2011). There is thus scope for safe, practical, and durable shear strengthening methods.

In the last two decades, the use of fibre-reinforced polymer (FRP) reinforcement for retrofitting RC structures has become a field of much research interest. FRPs have several advantages over classic strengthening techniques, such as design flexibility, ease of use, and corrosion resistance. Methods for shear strengthening of RC beams using FRP composites include externally bonded (EB) sheets (Dirar et al., 2012) or plates (Mofidi et al., 2014), near-surface mounted (NSM) bars (Rahal and Rumaih., 2011), prestressed carbon fibre reinforced polymer (CFRP) straps (Dirar et al., 2013) and embedded CFRP rods (Valerio et al., 2009; Mofidi et al., 2012a). Compared with the EB and NSM shear strengthening methods, the deep embedment (DE) technique, also known as the embedded through section (ETS) technique (Valerio and Ibell., 2003; Valerio et al., 2009; Mofidi et al., 2012a), offers better bond performance between the concrete and the FRP reinforcement (Chaallal et al., 2011).

1.2. Aim and objectives

The aim of this study was to investigate the shear behaviour of uncorroded and corroded RC T-beams strengthened with different CFRP composites, the critical factors affecting the shear contribution of DE CFRP rods, and to review the accuracy of the Concrete Society Technical Report 55: Design guidance for strengthening concrete structures using fibre composite materials (also known as TR-55) which estimates the shear contribution of DE CFRP rods at ultimate limit state based on the truss analogy method. To achieve these aims, the following objectives were set:

1) To identify the effect of monotonic loading on shear force capacity and failure mode of un-strengthened, as well as CFRP-strengthened, RC T-beams with

corroded shear links,

2) To develop non-linear finite element (NLFE) predictive tools capable of modelling the behaviour of the experimental specimens,
3) To carry out a parametric study to identify the effect of concrete strength, steel-to-CFRP shear reinforcement ratio and shear span-to-effective depth ratio on the shear strength enhancement offered by DE CFRP rods, and
4) To enrich general understanding and expand the test database of RC members strengthened in shear with FRP systems, and compare the results of experimental tests, numerical models and the predictions of TR-55.

1.3. Research methodology

In order to meet the objectives outlined above, physical testing as well as NLFE modelling will be used. Physical testing involves testing nominally identical RC T-beams with various corrosion levels (un-corroded, 7% or 15%) and different CFRP strengthening methods (DE-strengthened or EB-strengthened) under a three-point-bending configuration. Numerical modelling involves validating the NLFE models against the experimental tests. The validated numerical models will then be used to study the critical parameters which influence the shear contribution of DE CFRP rods. Once these two approaches have been completed, the accuracy of TR-55 predictions can be addressed.

1.4. Research innovation

A careful review of the published literature reveals that research studies investigating the shear behaviour of RC beams strengthened using the DE technique is scarce. Moreover, very few studies have considered the behaviour of CFRP shear-strengthened RC T-beams with corroded shear links (El-Maaddawy and Chekfeh,

2013), where RC T-beams adequately simulate the slab-on-beam construction method. In reality, the majority of bridge superstructures behave as T-beams made up of beams and decks rather than rectangular beams. However, the results should be applicable to rectangular beams as well. Furthermore, to date there are no research studies comparing the effectiveness of the EB and DE CFRP shear strengthening systems in the context of RC T-beams with corroded shear reinforcement.

1.5. Thesis outline

Following the introduction of the research problem addressed in Chapter 1, Chapter 2 reviews the existing literature, Chapters 3 details the experimental work and Chapter 4 discusses the results of the experimental tests. Chapter 5 reviews NLFE modelling concepts and validates the proposed NLFE models against the experimental results. A parametric study of critical parameters (corrosion level, concrete compressive strength, steel-to-CFRP shear reinforcement ratio and shear span-to-effective depth ratio) on the shear contribution of DE CFRP rods and the comparison of experimental results to TR-55 and NLFE predictions is presented in Chapter 6. Chapter 7 summarises the key findings of the current research, the applicable limitations and recommendations for future research.

CHAPTER 2: LITERATURE REVIEW

2.1. Introduction

This chapter reviews the existing literature and presents the latest research developments in shear behaviour of corroded reinforced concrete (RC) T-beams strengthened with CFRP composites. The shear behaviour of RC beams is discussed in Section 2.2, including categories of shear failure, typical shear failure modes, and shear capacity prediction methods.

Corrosion effects on RC beams are explained in Section 2.3, with particular reference to corroded shear links. The different effects of natural corrosion and laboratory-based corrosion processes are compared, and the critical level of corrosion is identified based on Almusallam (2001).

Section 2.4 focuses on fibre reinforced polymer (FRP) composite strengthening techniques. The shear behaviour of RC T-beams repaired with CFRP composites is reviewed, including the difference between strengthening technologies with externally bonded (EB) CFRP sheets and deep embedded (DE) CFRP rods. The failure modes of the strengthened beams are also reviewed.

The methodology of using Fibre Bragg grating (FBG) sensors to record strain is discussed in Section 2.5. Finally, Section 2.6 addresses the knowledge gap and summarises the methodology adopted in this research.

2.2. Shear in reinforced concrete

There are two major failure modes of RC beams: flexural failure and shear failure.

Flexural failure is caused by the yielding of tension reinforcements and occurs in RC sections with adequate shear capacity. The flexural failure of an under-reinforced section occurs in a ductile manner. By contrast, shear failure is brittle and sudden in nature.

The shear behaviour of RC beams has been well studied since the 1960s. In 1962, the widely used truss analogy was reported on by the American Concrete Institute and American Society of Civil Engineers (ACI-ASCE) Committee 326 (1962) and is still used today. A similar report to further understanding was published in 1973 by the ACI-ASCE Joint Committee 426 (1973). It should be noted that shear behaviour is always accompanied by other behaviours, such as bending, torsion, and axial loads.

2.2.1. *Shear in a plain concrete beam*

Figure 2.2.1 shows a simply supported concrete beam under a uniformly distributed load (Pillai and Menon, 2003). The meaning of 'shear', in this case, is a shortening of the phrase 'flexural shear'. For a small concrete block at section X-X and 'y' distance from the neutral axis in Figure 2.2.1 (a), Figure 2.2.1 (b) shows that the uniformly distributed load causes the bending moment, M, and shear force, V, at the section of concrete block. The bending moment, M, causes a tension or compression force on the block, depending on the location of the block. Figure 2.2.1 (c) shows that this tension or compression force due to the bending moment, M, and the shear force, V, can be simplified to axial stresses (bending stresses), f_x, and shear stresses, τ, on the block respectively. The combination of bending stress and shear stress causes principal stresses, f_1 and f_2.

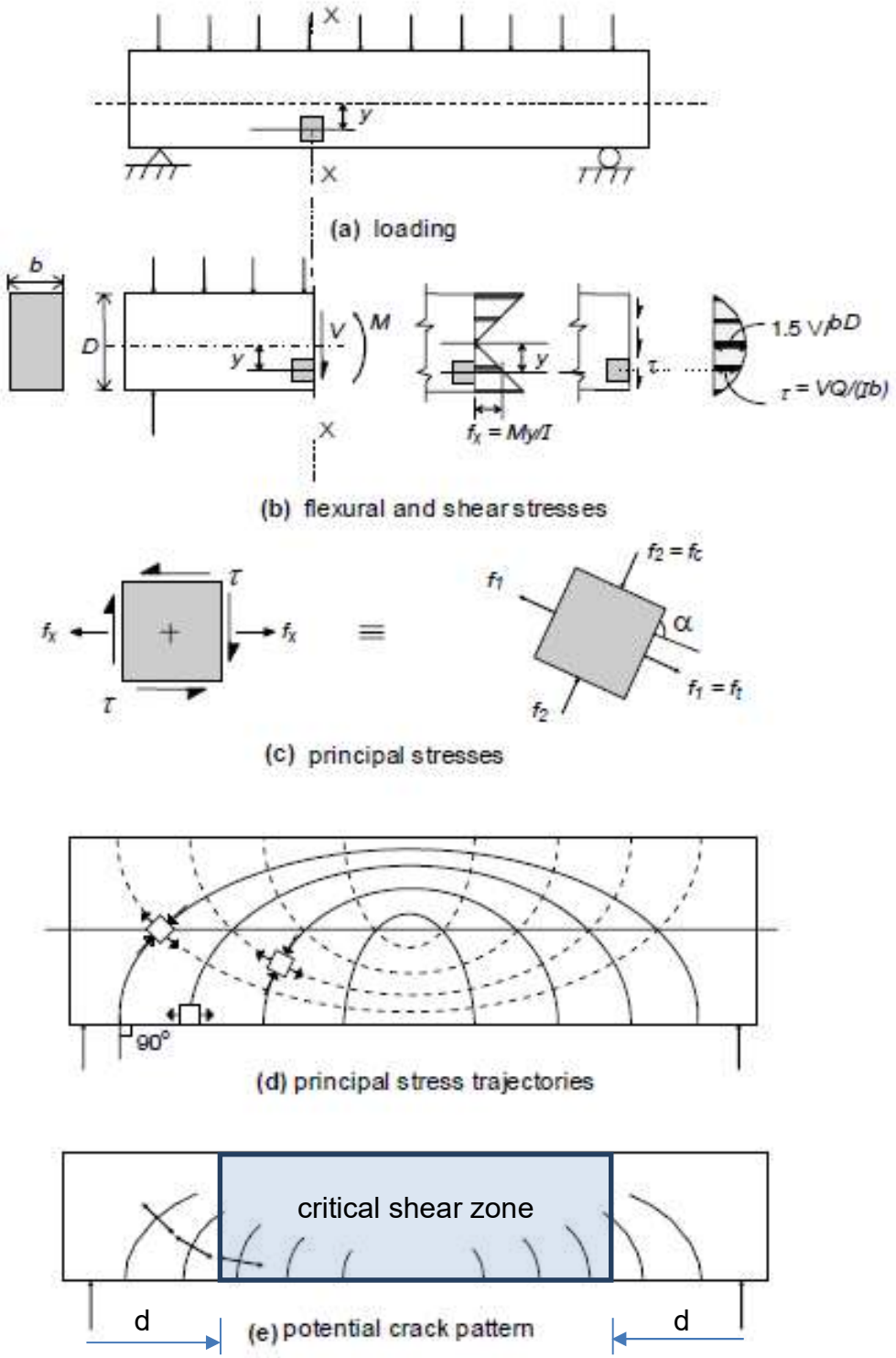

Figure 2.2.1: Stress distribution in homogeneous beams with rectangular section (a) loading, (b) flexural and shear stresses, (c) principal stresses, (d) principal stress trajectories, and (e) potential crack pattern
- from Pillai and Menon (2003)

The principal stresses can normally be considered as a pair of compression, f_2 *(or* f_c*)*, and tension, f_1 *(or* f_t*),* stresses. The relationships between principal stresses, bending stresses, and shear stresses are summarised in Equations 2.1 to 2.3.

$$f_1 = \frac{f_x}{2} + \sqrt{{f_x}^2 + 4\tau^2} \quad (2.1)$$

$$f_2 = \frac{f_x}{2} - \sqrt{{f_x}^2 + 4\tau^2} \quad (2.2)$$

$$tan2\alpha = \frac{2\tau}{f_x} \quad (2.3)$$

where:

f_1 Principal tension stress (maximum principal stress, *N/mm²*).

f_2 Principal compression stress (minimum principal stress, *N/mm²*).

f_x Bending stress. $f_x = \frac{My}{I}$ (*N/mm²*).

τ Shear stress $\tau = \frac{VQ}{Ib}$ (*N/mm²*).

α The inclination of the principal tensile stress with respect to beam axis (*degrees*).

M Bending moment at the section (*Nmm*).

y Distance from centroid of the block to the neutral axis of the beam (*mm*).

I Second moment of area (*mm⁴*).

V Shear force at the section (*N*).

Q First moment of area (*mm³*).

b Width of the beam at the layer where shear stress is calculated (*mm*).

Any pair of the principal stresses should be in equilibrium in the beam under loading. If either the pair of principle compression stresses or principle tension stresses exceeds the compressive or tensile strength of the concrete, the concrete block will

fail in compression or tension respectively. Accompanied by this failure, a diagonal tension crack normally develops (see Figure 2.2.1 (e)). The compressive and tensile strengths can be determined from a material test. The crack normally develops in the principle compression stress direction, as shown in Figure 2.2.1 (e). Once the crack develops, the stress distributions depicted here are no longer valid in that region, as the effective section is altered and the above equations are no longer valid.

2.2.2. *Shear in beams without shear links*

Pillai and Menon (2003) concluded that shear capacity results from three main mechanisms for a beam without shear links. They are the shear capacity in the compression concrete, V_{cz}, the interface shear capacity, V_a (normally called 'aggregate interlock'), the dowel force, V_d, in the tension reinforcement. However, the entire aggregate interlock does not resist the shear force; only the vertical component, V_{ay}, is helping to resist the shear force as shown in the free-body diagram in Figure 2.2.2. By contrast, the shear contribution due to the dowel action is an additional shear contribution to the homogeneous concrete section.

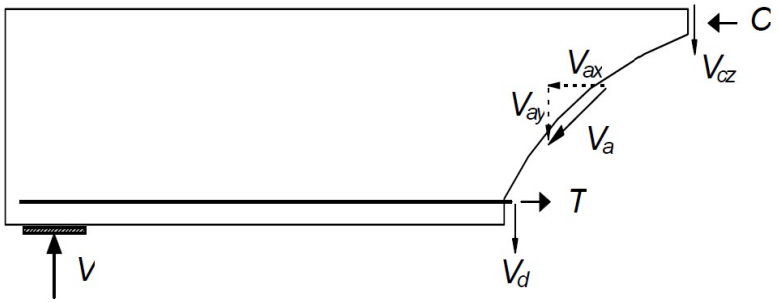

Figure 2.2.2: Shear failure mode in concrete beams without shear links
- Pillai and Menon, 2003

The contribution of these mechanisms depends on the loading stage, the extent of cracking, and the material and geometric properties of the beam. Prior to flexural cracking, the external applied shear is mainly resisted by the un-cracked concrete, V_{cz}. When the loading is increased, some interface shear, V_a, and dowel action, V_d, will develop to assist the redistribution of stresses. As the diagonal tension cracks appear, the concrete can only resist a limited amount of tensile stress; hence, the beam can undergo a sudden increase in tensile strain and stress, and cause the sudden failure of the RC beam. All three mechanisms will be involved at this stage. It is important to note that the presence of the longitudinal reinforcement in the tension zone not only contributes to enhanced dowel action, but also serves to control the development of flexural cracks, and contributes to an increase in the depth of the neutral axis. In this way, the depth of the un-cracked concrete in compression is increased, which enhances the contributions of aggregate interlock and shear resistance in the compressed concrete.

2.2.3. *Shear in beams with shear links*

In beams with shear links (especially when effective depth is greater than the spacing of the shear links), the shear links intercept the diagonal tension cracks and prevent the sudden increase in tensile strain and stress. Therefore, shear resistance continues to increase even after the formation of incline cracks, until shear reinforcement yields in tension. As the cracks normally develop from the support to the loading point, inclined shear links (perpendicular to the crack opening direction) are more efficient than vertical shear links. However, if excessive shear reinforcement is provided, it is likely that the ‘shear-compression’ mode of failure (see

Section 2.2.4) will occur first. This is undesirable as such a failure will occur suddenly and without warning.

The numerical formulae used to represent the mechanism behaviour are summarised in Equations 2.4 and 2.5. The difference between tension force, *T*, in steel and compression force, *C*, in concrete is equal to the horizontal component of aggregate interlock force, V_{ax}.

$$V = V_{cz} + V_{ay} + V_d + V_s \quad (2.4)$$

$$T = V_{ax} + C \quad (2.5)$$

where:

V Total shear resistance (*N*).

V_{cz} The shear resistance from compression zone (*N*).

V_d Shear resistance from dowel action (*N*).

V_{ay} Component force of aggregate interlock perpendicular to the beam (*N*).

V_{ax} Component force of aggregate interlock in parallel to the beam (*N*).

V_s Shear resistance from shear link (*N*).

T Tensile force in steel (*N*).

C Compressive force in concrete (*N*).

2.2.4. *Shear failure modes*

As discussed above, loading has to be transferred from the loading position to a support along load path(s). This action can typically be classified as beam action or arch action. Evans and Kong (1987) detailed these actions based on the shear span length-to-effective depth ratio, a_v/d, (also known as shear span-to-effective depth ratio); see Table 2.2.1. The shear span length is the horizontal distance between the

applied loading-point and the support (for a point load); the effective depth is the depth from the compression concrete face to the centre-line of the main tension reinforcements.

Table 2.2.1: Beam Shear Classification, Evans and Kong (1987)

Shear Span-to-Effective Depth Ratio, a_v/d	**Beam Type**	**Classification**
$a_v/d \leq 1$	Deep	Very Short
$1 < a_v/d \leq 2.5$	Deep	Short
$2.5 < a_v/d \leq 6.5$	Slender	Slender
$a_v/d > 6.5$	Slender	Very Slender

The shear span-to-effective depth ratio, a_v/d, represents the relationship between the applied moment and the shear force; see Equation 2.6 for details.

$$\frac{a_v}{d} = \frac{Va_v}{Vd} = \frac{M}{V} \times \frac{1}{d} \qquad (2.6)$$

where:

a_v Shear span length (*mm*).

d Effective depth (*mm*).

V Applied shear force (*N*).

M Applied moment (*Nmm*).

'Beam action' (a_v/d > 2.5) is where the concrete beam starts to crack, with flexure cracks developing perpendicular to the concrete tension face. These cracks are typically located away from the support or a change in cross section. When the a_v/d is greater than 6, the beam usually fails in bending. When a_v/d is between 2.5 and 6.5, the flexure crack gradually becomes an inclined crack as the applied load

increases. This is known as a flexure-shear crack. With a relatively high a_v/d, the diagonal crack will rapidly develop into a concrete compression zone towards the loading point, and the beam could fail suddenly. Such a failure mode is often called 'diagonal-tension failure'. For a low a_v/d in the range of 2.5 to 6.5, the secondary crack normally develops along the longitudinal tension reinforcement. As the applied loading increases, the secondary crack becomes increasingly wide, and eventually the beam fails. Such a failure mode is often called shear-tension failure (Pillai and Menon, 2003).

For a_v/d less than 2.5, the beam normally fails due to arch action. When the ratio is between 1 and 2.5, a failure crack usually develops near the support. This failure crack usually forms independently and not as a development of a flexural crack. With an increase in the applied load, the diagonal crack penetrates into the concrete compression zone until eventually a crushing failure of the concrete occurs. This failure mode is called shear-compression failure. For ratios less than 1, the crack normally forms as a line joining the support and the loading points. This failure crack is mainly due to compression failure between the load and the support (Park and Paulay, 1975).

2.2.5. *Reinforced concrete shear prediction models*

Numerous models are available to predict the shear capacity of RC beams, such as the empirical model developed by Sarsam and Phillips (1985) where total shear strength is based on the sum of two basic contributions relating to concrete and steel shear links. The other well-known models are truss analogy, compression field theory, modified compression field theory, and strut-and-tie model.

- Truss analogy

A number of code-adopted methods are based on the truss analogy model. The truss analogy assumes that the concrete sustains compression and the reinforcements sustain tension. The truss model is based on the lower-bound theorem of plasticity; for details refer to Kong (2002). MacGregor and Bartlett (2000) suggested that the truss model ignores the effects of shear in the compression zone, the vertical component of aggregate interlock, and the dowel action of the reinforcement. Furthermore, the application of a truss system is not unique; hence, more members in a system will be more efficient as each members contributes to its ultimate load capacity.

- Compression field theory

Compression field theory was introduced in 1974. This method is based on compatibility, equilibrium, and constitutive relationships. This method considers concrete stresses in principal directions superimposed with the stresses in the reinforcement, which is assumed to be only axial. The concrete constitutive relationship takes into account the softening effect, but it assumes that the concrete cannot take any tension (where tension strength = 0 N/mm^2). Thus, Vecchio and Collins (1986) developed the modified compression field theory (MCFT) to take account of the tensile capacity of concrete that results from the tension stiffening effect.

- Strut-and-tie model

The strut-and-tie model is another model accepted by many codes of practice, such as the American Association of State Highway and Transportation Officials

(ASSHTO) (2012) and Eurocode 2 (2004). This model is generally represented by considering RC sections with concrete struts and reinforcement ties. The concrete struts are typically limited by the angle of the load transfer and the width of the supporting bearing, and most importantly, the concrete struts must fit within the geometric constraints of the beam.

- Other shear capacity prediction models

A number of studies have proposed shear capacity prediction models based on the considerations discussed above. Bažant and Kim (1984) proposed an expression to consider both beam and arch action. In Bažant and Kim's (1984) proposal, both beam and arch action depend on the reinforcement ratio. Furthermore, beam action is affected by the concrete strength, while arch action is affected by the span-to-depth ratio.

In 1997, Russo and Puleri (1997) further developed Bažant and Kim's (1984) proposed expression by introducing an effectiveness factor. This effectiveness factor was developed based on the hypothesis that shear links are less effective when arch action is dominant and more effective when beam action is dominant.

MacGregor and Bartlett (2000) proposed a formula that also considered both beam action and arch action. Beam action was contributed by the horizontal shear flow, and arch action will only occur when the shear flow is interrupted by an inclined crack.

Matamoros and Wong (2003) and Russo et al. (2005) developed several formulae based on the strut and tie approach. Matamoros and Wong (2003) considered that shear resistance is contributed by a direct strut, a vertical tie, and a horizontal tie.

Each component is limited by its material strength and combined with a coefficient. The coefficients were determined by experimental work. Russo et al (2005) took account of the softening effect experienced by concrete in tension and the effects of web reinforcement.

2.2.6. *Size effects*

Most experimental tests have been carried out on relatively small beams or parts of a beam. It is difficult to simulate an entire bridge structure in laboratory tests. Hence, understanding size effects is extremely important in the study of the shear behaviour of RC beams. Kani (1967) suggested that the shear strength of concrete beams without web reinforcement appears to decrease as the effective depth increases. Taylor (1972) found that the effect of the absolute size of a beam on its shear strength is not as large if proper scaling of all properties is taken into account. Dowel and aggregate interlock actions, in particular, can be considerably reduced in large beams if aggregate and reinforcement sizes are not correctly scaled. Bhal (1968) concluded that the relative reduction of shear strength of large beams was less significant when beams with web reinforcement were compared.

To summarise the above findings, size effects on the shear strength of RC beams are represented by a reduction in ultimate shear strength as an increase of beam size, especially for shallow RC beams (Zhang and Tan (2007)). Bažant and Kazemi (1991) studied size effects on diagonal shear failure of beams without shear links. It has been suggested that the causes of size effects may be explained in terms of fracture mechanics concepts in non-linear forms, and that the effect can be predicted by the Bažant (1984) model.

2.3. Corrosion

Corrosion is an electrochemical process. There are several causes of corrosion in RC structures, such as carbonation and chloride ingress. Carbonation is due to the ingress of carbon dioxide that reduces the alkalinity of the concrete. By contrast, chloride ingress occurs when chloride ions penetrate into the concrete and cause corrosion of the reinforcement. Carbonation is a relatively slow process that causes a generalised or uniform corrosion. Chloride ingress affects the structure across its entire service life. In particular, coastal structures and those structures having exposure to chloride-based de-icing chemicals are affected. As a result, chloride ingress needs to be studied in greater detail.

2.3.1. *Chloride-induced corrosion and carbonation-induced damage*

During the service life of an RC structure, the cracks of a structure under action may develop from the surface of the concrete to the reinforcement level. Chloride ions penetrate the concrete and break down the alkaline protective layer around the reinforcement. Eventually, corrosion occurs in the presence of moisture (H_2O) and oxygen (O_2). Once the chloride ions (Cl^-) penetrate into the steel reinforcement, the reinforcement (mainly irons, Fe) starts to corrode and rust (iron hydroxide, $Fe(OH)_2$ and $Fe(OH)_3$). $Fe(OH)_3$ can be transformed into hydrated ferric oxide, ($Fe_2O_3 \cdot H_2O$), where the unhydrated ferric oxide, Fe_2O_3, is formed on the surface of the reinforcement. Usually, Fe_2O_3 has a volume about twice that of the steel. It replaces the steel when fully dense. Such an increase in volume leads the stress to increase at the interface between the concrete and steel, until eventually, the interface concrete is propagated due to its lower tensile strength. The electrochemical

reactions can be summarised as follows:

$$Fe \rightarrow Fe^{2+} + 2e^{-} \quad (2.7)$$

$$2e^{-} + H_2O + {}^{1}/_{2}\, O_2 \rightarrow 2OH^{-} \quad (2.8)$$

It should be noted that Equation 2.7 presents the reaction at the anode, and Equation 2.8 presents the reaction at the cathode. The electrochemical reactions are shown by Equations 2.9 to 2.11:

$$Fe^{2+} + 2OH^{-} \rightarrow Fe(OH)_2 \quad (2.9)$$

$$4Fe(OH)_2 + O_2 + 2H_2O \rightarrow 4Fe(OH)_3 \quad (2.10)$$

$$2Fe(OH)_3 \rightarrow Fe_2O_3 \cdot H_2O + 2H_2O \quad (2.11)$$

These electrochemical reactions do not just reduce the physical properties of the shear links (e.g. reducing the diameter), but also weaken the bond of the interfacial transition zones (ITZs) of the longitudinal steel-to-concrete and shear links-to-concrete interfaces; see Yuan et al (2007).

Recently a lot of researchers have drawn attention to carbonation of concrete as a result of climate change, such as Yoon et al (2007). Carbonation of concrete is a chemical reaction of portlandite, $Ca(OH)_2$. Carbon dioxide, CO_2, reacts with hydrated cement paste, mainly as $Ca(OH)_2$ in pore water, to reduce the natural alkalinity of concrete. The main chemical reactions are shown in Equations 2.12 and 2.13:

$$Ca(OH)_2 \rightarrow Ca^{2+}(aq) + 2OH^{-}(aq) \quad (2.12)$$

$$Ca^{2+}(aq) + 2OH^{-}(aq) + CO_2 \rightarrow CaCO_3 + H_2 \quad (2.13)$$

2.3.2. *Methods of simulating corrosion processes in the laboratory*

There are three techniques that can be used to corrode reinforcements in the

laboratory: natural corrosion, accelerated corrosion, and simulated natural corrosion. The natural corrosion process is time-consuming to reproduce under lab conditions. Yuan et al. (2007) compared the Galvanostatic corrosion process and the simulated natural corrosion process, and the results were comparable. Therefore, these two techniques were compared.

- *Galvanostatic method*

The Galvanostatic method was developed based on the electrochemical process. Higgins and Farrow (2006), Xia et al. (2011), and several other researchers carried out corrosion damage research on RC beams based on this method. The concrete is either mixed with/without chemicals containing chloride (normally 2% calcium chloride by mass of cement), and then cured for 28 days. After curing, the concrete is placed in a salted water tank (3% salt by mass of water). By introducing 2% calcium chloride by mass of cement, it will increase the electrical conductivity and add more free chloride ions. With more free chloride ions, the possibility of corrosion will be more likely to occur. Du et al (2005) added 4% calcium chloride to the weight of cement to study the residual capacity of corroded steel reinforcements. Rodriguez et al (1997) also used 3% calcium chloride in their study of load carrying capacity of concrete structures. The calcium chloride increases the electrical conductivity of the RC beam; however, as additional calcium is added into the mix, the concrete strength is normally higher than expected. The salt water does not just speed up the corrosion process, but also simulates a marine environment (such as an RC structure below sea level). Xia et al. (2011) also used the Galvanostatic method with wetting and drying cycles to simulate in-sea and out-of-sea environments when the tide

changes.

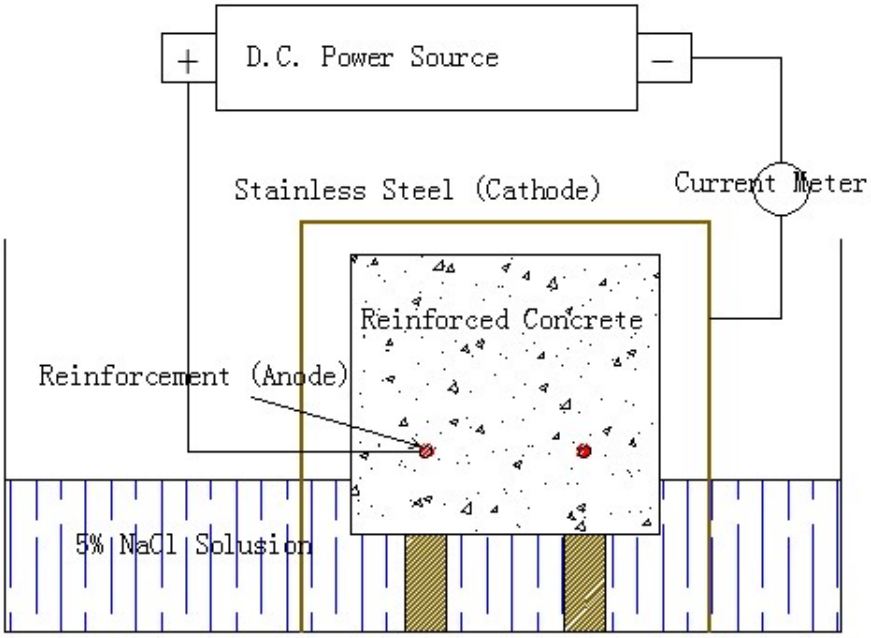

Figure 2.3.1: Corrosion arrangement of Galvanostatic method
- Azad et al, 2007

A direct current from the positive terminal of a power supply is applied to the reinforcement in the concrete with the concrete placed in the tank. The negative terminal connects through a current meter to a stainless steel sheet. In the resulting circuit, the reinforcement acts as an anode and the stainless steel sheet acts as a cathode. Figure 2.3.1 shows the corrosion arrangement of the Galvanostatic method. By applying a constant current, the chloride irons will quickly penetrate to the steel reinforcement surface, and eventually the electrochemical process will occur.

- *Climate control method*

The artificial climate control method involves subjecting the specimen to a high temperature, high humidity, and repeated wetting-and-drying cycles. However, this

method does not permit prediction of the corrosion level and takes a longer time to reach the targeted corrosion levels (7% and 15%). The advantage of using this method is that it is slightly faster compared with the natural corrosion process, and it truly behaves like the steel reinforcement corrosion process in nature. As it is still slow and difficult to carry out this process, this method was not considered.

- *Comparison of two corrosion methods*

Yuan et al. (2007) found that the Galvanostatic method is slightly different from the artificial climate control and natural corrosion methods. Using the Galvanostatic method, rust forms on the entire surface of the steel reinforcement. In reality, rust forms from the near face of the concrete to the far side of the steel reinforcement. However, both methods reduce the loading capacity and ductile characteristics of the steel reinforcements and transform the failure mode from ductile to brittle. In conclusion, the final results between the Galvanostatic method and the artificial climate control method are comparable. Hence, the Galvanostatic method can be used in the laboratory to simulate the corrosion behaviour of the steel reinforcement in a shorter time and achieve comparable results. Another advantage of using the Galvanostatic method is that the level of corrosion can be predicted by Faraday's law; see Equation 2.14.

$$M_{th} = \frac{W.I_{app}.T}{F} \qquad (2.14)$$

where:

M_{th} Theoretical mass of rust per unit surface area of the reinforcement (*g/mm*^{2}).

W Equivalent weight of steel that is taken as the ratio of atomic weight (55.85 *g*) of iron to the valency of iron (2) = (27.925 *g*).

I_{app} Applied current density (*A/mm²*).

T Duration of induced corrosion (*s*).

F Faraday's constant (96,487 *A-s*).

This equation can be developed to Equation 2.15 for a uniform steel section. A similar relationship was also determined by Du et al. (2005). The proposed formulae are presented in Equations 2.16 and 2.17:

$$Q_{corr} = \frac{M_{th} \times dl}{M} = \frac{W.I_{app}.T}{F} \cdot \frac{dl}{\frac{1}{4}\pi d^2 l \rho_s} = 0.0472 \frac{I_{app} T}{d} \quad (2.15)$$

$$Q_{corr} = 1 - \left(\frac{d_s}{d}\right)^2 \quad (2.16)$$

$$Q_{corr} = 4 \frac{x_{corr}}{d} = 0.046 \frac{I_{app} T}{d} \quad (2.17)$$

where:

Q_{corr} Percentage of corrosion level.

M_{th} Theoretical mass of rust per unit surface area of the reinforcement (*g/mm²*).

M Initial weight of the bar before corrosion (*g*).

d Diameter of the corroded reinforcement (*mm*).

l Total length of the corroded reinforcement (*mm*).

I_{app} Applied current density (*A/mm²*).

W Equivalent weight of steel that is taken as the ratio of atomic weight (55.85 g) of iron to the valency of iron (2) = (27.925 *g*).

T Duration of induced corrosion (*s*).

F Faraday's constant (96,487 *A-s*).

ρ_s Steel density (7,800E-6 *g/mm³*).

x_{corr} The corrosion attack penetration at the reinforcement surface: $x_{corr} = 0.0115 I_{app} T$.

d_s Diameter of corroded reinforcement (*mm*).

2.3.3. *Effect of corrosion on the properties of steel reinforcement*

The factors that influence the behaviour of corroded RC structures include reinforcement corrosion level and crack width. The effect of corrosion on mechanical characteristics of steel reinforcement has been well studied and was summarised in Table 2.3.1, where f_y is the nominal yield stress of a corroded reinforcement, f_u is the nominal ultimate strength of the corroded reinforcement, f_{y0} is the nominal yield stress of the corroded reinforcement when it is uncorroded, f_{u0} is the nominal ultimate yield stress of the non-corroded reinforcement, E is the modulus of elasticity of the steel reinforcement, Q_{corr} is the corrosion level of the corroded reinforcements, λ is the elongation percentage of the corroded reinforcement, and λ_0 is the elongation percentage of the non-corroded reinforcement.

Table 2.3.1: Models for the mechanical properties of corroded reinforcement - Du et al, 2005

Model	Equations
Andrade et al. (1991)	$f_y = 570 - 8.2Q_{corr}$ $f_u = 636 - 8.57Q_{corr}$ $\lambda = 10.63 - 0.176Q_{corr}$
Lee et al. (1996)	$f_y = 352.2 - 4.3Q_{corr}$ $E_s = 192583 - 2423Q_{corr}$

Saifullah (1994)	For Plain Reinforcement: $f_y = 337 - 4.32Q_{corr}$ $f_u = 524 - 8.78Q_{corr}$ For Ribbed Reinforcement: $f_y = 507 - 5.87Q_{corr}$ $f_u = 676 - 9.75Q_{corr}$
Morinaga (1996)	$f_y = 360 - 5.77Q_{corr}$ $f_u = 501 - 13.17Q_{corr}$ $\lambda = 23.5 - 1.415Q_{corr}$
Zhang et al. (1995)	$f_y = (1.00 - 0.01053Q_{corr})f_{y0}$ $f_u = (1.00 - 0.01072Q_{corr})f_{u0}$ $\lambda = (1.00 - 0.016Q_{corr})\lambda_0$

All models can be converted into a similar form, as shown in Equations 2.18 to 2.21:

$$f_y = (1.00 - AQ_{corr})f_{y0} \quad (2.18)$$

$$f_u = (1.00 - BQ_{corr})f_{u0} \quad (2.19)$$

$$E_s = (1.00 - CQ_{corr})E_{s0} \quad (2.20)$$

$$\lambda = (1.00 - DQ_{corr})\lambda_0 \quad (2.21)$$

where:

A Constant varies from 0.01 to 0.016.

B Constant varies from 0.01 to 0.026.

C Constant equals 0.013.

D Constant varies from 0.016 to 0.06.

E_{s0} Elastic modulus of non-corroded reinforcement.

These formulae show that yield strength, ultimate strength, elasticity and elongation

of reinforcement decrease more than the reduction in the cross section area of steel reinforcement.

Du et al. (2005) concluded that three parameters influence concrete cracking due to the corrosion process: corrosion time, corrosion level, and corrosion penetration. When using the Galvanostatic method to accelerate the corrosion speed in the laboratory, Faraday's law can be used to calculate the corrosion level over a specific time. Andrade et al. (1991) proposed Equations 2.22 and 2.23 to determine the attack penetration:

$$x_{cr} = 0.318 \times 10^{-6} I_{cr} t_{cr} \quad (2.22)$$

$$x_{cr} = \frac{1}{4} D_0 Q_{cr} \quad (2.23)$$

where:

x_{cr} Attack penetration for concrete cracking (*mm*).

I_{cr} Current intensity (*A/mm²*).

t_{cr} Corrosion time (*s*).

D_0 Diameter of original reinforcement diameter (*mm*).

Q_{cr} Amount of corrosion of reinforcement (*%*).

Another parameter that influences the attack penetration and corrosion level is the ratio of concrete cover to reinforcement diameter. Al-Sulaimani et al. (1990) concluded that the relationship between attack penetration and ratio of concrete cover, *c*, to reinforcement diameter, *d*, and the relationship between corrosion levels were as follows:

$$x_{cr} = 0.0145 \left(\frac{c}{d}\right) + 0.0021 \qquad r = 0.864 \quad (2.24)$$

$$Q_{cr} = 0.4953\left(\frac{c}{d}\right) + 0.0856 \qquad r = 0.853 \qquad (2.25)$$

where:

x_{cr} Attack penetration for concrete cracking (*mm*).

Q_{cr} Amount of corrosion of reinforcement (*%*).

$\frac{c}{d}$ The ratio of concrete cover to reinforcement diameter.

D_0 Diameter of original reinforcement diameter (*mm*).

Q_{cr} Amount of corrosion of reinforcement (*%*).

r Regression

2.3.4. *Effects of corrosion on RC structures*

Rodriguez et al. (1996) summarised the effects of corrosion on the components of RC in three steps:

- The steel, due to the reduction of both the reinforcement cross section area and the mechanical properties.
- The concrete, due to the cover cracking produced by the expansion of corrosion products.
- The composite action of both concrete and steel, due to bond deterioration.

When steel starts to reduce its cross section area, it will then form an ITZ between the steel and concrete; this was investigated by Yuan et al. (2007). In 2009, Yuan et al (2009) found that the corrosion process will start from the side of the reinforcement facing the concrete cover only, and the corrosion rate will experience three phases, namely ‘descending phase’ at the initial corrosion, then ‘steady phase’, and finally ‘ascending phase’ after concrete cover cracking caused by corrosion.

The bond deterioration occurs in a similar fashion to the reduction of steel cross

section area. The ITZ forms a new bond property that transfers loading between the reinforcement and the concrete. The ITZ will partially and uniformly distribute along the reinforcement. As the ITZ develops, slip will eventually occur between the concrete and the reinforcement due to the weakness of the newly formed rust.

In most RC beams, shear links are much closer to the concrete surface than the other reinforcements. Therefore, shear links would be the first to be attacked by chlorides in the corrosion process. Moreover, shear links are generally made of small diameter steel reinforcements and therefore, if they are corroded, the shear links will quickly lose their load-bearing ability. Almusallam (2001) concluded that for reinforcements corroded above 12.6%, brittle behaviour will be exhibited. Figure 2.3.2 presents the experimental results of Almusallam (2001) for load-elongation curves.

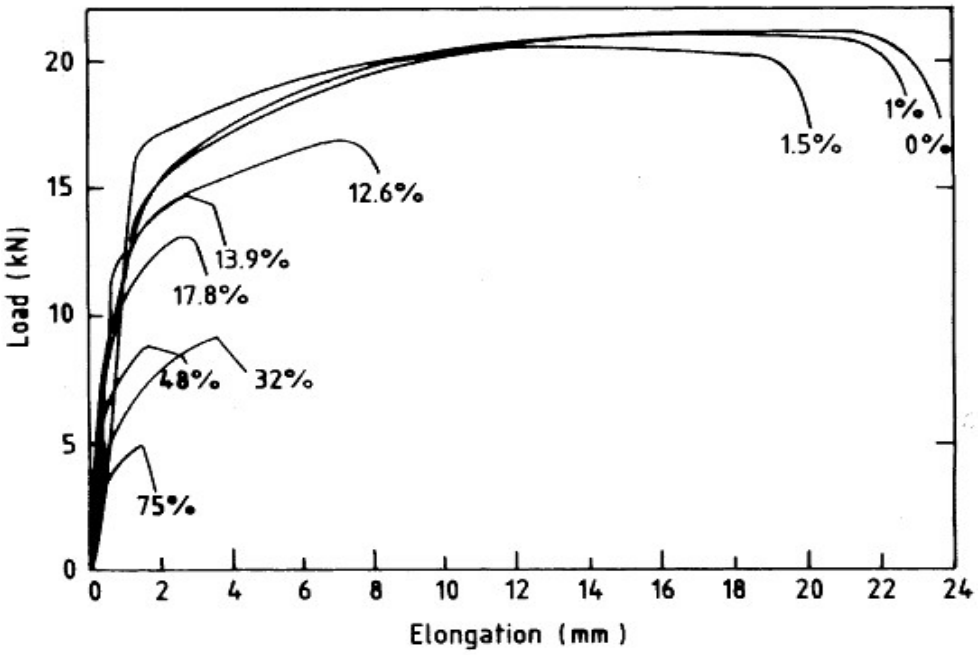

Figure 2.3.2: Load-elongation curves for 6 *mm* diameter steel reinforcements with different corrosion levels

- Almusallam, 2001

According to Figure 2.3.2, corrosion levels of 7% and 15% show that the steel reinforcement does not lose its ductility and completely loses it ductility respectively. For corrosion levels up to 7%, the reinforcement still retains its ductile property; however, the elongation in the hardening process is much shorter compared with un-corroded reinforcement. For corrosion levels up to 15%, the reinforcement behaves as a brittle material. It suddenly fails once it reaches the yield strength. However, other corrosion levels may be considered once these levels have been investigated.

Corrosion of reinforcements can lead to brittle failure of the structure in practice, as discussed above. The corrosion of metals is an electrochemical process. Almusallam (2001) and Du et al. (2005) confirmed that corrosion does affect the failure mode and ductile behaviour of reinforced concrete beams. An increase in corrosion levels decreases beam ductility and changes the ductile failure of under-reinforced beams to brittle failure.

2.3.5. *Shear behaviour of corroded RC beams*

Many studies have investigated the influence of corrosion on the behaviour of shear failure. The majority of research has focused on the influence of corroded tensile reinforcements or the influence of a combination of corroded tensile reinforcements and shear links. The longitudinal steel reinforcements and shear links are normally corroded at the same time. However, this study focused on the shear behaviour of RC beams. Hence, the effect of the corrosion on the shear link has been investigated.

Takahashi (2013) studied five rectangular RC beams with similar concrete

compressive strengths and span-to-depth ratios, but with different shear link spacings, corrosion levels, and shear link to cross-section ratio. The results showed that shear resistance was reduced as the corrosion level increased, due to the diameter and strength of the shear links being reduced. However, the moderated corrosion level may also change the failure mode from a diagonal tension failure to shear compression failure in some cases.

Similar results were reported by Xia et al. (2011). Xia et al. (2011) prepared eighteen rectangular RC beams to investigate shear behaviour based on the parameters of corrosion level, diameter of the shear link, and spacing of the shear link with other parameters held constant. It was concluded that the shear resistance of the beam decreases with the increase in the corrosion level of the shear link.

Xia et al. (2011) also suggested that the corrosion-induced crack could be used as an indicator of the corrosion level of the corroded shear links. The more severe the corrosion level of the shear links, the wider the crack width. However, more experimental data are required to develop an accurate relationship with different concrete covers and diameters of reinforcement.

The gradient of load-deflection curve decreases as the corrosion level increases. However, the reduction of gradient is insignificant when the applied load is relatively low. It is only when the applied load exceeds 20-30% of the ultimate load that the stiffness loss is significant due to the corrosion of shear link.

2.4. Fibre-reinforced polymer strengthening

Fibre-reinforced polymer (FRP) is a composite material which consists of high-

strength fibres and a matrix for binding these fibres to fabricated structural shapes. There are many types of FRP composite, such as aramid, carbon, glass, and high-strength steel. Since 1984, carbon fibre-reinforced polymer (CFRP) has been used in RC beam strengthening. The main advantages of using CFRP composites are their low weight (only 20% of that of steel), corrosion resistance, and ease of application.

A number of technical reports have been written on the use of FRP composite materials and design procedures. The UK Concrete Society published its first edition of design guidance for strengthening concrete structures using fibre composite materials (Technical Report 55 also known as TR-55) in 2000. They revised TR-55 to the third edition in 2012. This research is not limited to the UK. In the US, design guidance has been given by the American Concrete Institute (ACI Committee 440 (2015)). In Japan, the Japan Concrete Institute (JCI) also updates their documents frequently and Fédération internationale du béton / International Federation for Structural Concrete (FIB) technical report bulletin 14 (2001) is commonly used in European countries.

There have been many successful applications of FRP composites in the field over the last 20 years. The majority of the initial uses were in Japan, followed by Europe and North America. Currently, FRP composites are used to strengthen different types of structures in numerous countries.

2.4.1. *Mechanical properties of FRP composites*

It is commonly known that FRP is a brittle material. Unidirectional CFRP sheets normally have tensile strengths 5 to 8 times that of the steel reinforcement strength in

the strengthening direction. CFRP rods have similar properties. It should be noted that CFRP rods have two types of surfacing: sand-coated surfacing and plain surfacing. The sand-coated surfacing may offer better bond-slip stiffness between epoxy and CFRP rods, and consequently may improve the shear contribution of CFRP rods.

Figure 2.4.1 compares the stress-strain curves of different types of FRPs to the typical steel. It shows that all of these FRPs have the same stress-strain behaviour: linear elastic up to final brittle rupture when subject to tension. It also shows that only CFRP has comparable stiffness to steel. Apart from the typical stiffness and strength, these curves show a clear contrast between the brittle behaviour of FRP composites and the ductile behaviour of steel.

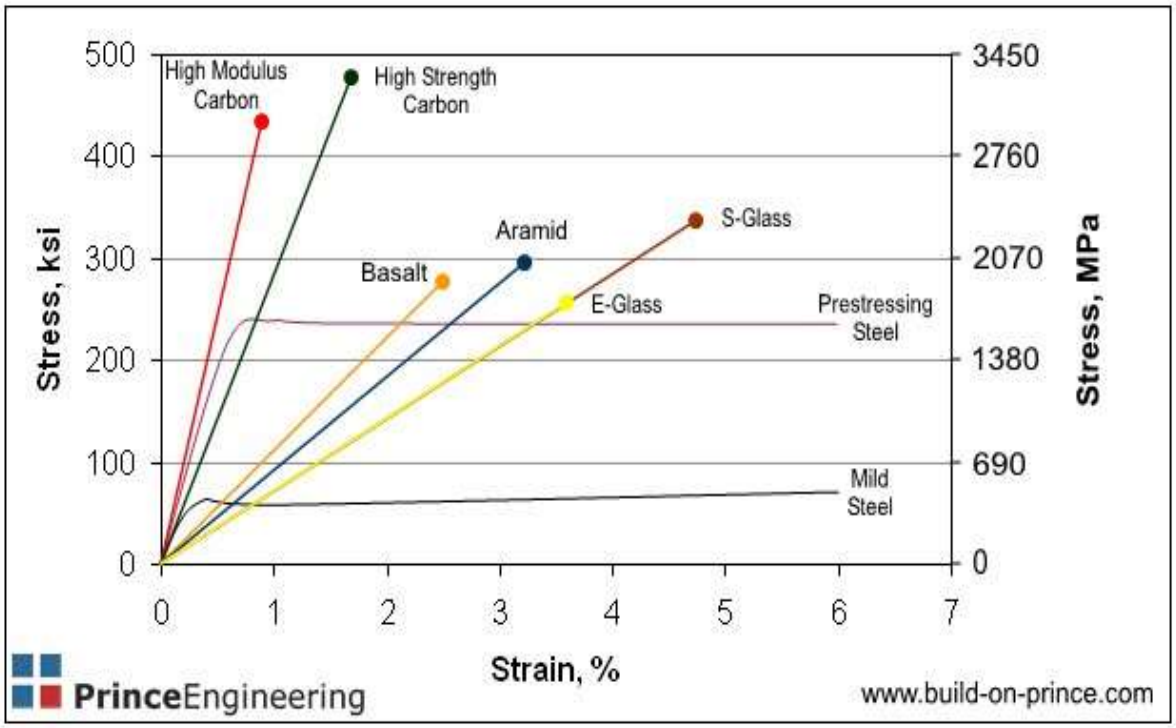

Figure 2.4.1: Comparison of FRP material to steel
- Prince Engineering, PLC

2.4.2. Strengthening RC beams with FRP composites

FRP composites typically use epoxy resins to bind different type of fibres together. As discussed previously, numerous researchers have studied the FRP strengthening behaviours of EB CFRP sheets. To install FRP sheets, two typical methods are commonly used. They are known as wet lay-up and prefabrication. Wet lay-up is more versatile for site application in terms of bonding to curved surfaces and wrapping around corners, whereas prefabrication allows for better quality control. It should be noted that access to the soffits of bridges is limited in some circumstances; hence, wrapping the structure is not possible.

For installing DE FRP rods, the FRP rods can be fixed with a reinforcing cage before casting the concrete. Alternatively, Valerio et al. (2009) demonstrated that it was possible to install FRP rods by drilling vertical holes upwards from the soffit for the bridges which needed strengthening work. However, drilling vertical holes may lead to the failure of the existing structure. Hence, it is recommended that the existing structure should be supported wherever possible before the strengthening process begins. If this is not possible, sufficient assessment work should be undertaken to locate the strengthening locations. If it is necessary, traffic management should be requested. It also should be noted that the as-built reinforcement drawings of existing structures should be available to determine where the DE CFRP rods should be installed for strengthening work.

Based on the fibre orientation, FRP composites can be categorised into unidirectional FRP composites and multidirectional FRP composites. Unidirectional CFRP sheets and CFRP rods are used to investigate shear behaviour of corroded RC T-beams

strengthened with CFRP composites.

2.4.3. Parameters that influence FRP contributions in shear

Balaguru et al. (2009) concluded that several parameters will influence FRP shear contribution. These include the stiffness and the thickness/diameter of FRPs, concrete compressive strength, angle of fibre orientation, quality of adhesive used for bonding, bond surface treatment, and anchoring mechanisms. The angle of fibre orientation, quality of adhesive used for bonding, and anchoring mechanisms are considered as less significant. For EB CFRP sheets, only the unidirectional CFRP sheet was studied in this research. The fibre orientation was always perpendicular to the beam axis.

The increase in stiffness and thickness of FRP leads to more shear force being distributed into the FRP. Increasing the concrete compressive strength increases the shear force transferred to the concrete in the compression zone. These effects are similar to the influence factors in beams with shear links.

2.4.4. Failure modes of EB FRP-strengthened RC beams

The failure modes of FRP sheet-strengthened beams were initially observed by Meier et al. (1995a and 1995b); this group identified eight failure modes as listed below:

- Failure of steel reinforcements
- Tensile failure of FRP composite
- Cohesive failure within the adhesive
- Adhesive failure at the FRP to adhesive interface
- Adhesive failure at the concrete to adhesive interface

- Inter-laminar shear within the FRP
- Continuous peeling of FRP sheets or strips
- Crushing of concrete
- Cracking of concrete near the bond line.

However, the typical failure of FRP shear strengthened beams can be summarised by four types of shear failure modes. These are shear failure with FRP rupture, shear failure without FRP rupture, shear failure due to FRP debonding, and failures near mechanical anchors.

Teng et al. (2001) suggested that almost all beams with wrapped FRPs, and some with U-jackets, normally fail with FRP rupture. This type of failure occurs most often with a diagonal tension shear crack of concrete. As the width of the diagonal crack increases, the maximum strain in the FRP eventually reaches its ultimate strain, which often occurs at the lower end of the crack. The FRP immediately breaks along the diagonal shear crack and leads to total failure of the beam in a brittle manner.

Shear failure without FRP rupture means the FRP allows the failed beams to continue to carry a significant load after the concrete failure, but there is no FRP break at failure. An example can be found in Chajes et al. (1995).

Debonding failure is the most common failure for U-jacket and side plate strengthened technologies. Once the FRP starts to peel off, the beam will fail very quickly. The ductility of beams failing is usually very limited. By contrast, mechanical anchors are used to anchor the FRP to the sides of RC beams to prevent FRP peel off from the concrete, so it is possible the failures can occur adjacent to the anchors. Sato et al. (1997) observed that either FRP or concrete may fail locally around the mechanical anchors. Extra care must be taken in design until a better understanding

of these aspects is achieved.

2.4.5. Failure modes of DE FRP-strengthened RC beams

DE strengthening technology was recently developed. Hence, very limited studies have been conducted in this area. The available literature shows that FRP rupture of the DE FRPs barely reach their limited ultimate strain. Hence, the failures normally occur in the concrete near the epoxy. Debonding failure may be due to the limited bonded length. Alternatively, the concrete or shear links might reach their limitations before debonding failure occurs.

The failure modes of DE FRP-strengthened beams are comparable to those of FRP sheet-strengthened beams. Chaallal et al. (2011) studied T-beams of 4,520 *mm* length. The overall dimensions of T-section were 508 *mm* wide by 406 *mm* deep. A total of 12 specimens with different configurations of strengthening method were considered. The study showed that the DE FRP rods increased the shear force capacity by 60%, which is much higher than using EB strengthening technologies. In terms of the failure mode, the EB strengthened beam failed by debonding of FRP sheets and the DE strengthened beam mainly failed in flexure. Chaallal et al. (2011) recommended that the DE method should be further investigated.

2.4.6. Shear design models of shear-strengthened beams

EB FRP sheets have been used to strengthen concrete beams by several researchers; this has been reasonably well studied. For example, Bousselham and Chaallal (2006) studied a series of T-shaped beams with a length of 4,520 *mm*. The overall depth of the RC T-beam was 406 *mm*, and the width of the flange and web

were 508 *mm* and 152 *mm* respectively. The beam was strengthened with a bidirectional U-shaped CFRP composite in the web area. The shear span-to-effective depth ratio, the spacing of the steel shear links, and the number of CFRP layers were the parameters investigated. Test results confirmed that shear capacity gain due to the EB CFRP sheet was less for slender specimens than for deep specimens. Additional shear links decreased the shear capacity gain. The shear capacity gain was not proportional to the CFRP thickness. The most important finding was that no specimen failed by debonding, delamination, or fracture of the CFRP; failure occurred by crushing of the concrete struts.

In Bousselham and Chaallal (2006), RC beams strengthened in shear using EB FRPs showed complex behaviour. However, many factors influenced the shear strength and the failure mode. The complexity of the problem makes it difficult to develop accurate predictive strength models that are suitable for practical design. Nevertheless, several attempts have been made to develop such models, as detailed below.

Most of the existing models consider the overall shear capacity as a sum of the shear contributions of concrete, V_c, shear links, V_s, and FRP composites, V_{frp}. Equation 2.26 expresses this relationship numerically:

$$V_n = V_c + V_s + V_{frp} \qquad (2.26)$$

The shear contributions of the concrete and shear links have been discussed in Section 2.2. In practice, these contributions may be calculated according to provisions in existing design codes, such as Eurocode 2. Such codes underestimate the shear contribution of concrete and steel reinforcement. This will be discussed in

detail in Chapter 6. Equation 2.26 shows that existing models considered that FRP contribution can be separated from concrete and steel reinforcement contributions.

Chaallal et al. (1998) proposed a model to estimate the shear contribution of EB FRPs in ACI 318-95 (1999). The study assumed that EB FRP contributes to shear resistance in the same way as that of internal steel shear reinforcement, and that all FRPs intersected by shear cracks reach their full tensile strength at beam failure unless otherwise limited by insufficient bond lengths. Chen and Teng (2001 and 2003a) reviewed these models and identified that they suffer from two major drawbacks. First, the assumption that the FRP reaches its full tensile strength at beam failure is overly optimistic. Second, the limiting stress level of debonding does not fit well with experimental data. Hence, a large 'safety' factor is required to achieve safe design. Consequently, the use of this concept could lead to misunderstanding and conservative design.

Another design model was prepared by Triantafillou (1998), which suggested that predicting the contribution of FRP to shear resistance is extremely difficult. It depends on the failure mechanism, and the failure mechanism depends on various factors. Hence, he suggested a semi-quantitative approach. The disadvantage of this model is that no distinction is made between the different strengthening schemes or failure modes. As a result, predicted FRP contribution is the same for fully wrapping and side bonding, which is clearly incorrect.

Chen and Teng (2003a and 2003b) and Denton et al. (2004) proposed shear contribution models based on the maximum FRP strain method. This method leads to design formulae for continuous/strips sheets/plate in the design guidance prepared

by the UK Concrete Society and is called Technical Report 55 (TR-55). Equation 2.27 is used to calculate the shear contribution of EB FRP sheets in TR-55:

$$V_{frp} = \frac{A_{frp}}{s_{frp}}\left(d_{frp} - \frac{n_s}{3} l_{t,max} \cos\beta\right) E_{fd} \varepsilon_{fse} (\sin\beta + \cos\beta) \qquad (2.27)$$

where:

A_{frp} Area of FRP for shear strengthening measured perpendicular to the direction of the fibres (*mm²*).

s_{frp} Longitudinal spacing of the FRP laminates used for strengthening (*mm*).

d_{frp} Effective depth of the FRP strengthening, measured from the top of the FRP shear strengthening to the steel tension reinforcement (*mm*).

n_s Wrapped condition factor.

$l_{t,max}$ Anchorage length required to develop full anchorage resistance (*mm*).

β Angle between the principal fibres of the FRP and a line perpendicular to the longitudinal axis of the member (*degrees*).

E_{fd} Tensile modulus of the FRP laminate (*N/mm²*).

ε_{fse} Effective strain in the FRP for shear strengthening

TR-55 considered that shear failure is due to one of three possible mechanisms: loss of aggregate interlock, FRP rupture, and debonding from the surface of the concrete. Several parameters were evaluated in the expression, such as wrapping condition, area of applied FRP, and spacing of FRPs.

Dirar et al. (2012) tested seven RC T-beams consisting of five beams strengthened with unidirectional CFRP sheets along the beam transverse direction. Dirar investigated the shear behaviours by considering different effective depths, loading patterns, and longitudinal reinforcement ratios. The test results showed that the EB CFRP sheets normally increased shear capacity by 9.7 to 26.2%. The different

loading patterns did not influence the shear capacity of the strengthened beams and the prediction of shear force capacity overestimated the contribution of the EB CFRP sheets by a minimum of 41% of the TR-55 predictions. Dirar et al. (2012) also identified that a lower longitudinal reinforcement ratio would change the failure mode from brittle failure to flexure failure. Hence, the proposed shear contribution model still cannot address some of the experimental data; further investigations need to be carried out.

Limited shear contribution models were proposed for strengthening RC structures with DE FRP rods. Desk study showed that only TR-55 and Mofidi et al. (2012) proposed prediction models of shear contribution by DE FRP rods. These models were based on a 45° truss analogy and the maximum FRP strain concept.

TR-55 suggested that the shear contribution due to DE FRP rods can be estimated by Equation 2.28:

$$V_{frp} = \frac{E_{fd}\varepsilon_{fse}A_{frp}}{s_{frp}}\left(h - 2l_{b,max}\right) \qquad (2.28)$$

where:

E_{fd} Tensile modulus of the FRP laminate (*N/mm²*).

ε_{fse} Effective strain in the FRP for shear strengthening.

A_{frp} Area of FRP for shear strengthening measured perpendicular to the direction of the fibres (*mm²*)

s_{frp} Longitudinal spacing of the FRP laminates used for strengthening (*mm*).

h Depth of the strengthened structure (*mm*).

$l_{b,max}$ The effective anchorage length (*mm*).

The required anchorage length at each end of the embedded rods can be assumed by Equation 2.29:

$$l_{b,max} = \frac{\varepsilon_{fse} E_{fd} A_{frp}}{(\pi d_b \tau_b)} \quad (2.29)$$

where:

$l_{b,max}$ The effective anchorage length (*mm*).

d_b Deep embedded FRP rod diameter (*mm*).

τ_b Average bond stress over the length of the anchor, taken as 15 *N/mm²* recommended by TR-55 (*N/mm²*).

The validity of the proposed formulae is based on the high ductility of the bond-slip response of the DE system. Hence, it is possible to rely on a sustained value of bond stress (suggested as 15 *N/mm²*) even for large values of the crack widths (and then large slips) and consider the contribution additive to that of internal shear links after yielding. However, the proposed Equation 2.27 is opportunely conservative, as all rods crossed by the 45° crack whose length is below the required length are disregarded. Hence, the value of the required anchorage length would be sufficiently small that the contribution of any rod with a short length may be disregarded.

Valerio et al. (2009) compared the results of experimental tests and the predictions of TR-55 (2004). However, only five DE CFRP rod-strengthened beams failed in shear. The results showed the mean of predicted-to-actual ratio to be 0.92 (slightly on the conservative side), and the coefficient of variation to be 18.7%, which was not unduly high given the extreme simplicity of the approach. However, the comparisons are based on limited experimental tests. More results of experimental tests and actual structure tests should be carried out to validate the proposed shear strength model of

DE FRP rods.

Mofidi et al. (2012) also proposed prediction formulae of DE FRP rod shear contribution. It was developed based on the same concept as TR-55. However, Mofidi et al. (2012) suggested that for an FRP with a sand-coated surface, the bond stress was 8.4 *MPa* based on the experimental test. To determine the effective bonded length, the slip at maximum bond stress and the bond parameter were 0.08 *mm* and 0.09 respectively. However, these parameters were determined specifically for his experimental test. Hence, the proposed formulae of shear contribution by DE FRP rods were not investigated.

2.5. Surface strain measurements

Strain is a deformation of a solid due to stress. A wide range of techniques have been used to measure strain, such as strain gauges, extensometers, stress and strain determined by machine crosshead motion and optical strain measurement techniques. To measure surface strain of reinforcements, strain gauges and optical strain measurement techniques are the most commonly used methods.

The advantage of using strain gauges (SG) is their low cost, ease of application, and their level of accuracy. However, they are frequently misused as mentioned in Motra et al. (2014). Such misuse will cause uncertainty and error in their measurements.

The fibre optic sensor is a recently developed measurement technology. These sensors can be used to measure strain and/or temperature changes of structures, whether embedded internally or attached externally. Advantages of these sensors over conventional SG sensors include the facts that they are non-corrodible, have

longer sensing lengths, and have the potential to provide a long-term reliable monitoring solution.

2.5.1. Fibre Bragg grating sensors

There are two types of fibre optical sensors that are commonly adopted in practice. They are the Fibre Bragg Grating (FBG) sensor and the distributed optical fibre (FO) cable. Hill et al. (1978) were the first to demonstrate the use of FBG sensors on strain measurement. An FBG sensor is made from two components: a fibre core (consisting of a short segment of distributed Bragg reflector optical fibre) at the centre surrounded with optical fibre. The advantage of using FO cable is that it provides highly distributed continuous strain profiles along the entire length of the optical fibre cables, and potentially allows monitoring of the structure for a long period with lower implementation costs.

2.5.2. Strain measurement using FBG sensors

The fundamental principle of strain measurement by an FBG sensor is Fresnel reflection. Adding a periodic variation to the refractive index of the fibre core generates a wavelength-specific dielectric mirror. The FBG can therefore be used as an inline optical filter to block certain wavelengths, or as a wavelength-specific reflector. As the wavelength of the light changes, the elongation of the material to which the FBG sensor is attached can be measured. Equation 2.30 is used to estimate strain due to the change in wavelength.

$$\frac{\Delta\lambda}{\lambda_B} = k.\varepsilon \qquad (2.30)$$

where:

$\Delta\lambda$ Change in wavelength (*mm*)

λ_B Base wavelength (*mm*)

k Gauge factor

ε Strain

2.5.3. Limitations of using FBG sensors

Ge et al. (2014) compared the measurement ability of four types of strain sensors under controlled temperature in RC beams. Their study included electrical resistance strain gauges (ERSGs), vibrating wire strain gauges, FBG sensors, and FO sensors. Ge et al. (2014) suggested that, although the FO sensors provide continuous temperature or strain profiles, the readings were unable to give highly accurate temperature measurements. A 5°C difference was observed in a dynamic temperature environment. However, the temperature is not an examined factor in this research. As the RC beams were tested at a constant room temperature of 20°C, the temperature effect can be eliminated.

Kreuzer (2006) suggested that FBG works well with new composite materials like glass or carbon fibre-reinforced composites because of the ability of high strain measurements (>10,000 *μm/m*). Lau et al. (2001) embedded FBG sensors into 20 layers of balanced type glass-fibre composite laminates at the interfaces between the 1st and 2nd layer and between the 19th and 20th layers. Externally bonded strain gauges were used to compare the results of FBG sensors when the beam was subjected to a four-point bending test; the strain results were comparable. However, a sufficient embedded length of the sensor is essential to avoid false measurements.

2.5.4. Measuring system of FBG sensors

The technology of FBG is a relatively new method compared with foil strain gauge technology. It provides many advantages in special applications. However, there are still some problems stemming from the requirement to induce the strain precisely into the fibre. These include embedding and gluing procedures for the fibres, temperature correction, and prevention of humidity dependency. Additionally, the issues that are well-known from foil strain gauge technology are also applicable to FBGs.

An independent FBG analyser is generally connected between the FBG cables and the PC. This allows the PC to measure and record the FBG signals. The data acquisition software permits online graphics and post-processing of the data.

2.6. Summary and discussion

This chapter has provided an overview of the shear behaviour of corroded RC beams strengthened with FRP composite. Shear design is considered in the ultimate limit state design stage. Such design stages normally deal with the limit states of structure approaching their collapse state. The independent effects of concrete, shear links, shear link corrosion levels and FRP strengthening methods have been well documented in many publications; see Table 2.6.1.

Steel shear reinforcement is another key parameter that influences overall shear contribution. However, the mechanical and physical properties will be highly affected by the corrosion level of shear links. Research has shown that the steel reinforcement will completely lose its ductility property and turn into a brittle material once a corrosion level of 12% has been reached. Thus, the higher the corrosion

level, the less the yield strength, and consequently, the lower the shear contribution.

Studies on shear strengthening with CFRP composites have been well documented for EB CFRP sheet technology. However, shear strengthening with EB CFRP sheets has a great deal of restrictions compared to DE CFRP rod strengthened technology, such as access to the soffit of the bridge, environmental conditions and end anchorage problems. Strengthening with DE CFRP rods offers a better bond performance between the concrete and the FRP reinforcement. It also offers an easy construction solution compared to EB CFRP sheet strengthening technology.

Research studies investigating the shear behaviour of RC beams strengthened using the DE technique is scarce. Moreover, very few studies have considered the behaviour of CFRP shear-strengthened RC T-beams with corroded shear links (El-Maaddawy and Chekfeh, 2013). It should be noted that RC T-beams adequately simulate the slab-on-beams construction method. In reality, the majority of bridge superstructures behave as T-beams made up of beams and decks rather than rectangular beams. However, the results should be applicable to rectangular beams as well. Furthermore, to date there are no research studies comparing the effectiveness of the EB and DE CFRP shear strengthening systems in the context of RC T-beams with corroded shear reinforcement.

This literature review has also shown that concrete compressive strength is one of the key parameters that influence the shear contribution of the concrete. An Increase in concrete compressive strength leads to more overall shear capacity because the contributions of compression concrete and interface shear capacity are increased. The bond strength of steel-to-concrete interface is also increased as the concrete

compressive strength increases, similar to the interface of the CFRP rod-to-concrete. However, TR-55 does not consider the effects of concrete strength on the shear contribution of DE CFRP rods.

Table 2.6.1: Knowledge Gap

Index	Publications	Number of Tested Beams	Properties and Parameters																								
			Geometry						Corrosion Control					Strengthing Scheme								Loading			Behaviour	
					a_v/d Ratio																						
			Rectangular Section	T-Section	ls/d<1	1<ls/d<2.5	2.5<ls/d<6.5	6.5<ls/d	Natural	Galvanostatic Method	Enviroment Control	Main Reinforcements	Stirrups	Carbon	Aramid	Glass	Externally Bonded (Sheets)	Deep embedment (Bars)	Strength Angle = 90	Strength Angle ≠ 90	Monotonic	Cyclic Loading	Fatigue	Flexure	Shear
1	Zeris et al. (2009)	8	■				■							■		■	■		■		■	■		■	■	
2	Pellegrino et al. (2006)	12	■				■							■			■		■		■			■		■
3	Deniaud et al. (2003)	8		■			■							■		■	■		■		■			■		■
4	Azad et al. (2007)	56	■							■		■	■								■			■		■
5	Higgins et al. (2006)	14	■	■		■				■		■	■								■					■
6	Xia et al. (2011)	18	■			■				■	■		■								■					■
7	Al-Hammoud et al. (2011)	30	■				■					■	■	■			■		■				■	■		■
8	Al-Saidy et al. (2011)	15	■					■		■		■		■			■		■		■			■		
9	Yuan et al. (2007)	7	■				■			■	■	■									■			■		■
10	Anil (2006)	6		■			■							■			■			■		■			■	
11	Ou et al. (2011)	5	■				■			■		■	■									■		■		■
12	Barros and Dalfre (2012)	14	■				■											■	■	■	■					
13	Chaallal et al. (2011)	12		■			■							■			■	■	■		■					
14	Breveglieri et al. (2015)	19		■			■							■				■	■	■	■					
15	Dirar et al. (2012)	7		■			■							■			■				■					
16	Mofidi and Chaallal (2014)	12		■			■							■			■				■					
17	Almusallam (2001)		■							■		■	■											■		
18	Ann et al. (2007)																									
19	Yuan et al. (2010)									■	■	■	■													
20	Du et al. (2005)									■		■	■													
21	Cairns (1995)		■																					■	■	
22	Rodriguez et al. (1997)		■							■		■	■											■	■	
23	Deniaud et al. (2004)		■	■										■			■		■		■			■	■	
	Current Research	*9*		■			■			■			■	■			■		■		■					■

CHAPTER 3: EXPERIMENTAL PROGRAMME

3.1. Introduction

As mentioned in Chapter 1, large amounts of money are spent on repairing corroded reinforced concrete (RC) structures. Corrosion of the internal shear links can have a detrimental impact on the shear capacity of RC beams. In this chapter, the objectives of the experimental work are introduced in Section 3.1 and the tests on uncorroded and corroded RC T-beams is described in Section 3.2. The relevant materials used in the tests, the accelerated corrosion methodology employed and the strengthening schemes used are summarised in Sections 3.3, 3.4 and 3.5 respectively. Sections 3.6 and 3.7 describe the test setup and the instrumentation of the experimental work respectively. Finally, Section 3.8 presents a summary of the keynotes in the experimental programme.

The aim of the experimental work was to investigate the shear behaviour of corroded and uncorroded RC T-beams shear strengthened with CFRP systems. The objectives of the experimental work were:

1. *To study the effect of shear link corrosion levels on the shear performance of T-beams*

Three RC T-beams with different shear link corrosion levels (0% / uncorroded, 7%, and 15%) were tested. The beams were designed to fail in shear. The two beams subjected to the accelerated corrosion process had an addition of 3% calcium chloride by weight of cement to the concrete mixture.

2. *To examine the effect of strengthening methods on the shear performance of uncorroded and corroded RC T-beams*

Six more specimens strengthened with either CFRP sheets or CFRP rods were tested at the shear link corrosion level of 0% (uncorroded), 7% and 15%. The research variable was the type of CFRP strengthening scheme (deep embedment (DE) or externally bonded (EB)).

3.2. Test program

As described in Section 3.1, a total of nine specimens were manufactured and tested. The details of the specimens are summarised in Section 3.2.1. Section 3.2.2 describes the fabrication, casting and curing of the specimens.

3.2.1. *Description of test specimens*

The research programme consisted of nine RC T-beams in three categories. Table 3.2.1 shows the details of the test specimens.

Table 3.2.1: Test Specimens

Specimen Reference	Theoretical Corrosion Level	Strengthening Scheme
N00	0 %	-
N07	7 %	-
N15	15 %	-
B00	0 %	CFRP rods
B07	7 %	CFRP rods
B15	15 %	CFRP rods
S00	0 %	CFRP sheets
S07	7 %	CFRP sheets
S15	15 %	CFRP sheets

The specimens with references initial letter ‘N’ were un-strengthened beams; specimens with references initial letter ‘B’ were CFRP rod-strengthened specimens; specimens with references initial letter ‘S’ were CFRP sheet-strengthened specimens. The specimens marked with ‘00’ were un-corroded specimens; those marked with ‘07’ were targeted to have a 7% corrosion level, and specimens marked with ‘15’ were targeted to have a 15% corrosion level.

The tested specimens were 2,700 *mm* long (l) and the clear span was 2,200 *mm*. The load was applied at a distance of 200 *mm* from the centre of the span. ‘Stiffness’ is the ratio of maximum shear force to soffit beam deflection in line with the loading jack. Hence, although the load was not applied at the centre of the RC T-beams, the effect of unbalanced shear links to experimental and numerical results was considered to be insignificant. The total depth (h), web width (b_w), flange width (f_w), and flange thickness (t_f) were 360 *mm*, 125 *mm*, 260 *mm*, and 100 *mm* respectively. The specimens had a shear span (a_v) to effective depth (d) ratio of 3.05 and an effective depth (d) of 295 *mm*. All specimens were designed to fail in shear. Figure 3.2.1 provides further details of the RC T-beams.

All specimens were reinforced with steel flexural and shear reinforcement. The longitudinal reinforcement consisted of three 20 *mm* (diameter) compression reinforcements at the top of the flange and four 25 *mm* (diameter) tension reinforcements in two layers at the bottom of the web. The compression reinforcements were anchored with a 230 *mm (width, w_{at})* x 50 *mm (height, h_{at})* x 25 *mm (thickness, t_{at})* steel plate at each end. The tension reinforcements were anchored with 100 *mm (width, w_{ab})* x 100 *mm (height, h_{ab})* x 25 *mm (thickness, t_{ab})*

steel plate at each end to prevent bond failure.

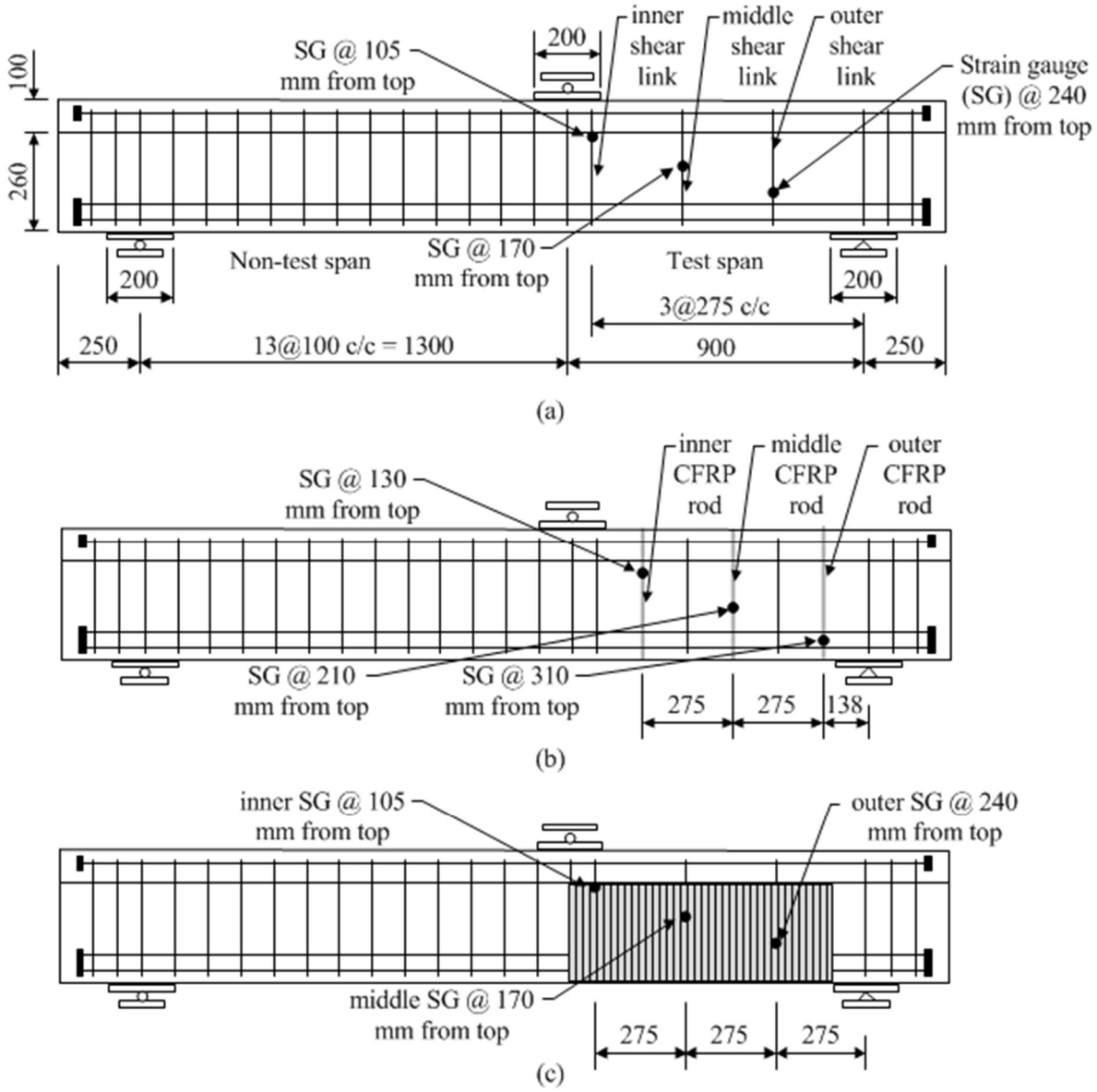

Figure 3.2.1: Test setup

- (a) unstrengthened beams, (b) DE CFRP strengthened beams, and (c) EB CFRP strengthened beams – all dimensions in *mm*

The internal steel shear links were 8 *mm* in diameter. The spacing of the steel shear links was 275 *mm* centre-to-centre within the tested span (900 *mm* in length from the centre of the support to the centre of the loading jack) and 100 *mm* centre-to-centre within the non-test span (1300 *mm* in length from the centre of the loading plate to

the centre of the other support). The CFRP rod-strengthened specimens were reinforced with additional 10 *mm* CFRP rods embedded between the shear links in the tested span at a spacing (s_{CFRP}) of 275 *mm* centre-to-centre. The CFRP sheet-strengthened specimens had one layer of CFRP sheet at the sides and soffit of the test span web, from the inner edge of the support to the centre line of the loading jack (approximately 800 *mm* in length). The bottom corners of the T-beams at the test span were rounded carefully to avoid stress concentrations in the CFRP sheets.

Beam N00 was tested straight after a 28-day curing period. Beam S00 and Beam B00 were cured for 28 days, strengthened with CFRP composites and then tested. The rest of the specimens were cured for 28 days and then subjected to an accelerated corrosion process as detailed in Section 3.4. The un-strengthened specimens were tested straight after the completion of the accelerated corrosion process, whereas other specimens were strengthened with CFRP composites before testing.

3.2.2. *Fabrication, casting, and curing*

The reinforcement cages were prepared before casting (see Figure 3.2.2 for a typical reinforcement cage of un-corroded beams and Figure 3.2.3 for a typical reinforcement cage of corroded beams). The cages of the corroded specimens, except the tested span shear links, were coated with aluminium pigmented epoxy to provide corrosion protection. The specimens were cast one at a time using the same concrete mixture proportions (cement: water: aggregate: sand = 1: 0.65: 2: 3) and a maximum aggregate size of 10 *mm*. An open-top formwork (see Figure 3.2.4) was prepared to cast the specimens. In addition to each specimen, nine cubes, six

cylinders and three prisms were also cast using the same concrete mixture. All of these were de-moulded on the second day of casting and then left to dry in ambient air for a minimum of a 28-day period inside the laboratory (room temperature was around 20 degrees). For the specimens subjected to the accelerated corrosion process (see Figure 3.2.5), a 3% calcium chloride by mass of cement was added to the concrete mixture to provide better electrical conductivity and chloride electron penetration. For the specimens strengthened with CFRP rods, three 15 *mm* PVC rods were installed at the locations where the CFRP rods would be installed (Figure 3.2.6). The rods were taken out on the third day of casting and the holes were blocked with rubber plugs for the beams subjected to the accelerated corrosion process. For the specimens strengthened with CFRP sheets, two round-corners (Figure 3.2.7) were fixed into the mould at the bottom corners of the location where the CFRP sheets would be installed.

Figure 3.2.2: Reinforcement cage for un-corroded specimens

Figure 3.2.3: Reinforcement cage for corroded specimens

Figure 3.2.4: Open-top mould filled with fresh concrete

Figure 3.2.5: Specimens subjected to the accelerated corrosion process

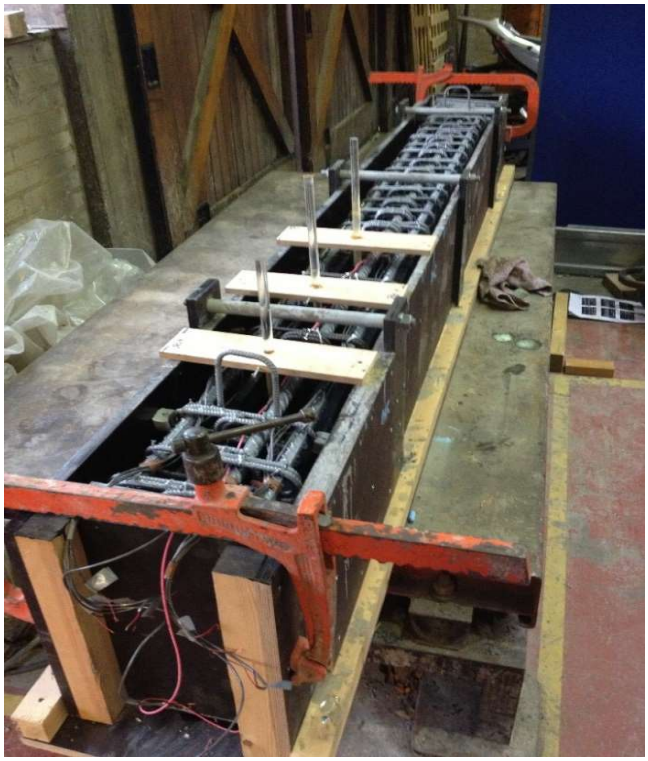

Figure 3.2.6: PVC rods installed at the locations of the CFRP rods in the mould

Figure 3.2.7: Rounded corner at the bottom of web for specimens strengthened with CFRP sheets

3.3. Material properties

This research involved four main materials which will be discussed in this section.

3.3.1. *Concrete*

- *Concrete mixture*

The RC T-beams were cast by using the same proportional concrete mixture (cement: water: aggregate: sand = 1: 0.65: 2: 3). The targeted concrete compressive strength was 25 *MPa* after a 28-day curing period. This research is to investigate the strengthening performance on the existing structures. Such structures are expected to have a low concrete strength (25 *MPa*) because of concrete deterioration. As the sand and aggregate were stored outside the laboratory, a moisture test was carried

out on the day of casting for each specimen. The actual proportions for each specimen were listed in Table 3.3.1. 3% calcium chloride (by mass of the cement) was added to the concrete mixture of corroded specimens. By adding 3% calcium chloride into the mixture, the strength of the concrete was increased due to the increase of calcium ions, which improved the electrical conductivity by introducing more free chloride irons. With more free chloride irons, the possibility of corrosion will more likely.

Table 3.3.1: Summary of concrete mixtures

	Cement (*kg*)	**Water (*kg*)**	**Sand (*kg*)**	**Aggregate (*kg*)**	**Calcium Chloride (*kg*)**
Beam N00	68.7	23.9	147.3	216.8	-
Beam N07	69.3	27.2	147.7	216.4	2.08
Beam N15	68.7	16.3	152.0	219.7	2.06
Beam B00	69.3	25.7	149.1	216.5	-
Beam B07	69.3	34.4	142.5	214.5	2.08
Beam B15	69.3	22.9	150.5	217.9	2.08
Beam S00	68.7	22.8	148.4	216.8	-
Beam S07	69.3	30.3	145.6	215.4	2.08
Beam S15	69.3	25.3	149.5	216.6	2.08

- *Concrete mixing*

In accordance with the concrete mixture proportions given in Table 3.3.1, the quantities of cement, coarse aggregate, fine aggregate, water and calcium chloride were carefully weighed using a platform balance, prior to each concrete mixing. For the corroded specimens, the calcium chloride was first dissolved in the mixing water in order to distribute it throughout the concrete mix uniformly. Then the fine aggregate, coarse aggregate and cement were put into the electrically operated

mechanical mixer and mixed for about three minutes. The water was then poured into the mixer. After another five to seven minutes mixing by the mechanical mixer until the concrete mix had an even consistency with a uniform colour, the concrete mix was ready to be cast.

- *Concrete casting and curing*

Before casting, all the moulds used for the specimens and samples were oiled and placed on a vibrating table. The vibrating table helped the mixture to liquefy and reduce the internal friction of the mix components of cement, aggregate and water. After the positions of the reinforcements in the moulds has been checked, the concrete was placed into the moulds in two approximately equal layers. Following the placement of each layer, the concrete mixture was vibrated for approximately two minutes. Once the concrete specimens and samples had been cast, they were covered with polythene to prevent the water content in the fresh concrete from evaporating too early. The specimens were de-moulded 24 hours after pouring and left covered with polythene for another 27 days. The specimens were then either tested or subjected to an accelerated corrosion process.

- *Concrete standard testing*

In order to examine the concrete quality throughout the investigation and to determine the concrete strength at different testing stages, standard tests on the hardened concrete were carried out in accordance with BS EN 12390 (2000 and 2009).

During the casting of the concrete specimens, three types of concrete samples, nine 100 *mm (height, h_{cu})* x 100 *mm (width, w_{cu})* x 100 *mm (depth, d_{cu})* cubes, six 200 *mm*

(height, h_{cy}) x 100 *mm (diameter, d_{cy})* cylinders and three 100 *mm (width, w_p)* x 100 *mm (height, h_p)* x 500 *mm (length, l_p)* prisms, were also prepared from each batch of fresh concrete. All the samples were cast and cured together with the concrete specimens, and tested following the procedures set out in BS EN 12390 (2000 and 2009).

The cubes were tested in compression using a Denison testing machine to determine the compressive strength, f_{cu}, of each concrete cube. The cube tests were conducted on the day when a specimen was loaded to failure. The average strength of six samples was taken as the cube compressive strength on the day when a specimen was loaded to failure. This concrete compressive strength was also used in the finite element analysis.

Table 3.3.2: Concrete properties

Beam designation	Cube compressive strength (N/mm^2)		Cylinder split tensile strength (N/mm^2)		Flexural strength (N/mm^2)	
	Average(1)	Standard deviation(1)	Average(2)	Standard deviation(2)	Average(2)	Standard deviation(2)
N00	26.3	2.4	2.3	0.7	4.1	0.2
N07	35.1	1.0	2.6	0.2	5.4	0.4
N15	41.8	2.1	2.2	0.1	6.1	0.4
B00	21.7	1.3	1.5	0.2	3.1	0.2
B07	37.0	1.0	2.0	0.4	5.1	0.2
B15	37.0	1.3	1.9	0.1	5.3	0.4
S00	37.0	1.4	2.4	0	4.2	0.7
S07	36.8	0.9	2.5	0.3	5.4	0.5
S15	42.9	1.3	2.1	0.4	6.1	0.3

(1) Based on at least five samples per beam

(2) Based on three samples per beam

Three concrete cylinders with a diameter of 100 *mm* and a length of 200 *mm* were loaded axially until failure. This indicated the cylinder compressive strength of the tested concrete specimen, f_{cm}. The remaining three concrete cylinders were used to determine the split tensile strength, f_t. The concrete prisms were tested to failure in a four-point bending configuration to determine the flexural tensile strength, f_r. Tests on the concrete cylinder and prism samples were also carried out on the day when the corresponding specimen was loaded to failure, in accordance with BS EN 12390 (2009). The values of cube compressive strength, cylinder split tensile strength, and flexural strength, as obtained on day of test (i.e. either 28 days after casting for the un-corroded RC T-beams or after the accelerated corrosion process for the corroded RC T-beams), are summarised in Table 3.3.2. The targeted cube compressive strength (f_{cu}) was 25 N/mm^2. Table 3.3.2 shows that the concrete compressive strengths were different between the targeted and actual cube compressive strength values. This is due to unintended quality control issues where the calcium chloride should also added into uncorroded beam mixtures. In order to avoid such an unfortunate situation, it is recommended that, where possible, all beams should be cast at the same time and using the same concrete batch. This should at least ensure that all beams have comparable, if not similar, concrete strength values.

3.3.2. *Steel reinforcement*

Reinforcements of three different diameters, 8 *mm*, 20 *mm* and 25 *mm,* were used in this study. The nominal characteristic strengths of the 8 *mm* reinforcements were slightly different at tested span and non-tested span as they were ordered at different times with different tensile strengths. The reinforcement with lower strength was

selected for the test span where the designed-failure load should be within the loading machine capacity. According to BS 4449:2005, the rib pattern of the 8 *mm* and 25 *mm* reinforcements was similar to that of B500B. The rib pattern of the 20 *mm* reinforcement was similar to that of B500C. A SANS MT8000 electromechanical universal testing machine (load capacity = 100 *kN*) was used to test the actual mechanical properties of the 8 *mm* reinforcements. A Dennison universal testing machine (load capacity = 500 *kN*) was used to test the actual mechanical properties of the 20 *mm* and 25 *mm* reinforcements. All of the reinforcements were supplied by the same supplier and delivered at two different times. A minimum of three reinforcements for each type, each diameter and each delivery were tested. The test results are summarised in Table 3.3.3. In general, the elasticity modulus of steel is normally around 200,000 *MPa*. However, a lower elasticity modulus of steel was found in the steel reinforcements. Dirar et al (2012) used 8 *mm* reinforcement in his study. The average elasticity modulus was 185,714 *MPa,* which was comparable to the elasticity modulus obtained.

Table 3.3.3: Mechanical properties of non-corroded reinforcement

Rebar reference	Modulus of elasticity (N/mm^2)	Yield strength (N/mm^2)	Ultimate strength (N/mm^2)
8mm test span	185600	542	664
8mm non-test span	182600	573	655
20mm compression	179200	576	707
25mm tension	180000	537	669

3.3.3. *Carbon fibre reinforced polymer rods*

Aslan 200 carbon fibre reinforced polymer (CFRP) rods were used to strengthen

three out of the nine specimens. The diameter of each rod was 10 *mm* and it was coated with sand. The nominal area, guaranteed tensile strength, tensile modulus of elasticity and ultimate strain were 71.26 mm^2, 2172 N/mm^2, 124,000 N/mm^2 and 1.75% respectively. Hilti RE 500 two-part adhesive was used for installing the Aslan 200 CFRP rods. The mechanical properties of Hilti RE 500 adhesive are summarised in Table 3.3.4.

Table 3.3.4: Mechanical properties of Hilti RE 500 adhesive

Material	Property	Value
Hilti RE 500 Adhesive (Cured Adhesive)	Bond Strength ASTM C882-91 2 day cure 7 day cure	 12.4 N/mm^2 12.4 N/mm^2
	Compressive Strength ASTM D-695-96	82.7 N/mm^2
	Compressive Modulus ASTM D-695-96	1493 N/mm^2
	Tensile Strength 7 day ASTM D-695-97	43.5 N/mm^2
	Elongation at break ASTM D-638-97	2.0 %
	Heat Deflection Temperature ASTM D-648-95	63 *degrees*

3.3.4. *Carbon fibre reinforced polymer sheets*

Tyfo SCH-41 composite is a unidirectional woven carbon fibre fabric for a wet application process. The fabric design thickness was 1 *mm* per layer. The width of the fabric sheet was 600 *mm*. The dry fibre tensile strength was 3,790 N/mm^2, the tensile elastic modulus was 230,000 N/mm^2 and the elongation at break was 1.7%. These are nominal values and supplied by Tyfo. The laminate properties were adopted in the numerical simulation (see Table 3.3.5 for details). Tyfo S epoxy is a 2-

part epoxy impregnation resin used to glue the Tyfo SCH-41 composite onto the concrete surface. The mechanical and physical properties of Tyfo SCH-41 composite and Tyfo S epoxy are summarised in Table 3.3.5.

Table 3.3.5: Mechanical and physical properties of SCH-41 composite and Tyfo S epoxy

Material	Property	Value
Dry Fibre Properties	Tensile strength	3,790 N/mm^2 (nominal)
	Tensile E-modulus	230,000 N/mm^2 (nominal)
	Elongation at break	1.7% (nominal)
Laminate Properties	Laminate thickness	1.0 *mm* per layer
	Ultimate tensile strength in primary fibre direction	986 N/mm^2
	Tensile E-modulus	95,800 N/mm^2
	Longitudinal compressive strength	344.8 N/mm^2
	Longitudinal compressive modulus	77,200 N/mm^2
Tyfo S Epoxy	Tensile Strength	72.4 N/mm^2
	Tensile modulus	3,180 N/mm^2
	Elongation percent	5%
	Flexural strength	123.4 N/mm^2
	Flexural modulus	3,120 N/mm^2

3.3.5. *Cement, aggregate and calcium chloride*

The cement, aggregate (sand and gravel) and calcium chloride were delivered by local suppliers. Ordinary Portland Cement (OPC) manufactured by Rugby Cement plc was used for the concrete mix. This CEM II/B-V 32,5N Portland - fly ash cement is produced according to BS EN 197-1. 10 *mm* maximum size gravel from Edwin Richards Quarry and sand from Welford Pit were used as the coarse and fine

aggregate for the concrete mixture. The calcium chloride was used in the form of "fused coarse" and was supplied by ReAgent.

3.4. Accelerated corrosion

Figure 3.4.1: Reinforcing cage coated with aluminium pigmented epoxy (except for the shear links at tested span)

As listed in Table 3.2.1, six out of the nine specimens were subjected to an accelerated corrosion process, also known as the Galvanostatic method. Apart from the outer, middle and inner shear links within the test span, the internal flexural steel and shear reinforcement, as well as the end plates, were coated with aluminium pigmented epoxy to provide corrosion protection; Figure 3.4.1 shows that the reinforcing cage is coated with aluminium pigmented epoxy, except the test span shear links. Figure 3.4.2 shows a schematic of the accelerated corrosion setup. After a 28-day curing period, the test span was encircled with a stainless steel sheet and placed within a plastic tank containing a 3% sodium chloride (NaCl) solution. The

NaCl solution level was maintained to just above the top surface of the stainless steel sheet during the corroding period.

The stainless steel sheet was set up 15 *mm* apart from the concrete surface and was connected to the cathode of the direct current (DC) power supply unit. The inner, middle and outer (also known as 1st, 2nd and 3rd in Figure 3.4.2) steel shear links in Beam N15 were each connected to the positive terminals of the DC power supply unit.

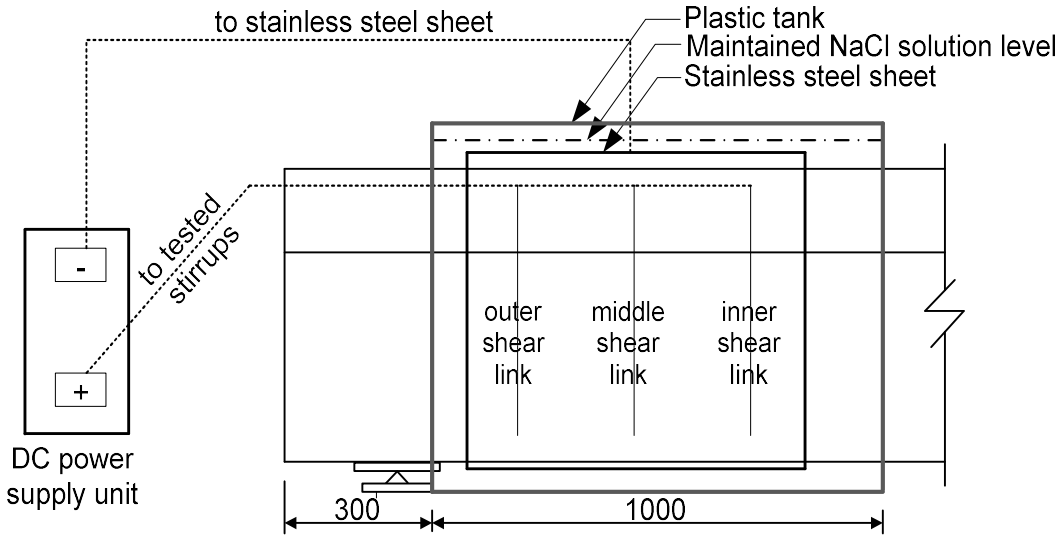

Figure 3.4.2: Accelerated corrosion setup
- Azad et al (2007)

A constant current of about 83.3 *mA* (1.83 $\mu A/mm^2$) per shear link was applied throughout the corrosion process, which lasted for 53 days. In the case of Beam B15, the inner, middle and outer steel shear links were connected to each other by electrical wiring and then to the anode of the DC power supply unit. A constant current of about 188.9 *mA* (1.40 $\mu A/mm^2$) was applied during the corrosion process,

which lasted for about 70 days. The inner, middle and outer steel shear links in the remaining specimens were connected in the same way as that of Beam N15. A constant current density of 2.0 $\mu A/mm^2$ (about 90 *mA* per shear link) was applied during the corrosion process, which lasted for 23 days for the 7% target corroded specimens and 49 days for the 15% target corroded specimens. These constant current densities were monitored from the DC power supply unit and maintained on a daily basis.

3.4.1. *Preparation of the specimens for the accelerated corrosion process*

The specimens were lifted up onto the supports by a crane. The stainless steel sheet (see Figure 3.4.3) was secured onto the target corroded location at the tested span (see Figure 3.4.4). A plastic tank was loaded onto a wooden board and jacked up from the bottom until it was adequately secured to the specimen. The jack was then locked into its position and the plastic tank was sealed with Sikadur epoxy onto the T-beams. Two additional plastic sheets were used to complete the tank (see Figure 3.4.5).

Figure 3.4.3: Stainless steel sheet with 15*mm* wooden spacers

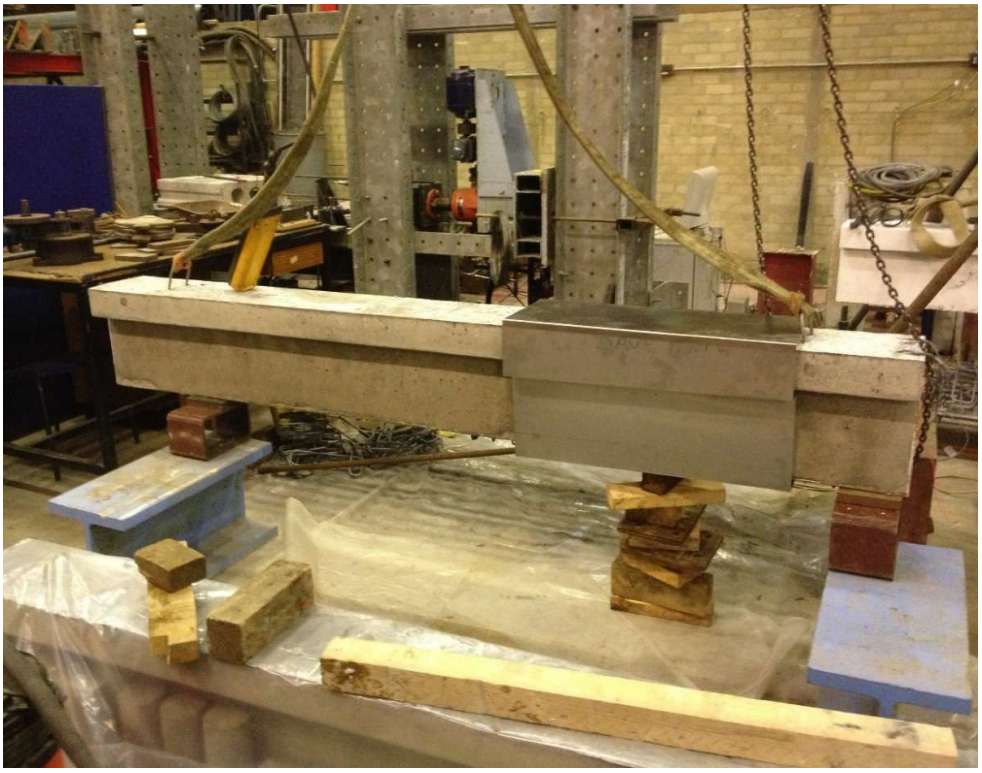

Figure 3.4.4: Stainless steel sheet secured on the targeted location

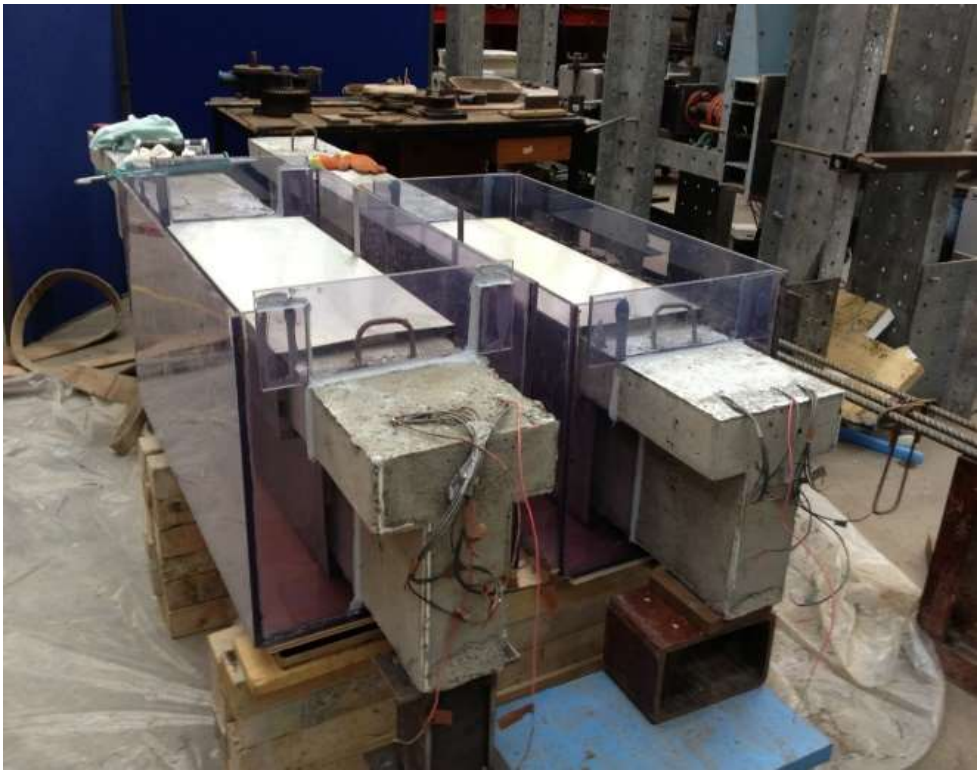

Figure 3.4.5: Specimens ready for the accelerated corrosion process

The tank was filled with water on the first day to test for leakage. If any leakage was identified, the tank would be emptied and left to dry, allowing the leaks to be repaired. This cycle would be repeated until all leakage was stopped; then the tank would be emptied again and filled with 3% sodium chloride solution. The DC power supply unit was connected to the stainless steel and the test span shear links (see Figure 3.4.6). The current was adjusted according to the value calculated from Faraday's law. The specimen was subjected to the accelerated corrosion process for the required period. During this period, the 3% sodium chloride solution was maintained to the level just above the stainless steel sheet. Barriers were used to prevent anyone working near the specimen accidently stopping the accelerated corrosion process.

Figure 3.4.6: Specimens connected to the DC power supply unit

Once the accelerated corrosion process was completed, the solution was emptied from the tank (see Figure 3.4.7). The jack was released in order to remove the plastic tank and the stainless steel sheet (see Figure 3.4.8). The test span was cleaned with fresh tap water and any remaining Sikadur epoxy was also removed from the concrete surface (see Figure 3.4.9). The specimen was left to dry for a minimum period of a week. Any cracks due to the accelerated corrosion process were marked on the surface of the concrete and photographs were taken. The specimen was then ready for strengthening and testing.

Figure 3.4.7: Emptying the sodium chloride solution from the plastic tank

Figure 3.4.8: A beam with the plastic tank and stainless steel sheet removed

Figure 3.4.9: A specimen cleaned with water

It should be noted that rust will form on the entire surface of the steel reinforcement and the targeted corrosion level can be reached in a short time by using the Galvanostatic method. In reality, rust forms from the near face of the concrete to the far side of the reinforcement and takes a long time to reach the targeted corrosion level. However, both the Galvanostatic method and the artificial climate control method reduce the loading capacity and ductile characteristics of the reinforcement, and transform the failure mode from ductile to brittle. Yuan et al. (2007) showed that the results between the Galvanostatic method and the artificial climate control method are comparable.

3.4.2. *Extraction of the corroded shear links*

In order to measure the mass loss of the corroded shear links, the corroded shear links were carefully extracted from the test span once the experimental test was completed. To remove the tested span shear links, the following steps were considered and followed:

1. An overhead crane was used to move the tested specimen from its location onto a carrying trolley car.
2. The estimated position of the corroded shear links was checked against the construction drawings and the locations were marked on the surface of the concrete web.
3. A hammer drill concrete breaker was used to remove the surrounding concrete around the shear links at the test span. It should be noted that the vibration will remove some of the corrosion (see Figure 3.4.10) from the surface of corroded shear links.
4. A wire cutter was used to remove the shear links, which were tied to the longitudinal reinforcements (see Figure 3.4.11).
5. A metal cutting saw was used to cut the compressive and tensile reinforcements at the centre of the loading plate.
6. The corroded shear links were removed from the longitudinal reinforcements.
7. The extracted shear links were marked with their beam reference and location.
8. A wire brush was used to remove the residual concrete bits from the surface of the shear links.

After step 8, the shear links were ready for the mass loss analysis which checked their actual weight loss during the accelerated corrosion process.

Figure 3.4.10: Corrosion around the shear links

Figure 3.4.11: Extracting the tested span shear links

3.4.3. *Mass loss analysis*

Almusallam (2001) showed that corrosion levels of about 12.6% resulted in significant reductions in the yield and ultimate stresses and strains of steel reinforcements. Hence, the targeted corrosion levels were 7% and 12% in order to examine the effects of low and moderate corrosion levels on shear strength. The theoretical time required to achieve such corrosion levels was calculated by Faraday's law. The actual corrosion levels achieved at the end of the accelerated corrosion process were determined using gravimetric mass loss analysis.

Figure 3.4.12: Extracted tested span shear links

Before casting the corroded specimens, the original mass (m_o) of each of the outer, middle and inner steel shear links within each test span was recorded. After testing, the corroded shear links were extracted from the concrete (see Figure 3.4.12) and the following procedure was used to calculate the actual corrosion level. Additionally,

an un-corroded reinforcement was subjected to the process in parallel to measure any steel loss per unit length during this process. Gravimetric mass loss analysis procedures:

1. A corroded shear link was cleaned with a wire brush after extraction from the concrete.
2. The initial mass (m_i) of the cleaned shear link was recorded.
3. The shear link was attached to a tie (for health and safety purposes) and the total mass of the shear link and tie (m_1) was recorded.
4. The shear link was suspended using the tie in a 3.5% hydrochloric acid solution for 15 minutes; see Figure 3.4.13 and Figure 3.4.16 for 7% and 12% corroded shear links respectively.
5. The shear link was removed from the hydrochloric acid solution and cleaned with water.
6. The shear link was cleaned with a wire brush and allowed to dry for 5 minutes while suspended in the air; see Figure 3.4.14 and Figure 3.4.17 for 7% and 12% corroded shear links respectively. The total mass of the shear link and tie (m_2) was recorded.
7. Steps 4 to 6 were repeated until the mass loss was negligible.
8. The shear link was cleaned and allowed to dry for 24 hours while suspended in the air; see Figure 3.4.15 and Figure 3.4.18 for 7% and 12% corroded shear links respectively. The total mass of the shear link and tie was recorded.
9. The remaining acid was checked by HP paper to confirm the acid was not totally used up in the chemical reactions; see Figure 3.4.19.

The final mass of the shear link and tie (m_f) was measured according to ASTM G1-03. The mass of the tie (m_t) was calculated using Equation 3.1, and the actual corrosion level was calculated using Equation 3.2.

$$m_t = m_1 - m_i \tag{3.1}$$

$$Corrosion\ level = (m_o - m_f + m_t)/m_o \tag{3.2}$$

Figure 3.4.13: 7% corroded shear links in 3.5% hydrochloric acid solution

Figure 3.4.14: 7% corroded shear links dried in the air after being cleaned with water

Figure 3.4.15: 7% corroded shear links after 24 hours of being suspended in the air

Figure 3.4.16: 12% corroded shear links in 3.5% hydrochloric acid solution

Figure 3.4.17: 12% corroded shear links dried in the air after being cleaned with water

Figure 3.4.18: 12% corroded shear links after 24 hours of being suspended in the air

Figure 3.4.19: HP paper used to confirm the acidity of the solution

3.4.4. *Testing techniques for mechanical properties of corroded reinforcement*

After the mass loss analysis, tests were carried out on the corroded shear links to assess their mechanical and physical properties. It was difficult to measure the corroded reinforcement diameter as most of the shear links were not corroded evenly. Therefore, eight diameter readings were taken for each corroded shear link. The averaged reading was considered as the remaining diameter, d_c. The weights of the flange and web shear links were also recorded. As the length of the flange and web shear links were recorded before casting, the theoretical remaining diameter, d_{ct}, could be calculated, as the density of steel is 7,900 kg/m^3. The theoretical remaining diameter was compared with the averaged reading to determine the final remaining diameter.

For the mechanical property test, a SANS universal testing machine (CMT8000) was used to obtain the stress-strain relationship of the corroded shear links. The web shear links were cut into two parts as a 'C' shape. Some parts of the bend and the heavily corroded reinforcements were not suitable for testing. However, it is important to note that the stress-strain curve was drawn based on the remaining diameter of the corroded reinforcements. The SANS universal testing machine gave the elasticity and strength of the corroded reinforcements directly. The test was setup according to BS EN ISO 15630-1-2010.

3.5. Installation of the CFRP strengthening systems

In order to achieve an adequate bond between the concrete and CFRP composites, the targeted concrete surface was prepared in advance. Six out of the nine specimens were separated into two groups. Each group was either strengthened with DE CFRP rods or EB CFRP sheets. The two un-corroded specimens were strengthened straight after casting. The four corroded specimens were strengthened after the accelerated corrosion process. The detailed CFRP composite installation steps are described in Sections 3.5.1 and 3.5.2.

3.5.1. *Installation of deep embedment CFRP rods*

In order to install the CFRP rods, 15 *mm* diameter vertical holes were created in the test span through the centreline of the cross-section at 138 *mm*, 413 *mm* and 688 *mm* from the centreline of the support; see Figure 3.2.1(b) for details. The vertical holes were created by installing 15 *mm* diameter acrylic rods at the required positions within the steel reinforcement cage, before casting the concrete. The acrylic rods

were removed from the concrete two days after casting. For the corroded beams, the vertical holes were blocked with rubber plugs before starting the accelerated corrosion process.

Prior to installing the CFRP rods, the holes were cleaned using a wire brush (see Figure 3.5.1) and compressed air to remove any cement or aggregate residues. The lower ends of the holes were sealed with plastic sheets (see Figure 3.5.2), and a two-part epoxy adhesive (HIT-RE 500) was used to fill two third of the holes (see Figure 3.5.3). The CFRP rods were covered with a thin layer of the two-part epoxy adhesive (see Figure 3.5.4) and inserted into the holes (see Figure 3.5.5). Any excessive epoxy was removed. The plastic sheets at the lower ends of the holes were removed two days after installing the CFRP rods.

Figure 3.5.1: Hole cleaning using a wire brush

Figure 3.5.2: Lower hole end blocked with a plastic sheet

Figure 3.5.3: Filling a hole with epoxy

Figure 3.5.4: CFRP rod covered with a layer of epoxy

Figure 3.5.5: CFRP rods inserted into holes

It should be noted that Valerio et al (2009) demonstrated that it was possible to install CFRP rods by drilling vertical holes upwards from the soffit. The procedure explained above for installing CFRP rods was used for simplicity as it did not require drilling holes. However, drilled holes are expected to have rougher surfaces then cast-in-concrete holes, and this should improve the bond between the CFRP rods and the concrete.

3.5.2. *Installation of externally bonded CFRP sheets*

In order to install CFRP sheets, the humidity and curing environment should be checked in advance to achieve the best bond between the CFRP sheets and the concrete beam.

The round corners were ground to make them smoother in order to avoid stress concentrations and damage to the CFRP sheets (see Figure 3.5.6). Both sides of the web and the soffit, where the CFRP sheets were attached, were ground using a concrete grinder; this was followed by the use of a wire brush and air compressor to clean the dust and smooth any sharp aggregate particles (see Figure 3.5.7).

The two-part Tyfo S epoxy was then used to prime the CFRP sheets (see Figure 3.5.8). The rest of the epoxy was mixed with Cab-O-Sil to make it thicken and then primed onto the web and soffit of the test span. The primed CFRP sheets were attached to the primed area on the test span (see Figure 3.5.9).

A plastic trowel was used to remove any air bubbles underneath. A second layer of thickened epoxy was then applied to finish the installation procedure (see Figure 3.5.10).

Figure 3.5.6: Preparing the concrete surface for the EB CFRP sheet-strengthened specimens

Figure 3.5.7: Prepared concrete surface for EB CFRP sheet-strengthened specimens

Figure 3.5.8: Application of epoxy prime onto a shear span

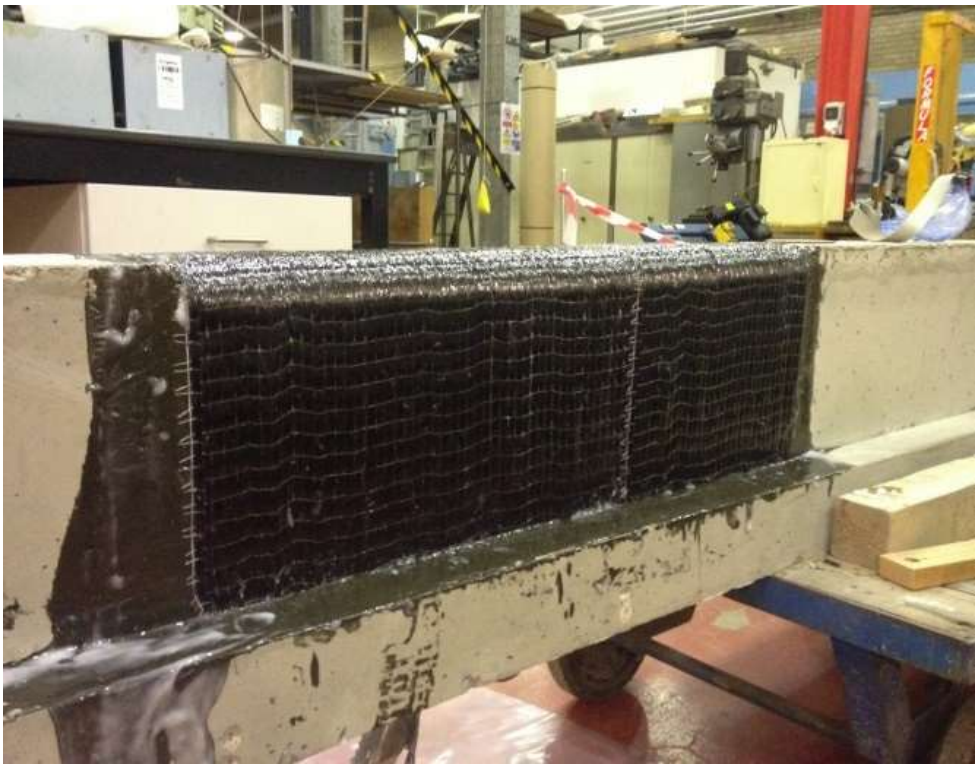

Figure 3.5.9: Application of epoxy-primed CFRP sheets onto a test span

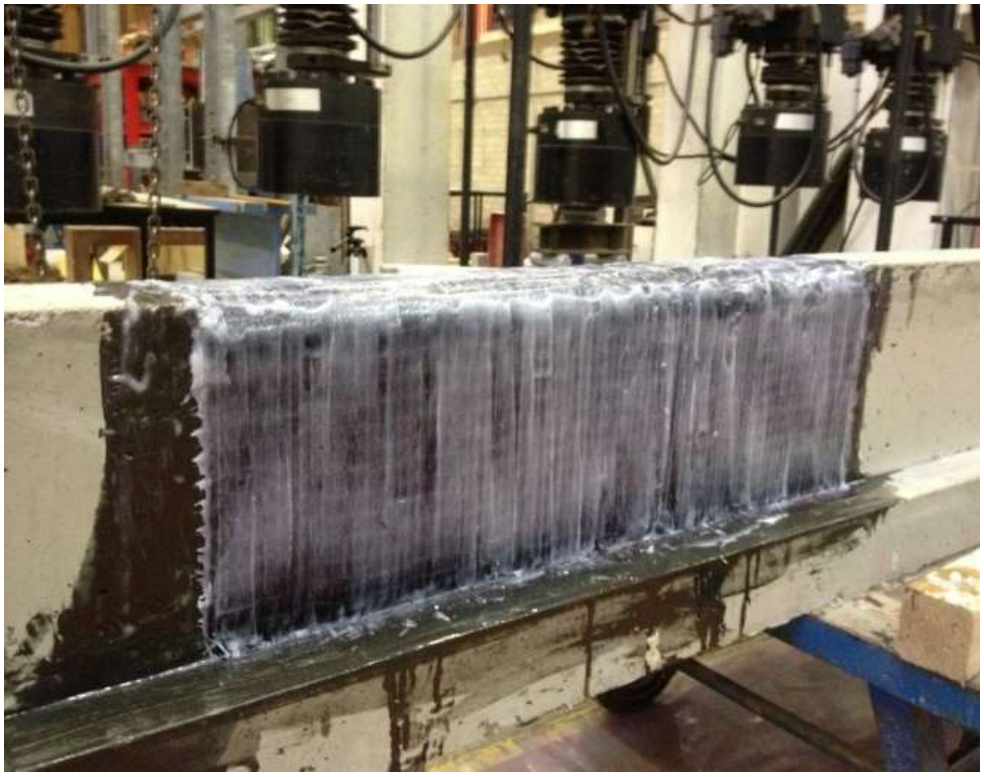

Figure 3.5.10: CFRP sheets coated with an additional epoxy layer

3.6. Test setup

The dimensions and reinforcement of the T-beams were designed in such a way that they would fail in shear under three-point bending.

All specimens were coated with a thin layer of matt white paint before conducting any tests, so that cracks could be easily traced. The un-strengthened and un-corroded specimen was tested straight after the curing period. The rest of the corroded specimens were subjected to the accelerated corrosion process after the curing period. The un-strengthened specimens were tested after the accelerated corrosion process, whereas the strengthened specimens were strengthened with CFRP composites before carrying out any tests.

The beam was simply supported. The centreline of each support was 250 *mm* from

the corresponding beam end. The centre-to-centre distance from the support to the loading jack was 900 *mm* at the test span and 1300 *mm* at the non-test span. Such an unbalanced arrangement will allow the beam to meet its capacity, with a hydraulic jack capacity of 400 *kN*. The specimens were checked by a level ruler to make sure the beam was horizontal.

The specimens were tested under a three-point-bending configuration. Steel plates, 200 *mm (width,* b_s*)* x 200 *mm (length,* l_s*)* x 25 *mm (thick,* t_s*)*, were used as bearing plates, whereas a 200 *mm (width,* b_l*)* x 200 *mm (length,* l_l*)* x 20 *mm (thick,* t_l*)* steel plate was used as a loading plate.

The load was applied at increments of 15 *kN* using a 400 *kN* hydraulic jack. The applied load can be read directly from the loading machine. Loading was continued up to failure of the test specimen. Details of the setup refer to Figure 3.6.1.

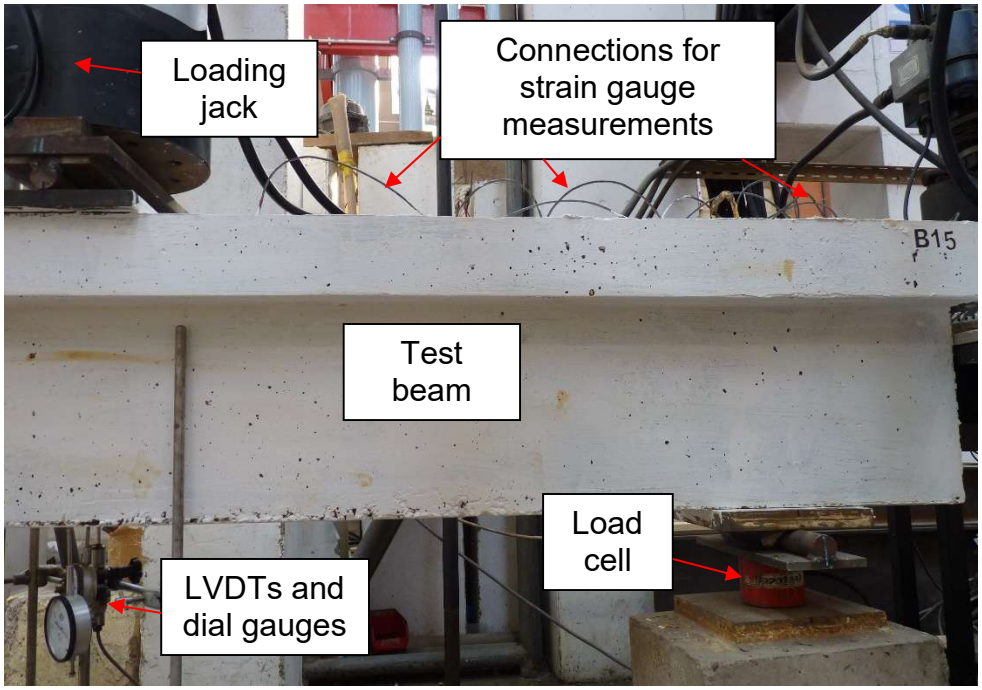

Figure 3.6.1: Typical test setup for the RC T-beams

3.7. Instrumentation

To meet the aim and the scope of this study, a comprehensive and carefully planned measuring strategy was implemented. A 250 *kN* load cell was placed under the support at the test span to measure the actual shear force, whereas the total load was monitored using the controller of the hydraulic jack. The vertical deflection under the applied load was measured using both linear variable differential transformers (LVDTs) and dial gauges. On the un-strengthened specimens, two LVDTs and one dial gauge were used to measure the deflection, whereas on the strengthened specimens, one LVDT and two dial gauges were used, as the data logger has limited connection ports. Thus, the limit of data logger ports means only one port is available when monitoring the deflection of the strengthened beams.

Strain gauges (6 *mm*, 120 *Ω*) were attached to each leg of the shear links in the test span and to the CFRP composites, as shown in Figure 3.7.1 to Figure 3.7.3. In addition, shear links in Beam B00, shear links and CFRP sheets in Beam S07, and shear links and CFRP rods in Beam B07 were instrumented with Fiber Bragg Grating (FBG) sensors at the same locations as the strain gauges.

The readings of the 250 *kN* load cell, LVDTs, and strain gauges were obtained using a data logger. The FBG sensor readings were recorded by a separate FBG analyser. The dial gauges and total applied load readings were manually recorded.

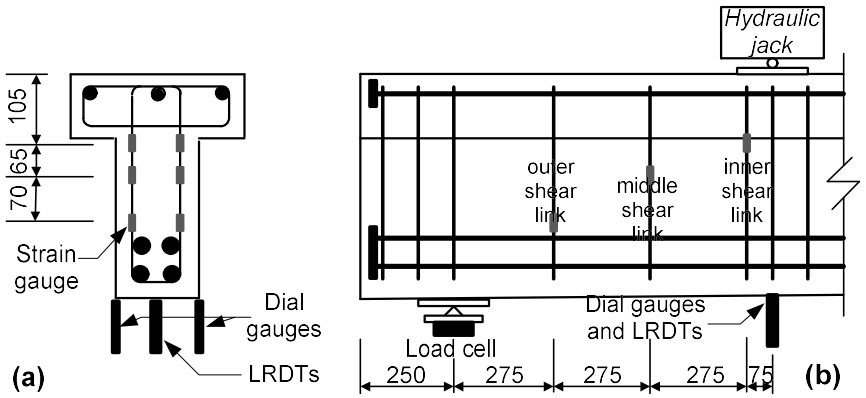

Figure 3.7.1: Measuring scheme for the un-strengthened specimens - (a) cross section, and (b) elevation

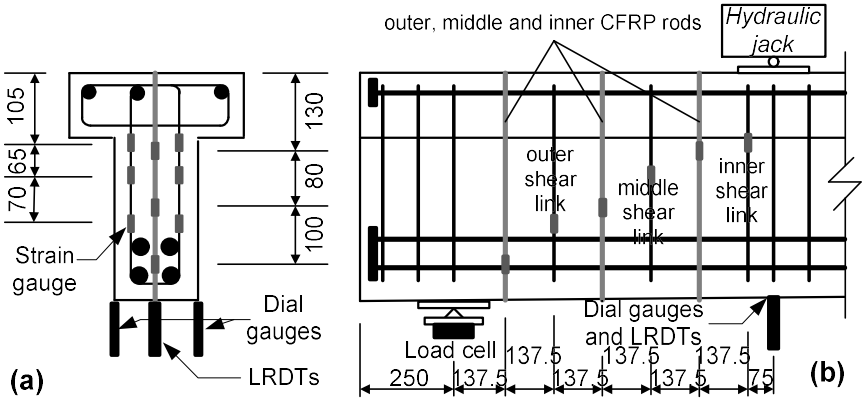

Figure 3.7.2: Measuring scheme for the CFRP rod-strengthened specimens - (a) cross section, and (b) elevation

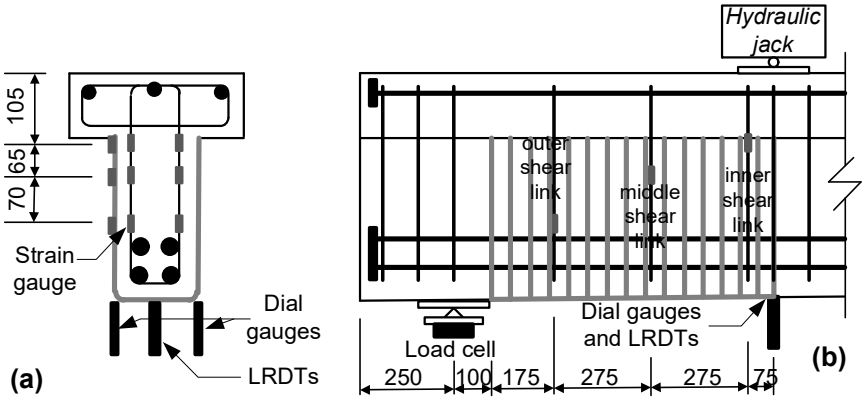

Figure 3.7.3: Measuring scheme for the CFRP sheet-strengthened specimens - (a) cross section, and (b) elevation

3.7.1. *Instrumentation of the steel reinforcement*

To install the strain gauges onto the shear links (Figure 3.7.4), these steps were followed:

1. A 200 *mm* flat file was used to prepare the surface of the 8 *mm* shear links, where the strain gauge would be attached, for a length of 20 *mm*.
2. Grade 120 sand paper was used to smooth the surface, followed by grade 200 sand paper to remove all the scratches on the targeted surface.
3. Acetone and cotton pads were used to clean the surface. The cotton pad was wetted in the acetone and then wiped over the targeted surface from top to bottom; the cotton pad was discarded once it had been used. Step 3 was repeated 4 – 6 times until the surface was clean.
4. The position of the strain gauge was marked using a permanent marker pen.
5. Clear tape was used to place the strain gauge onto the marked location.
6. The strain gauge was bonded to the targeted surface with superglue.
7. The superglue was left to dry for 48 *hrs*.
8. A soldering iron was used to connect the strain gauge to an isolated electric wire on the terminal pads.
9. A digital LCD multi-meter was used to check that the strain gauge was in a working condition after connection to the electrical wire.
10. The strain gauge was coated with two layers of silicon coating to prevent any damage.

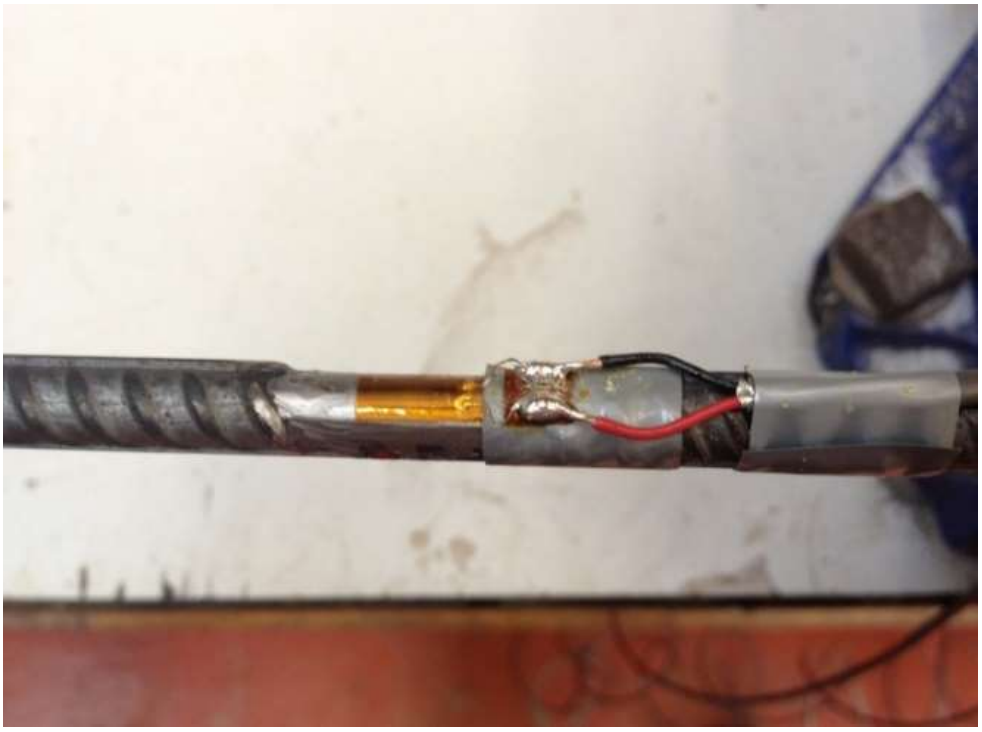

Figure 3.7.4: Test span shear link instrumented with a strain gauge

To install the FBG sensors onto the shear links, these steps were followed:

1. The opposite side of the strain gauge location was cleaned on the 8 *mm* shear link.
2. To avoid any damage to the silicon coating and the superglue bond, only water-wetted cotton was used to clean the targeted area. Step 2 was repeated until the targeted area was clean.
3. Cable ties were then used to secure the FBG sensors at the targeted locations. Extra care was taken not to damage the strain gauge wires; see Figure 3.7.5 for details.
4. HBM X120 visco-elastic two-component adhesive was used to glue the FBG sensor onto the targeted surface.
5. The adhesive was left to dry for 24 *hrs*.
6. The cable ties were then removed.

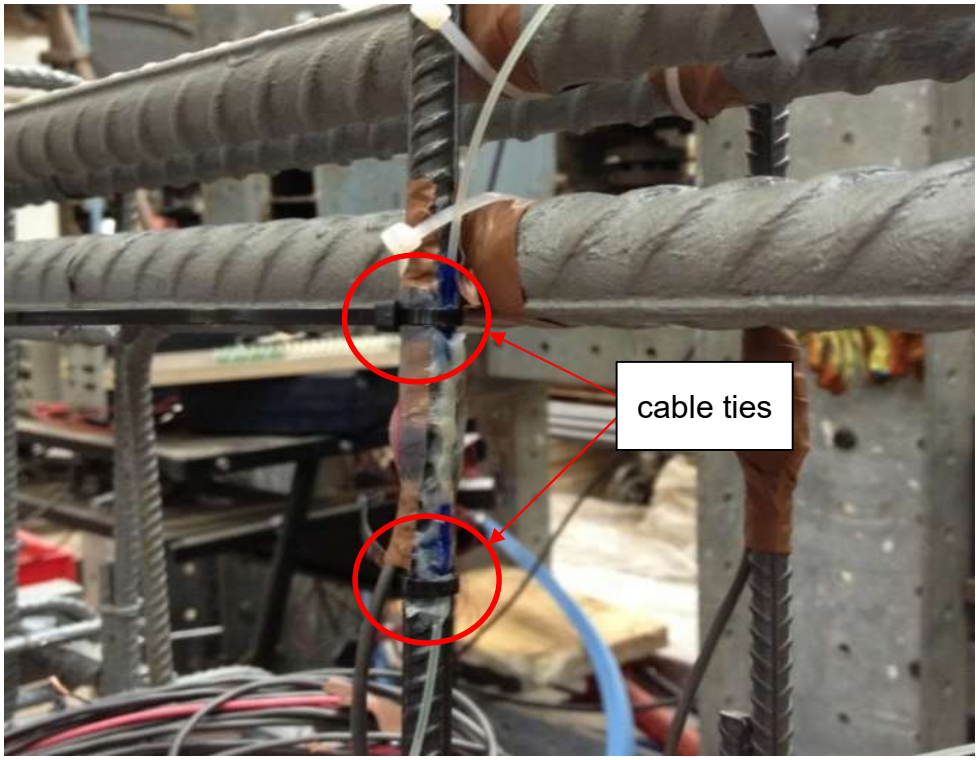

Figure 3.7.5: Test span shear link instrumented with FBG sensors

3.7.2. *Instrumentation of the CFRP composites*

Both the FBG sensors and strain gauges were attached to the selected CFRP composites. The strain gauges were used in all strengthened beams; the FBG sensors were used in selected beams.

The FBG sensors and strain gauges were installed before strengthening the beams for the DE CFRP rods. The installation procedures are similar to those described in Section 3.7.1. The targeted surface was prepared ahead of installing the sensors. Instead of using acetone to clean the targeted surface, clear water was used to clean the targeted surface as acetone will damage the epoxy. Once the sensors were installed, the rods were covered with two-part epoxy and placed onto the targeted locations of the RC T-beams. Details are shown in Figure 3.7.6 and Figure 3.7.7.

Figure 3.7.6: CFRP rod surface preparations

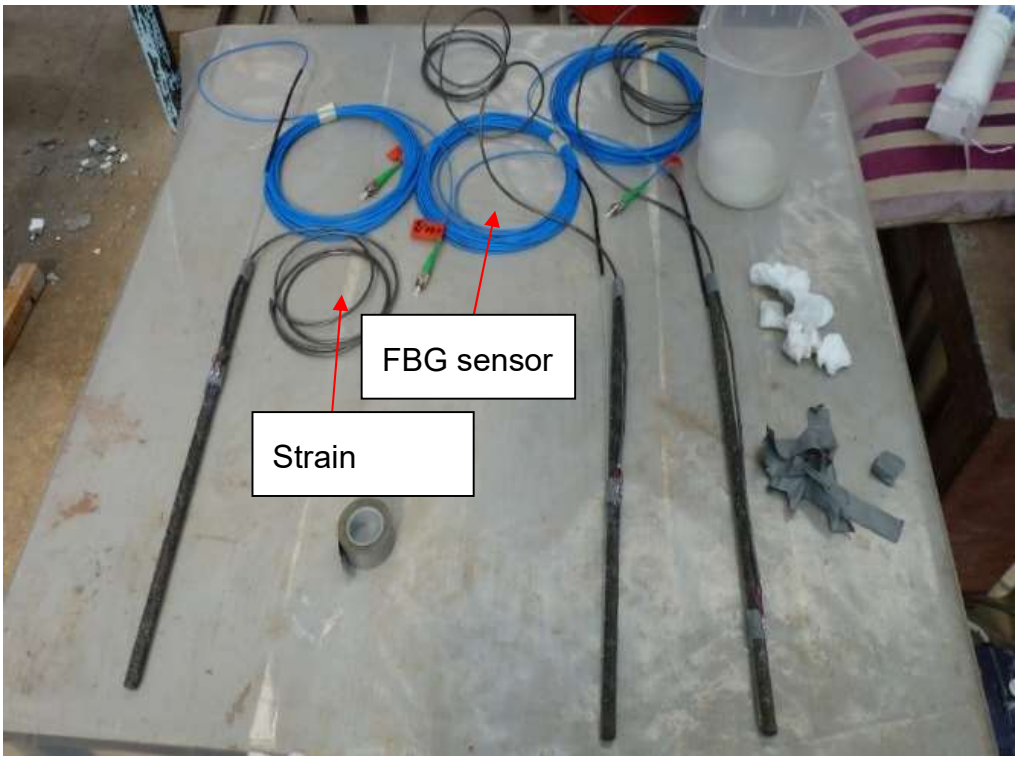

Figure 3.7.7: CFRP rods instrumented with strain gauges and FBG sensors

For the EB CFRP sheets, the FBG sensors and strain gauges were installed after the strengthening process but before load application. The installation procedures were similar to the instrument installation of steel reinforcement, as described in Section 3.7.1. However, acetone should not be used to clean the targeted location. Once the sensors were attached at the targeted location of CFRP sheets with superglue, the sensors were then covered with an additional layer of epoxy to prevent any damage (see Figure 3.7.8).

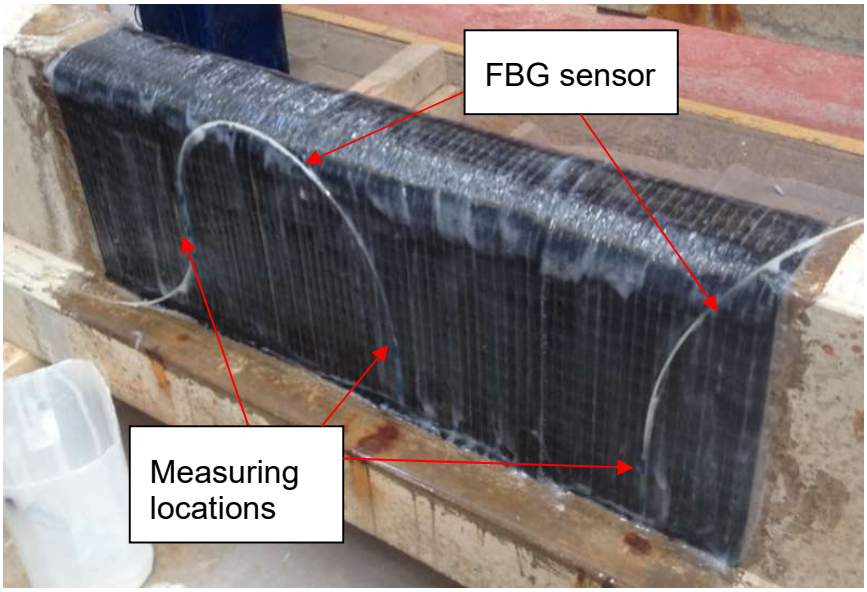

Figure 3.7.8: CFRP sheets instrumented with FBG sensors

3.7.3. *Deflection measurement*

Deflections were measured by one (un-strengthened specimens) or two (strengthened specimens) mechanical dial gauges, which were positioned at the bottom of the specimen along the centre line of the loading jack. Accompanying the mechanical dial gauges, two (un-strengthened specimens) or one (strengthened specimen) linear variable differential transformer (LVDTs) were also used to record the deflection of the specimens at the same location as the dial gauges, using a data

logger.

3.7.4. *Load measurement*

The total applied load was recorded manually from the hydraulic jack controller at an increment of 15 *kN*. The test span shear force was recorded by a data logger through a load cell located at the top of the test span support; see Figure 3.7.1 to Figure 3.7.3. The readings from the load cell were recorded simultaneously with the readings of the LVDTs, strain gauges and the supply voltage, every four seconds during the test.

3.8. Summary

An experimental programme to investigate the shear behaviour of corroded RC T-beams repaired with CFRP composites has been described in this chapter. The details of dimensions, materials, testing procedures and measurement schemes have been presented. A total of nine specimens were tested. Three corrosion levels (0%/uncorroded, 7% and 15%) and two strengthening schemes (deep embedment and externally bonded) were investigated. The specimens were tested under a three-point bending system. The shear span-to-effective depth ratio (a_v/d) was 3.05. The applied shear force at the test span, the deflection under the loading jack, the strains in the shear links and the CFRP composites were recorded using a data logger. The total applied load and the deflection under the loading jack were also recorded manually for comparison with the data logger readings. The strains in the shear links and CFRP composites were recorded by both strain gauges and FBG sensors in Beams B00, S07 and B07.

CHAPTER 4: EXPERIMENTAL RESULTS AND DISCUSSION

4.1. Introduction

The experimental results are presented in this chapter. This study focuses on exploring the behaviour of uncorroded and corroded RC T-beams repaired in shear with CFRP composites under monotonic loading. A total of nine RC T-beams were tested monotonically to failure. Six out of the nine specimens were subjected to an accelerated corrosion process, and the remaining three specimens were tested without being corroded.

Section 4.2 presents the experimental results of the corroded reinforcement. The accuracy of the predicted corrosion level using Faraday's law is reviewed, together with the change in mechanical properties due to corrosion attack. The shear force capacity, load-deflection results, cracking and failure modes, strain in the steel shear links and strain in the CFRP systems are discussed in Sections 4.3, 4.4, 4.5, 4.6 and 4.7 respectively. As the concrete strength was different in each beam, the normalized shear stress method was used to investigate the shear behaviour of the corroded RC T-beams repaired with DE or EB CFRP systems. The strain measurement performance of Fibre Bragg grating and strain gauge sensors is summarised in Section 4.8. The effect of corrosion levels and shear strengthening systems on the shear resistance components is presented in Sections 4.9 and 4.10 respectively. Finally, Section 4.11 summarises the key findings of the experimental results.

4.2. Results of the accelerated corrosion process

In this section, the results of the corroded shear links are presented. Six beams were subjected to the accelerated corrosion process, each beam containing three closed shear links located in the flange and web at a spacing of 275 *mm* at the test span. The physical properties were tested from both corroded shear links at the flange and web. Table 4.2.1 and Table 4.2.2 show the summary of the physical results of the corroded shear links at 7% and 15% corrosion levels respectively.

As can be seen in Table 4.2.1 and Table 4.2.2, the shear links in the test spans of beams N07, B07, S07, N15, B15, and S15 had average actual corrosion levels of 6.4%, 7.6%, 6.0%, 12.2%, 12.3%, and 12.1% respectively. Except for the shear links in the test span of beam B07, all the corroded shear links had average actual corrosion levels that are less than the targeted corrosion levels of either 7% or 15%. The average differences between the targeted (based on Faraday's law) and actual (based on gravimetric mass loss) corrosion levels were 11% and 23% for the shear links with nominal corrosion levels of 7% and 15% respectively. Comparable results were reported by Malumbela et al. (2012), where Faraday's law generally underestimated the actual corrosion level introduced by the Galvanostatic method. El Maaddawy and Soudki (2003) suggested that, at corrosion levels higher than 7%, the amount of corrosion around the steel reinforcement might hinder the diffusion of the Hydroxide and/or Ferrous ions through the rust layer. This might explain the higher difference between the targeted and actual corrosion levels for the shear links with a nominal corrosion level of 15%.

Table 4.2.1: Corrosion results at 7% corrosion level

Shear link reference	Original mass, $M_{o,g}$ (*g*)	Corrosion time (days)	Applied current (*mA*)	Remaining mass, $M_{r,g}$ (*g*)	Theoretical corrosion level (%)	Actual corrosion level (%)	Average actual corrosion level (%)
N07/outer	687.7	23	89.6 (200 $\mu A/cm^2$)	640.9	7.0	6.8	6.4
N07/middle	687.3		89.6 (200 $\mu A/cm^2$)	646.3	7.0	6.0	
N07/inner	683.2		89.2 (200 $\mu A/cm^2$)	639.8	7.0	6.4	
B07/outer	684.0	23	89.4 (200 $\mu A/cm^2$)	633.8	7.0	7.3	7.6
B07/middle	692.9		90.5 (200 $\mu A/cm^2$)	641.8	7.0	7.4	
B07/inner	687.9		89.9 (200 $\mu A/cm^2$)	633.1	7.0	8.0	
S07/outer	685.5	23	89.3 (200 $\mu A/cm^2$)	640.0	7.0	6.6	6.0
S07/middle	690.2		89.8 (200 $\mu A/cm^2$)	650.5	7.0	5.8	
S07/inner	690.5		90.0 (200 $\mu A/cm^2$)	652.2	7.0	5.6	

Table 4.2.2: Corrosion results at 15% corrosion level

Shear link reference	Original mass, $M_{o,g}$ (*g*)	Corrosion time (days)	Applied current (*mA*)	Remaining mass, $M_{r,g}$ (*g*)	Theoretical corrosion level (%)	Actual corrosion level (%)	Average actual corrosion level (%)
N15/outer	689.7	53	83.3 (185 $\mu A/cm^2$)	609.1	15.0	11.7	12.2
N15/middle	688.8		83.3 (185 $\mu A/cm^2$)	610.9	15.0	11.3	
N15/inner	699.6		83.3 (185 $\mu A/cm^2$)	604.9	15.0	13.5	
B15/outer	687.5	1270	188.9 (140 $\mu A/cm^2$) (connected in series)	612.1	15.0	11.0	.3
B15/middle	699.3			613.7	15.0	12.2	
B15/inner	692.4			598.4	15.0	13.6	
S15/outer	699.1	49	91.2 (200 $\mu A/cm^2$)	615.2	15.0	12.0	12.2
S15/middle	686.4		89.3 (200 $\mu A/cm^2$)	613.5	15.0	10.6	
S15/inner	687.2		89.5 (200 $\mu A/cm^2$)	592.1	15.0	13.8	

Table 4.2.2 shows that the current density values and wiring methods used in this study had an insignificant effect on the average actual corrosion level. The shear links in the test spans of B15, N15, and S15 were corroded using current density values of 140 $\mu A/cm^2$, 185 $\mu A/cm^2$, and 200 $\mu A/cm^2$ respectively. However, the shear links in the three beams had approximately equal average actual corrosion levels ranging from 12.1% to 12.3%. The three readings were so close that the standard deviation will probably tend to zero.

4.3. Shear capacity of concrete beam

Both EB and DE strengthening techniques were investigated in this research. It should be noted that the tensile strength of 10 *mm* DE CFRP rods (2172 N/mm^2) is higher than the tensile strength of 1 *mm* thick EB CFRP sheets (986 N/mm^2). Therefore, each 10 *mm* DE CFRP rod is equivalent to a 157 *mm* long and 1 *mm* thick EB CFRP sheet to resist same tensile load along the fibre orientation. In terms of the cost, the 10 *mm* DE CFRP rods and 1 *mm* thick EB CFRP sheets are $7.19 and $14.52 to $16.13 per square meter respectively. However, installing EB CFRP sheets requires access to the side and soffit of the bridge, which is limited in some circumstances; hence, wrapping the structure is not possible. Valerio et al. (2009) demonstrated that it was possible to install FRP rods by drilling vertical holes upwards from the soffit for the bridges which needed to have strengthening work carried out. However, drilling vertical holes may lead to the failure of the existing structure.

Table 4.3.1 shows the total shear force attained by each beam at failure. As reported

in Table 4.3.1, the tested beams had variable cube compressive strengths, and therefore it would be inaccurate to directly compare their shear force capacities. In order to reasonably compare the shear strength of the tested beams, the nominal shear stress at failure ($V_{max}/b_w d$) for each beam was divided by the square root of its cube compressive strength, which is a measure of concrete shear strength, where 'V_{max}' is the shear capacity, 'b_w' is the width of web and 'd' is the effective depth. The square root of concrete compressive strength, f_{cu}, is normally used to represent the shear strength, such as BS 5400: Part 4 (or BD 44/95) and ACI 318-08. The resulting values of normalized shear stress at failure ($V_{max}/b_w d\sqrt{f_{cu}}$) were then divided by the corresponding value for N00 (i.e. 0.76), to calculate the normalized shear stress at failure relative to N00 (see Table 4.3.1). The author acknowledges that the material variation was large in the concrete cube compressive strength. The concrete cube compressive strength of beams with and without 3% calcium chloride was 24±10% *MPa* and 38±10% *MPa* respectively. By applying the nominalisation method, the effect due to concrete cube compressive strength should be limited.

The effect of shear link corrosion level on the shear strength of the unstrengthened beams can be inferred by comparing their normalized shear stresses at failure relative to N00. Increasing the shear link corrosion level decreased the shear strength of N07 and N15 relative to that of N00 by 11% and 14% respectively. As the corrosion level increases, the yield and ultimate stresses and strains of the shear links decrease (Almusallam, 2001), and the bond performance between the shear links and concrete deteriorates. This, in turn, reduces the steel contribution to the shear force capacity, which adversely affects the shear strength of the beams.

Table 4.3.1: Shear force capacity results

Beam designation	Average cube compressive strength (N/mm^2)	Total shear force (kN)	Normalized shear stress at failure	Normalized shear stress at failure relative to N00	Deflection at loading point (mm)	Failure mode
N00	26.3	143	0.76	1.00	7.39	Shear
N07	35.1	148	0.68	0.89	8.73	Shear
N15	41.8	155	0.65	0.86	9.29	Shear
B00	21.7	142	0.83	1.09	9.57	Shear
B07	37.0	182	0.81	1.07	10.54	Shear
B15	37.0	164	0.73	0.96	9.69	Shear
S00	37.0	182	0.81	1.07	9.02	Shear
S07	36.8	174	0.78	1.03	7.62	Shear
S15	42.9	174	0.72	0.95	9.24	Shear

The shear link nominal corrosion level of 7% did not have a significant effect on the shear strength of the strengthened beams. The difference between the normalized shear stresses at failure for B00 and B07 was about 2%. Similarly, S00 and S07 had a difference of about 4% between their normalized shear stresses at failure. At the actual corrosion level of 12% (proposed corrosion level of 15%), the strengthened beams (i.e. B15 and S15) had normalized shear stresses at failure that were approximately 12% less than the corresponding values for the un-corroded beams (i.e. B00 and S00).

As can be seen in Table 4.3.1, all strengthened beams had higher normalized shear stresses at failure than the corresponding unstrengthened beams. Of note is that B07 and B15 had normalized shear stresses at failure that were 19% and 12% higher than the corresponding values for N07 and N15 respectively, whereas the

corresponding percentage enhancements for S07 and S15 were 15% and 11% respectively. The DE technique therefore seems more effective than the EB technique in enhancing the shear strength of RC beams with corroded shear links. The higher effectiveness provided by the DE technique may be explained by two factors. First, the embedded CFRP rods are less susceptible to debonding issues due to better bond performance between the concrete core and the CFRP reinforcement (Chaallal et al., 2011). Secondly, the CFRP rods can be embedded along the full effective depth of the beam, whereas the presence of the flange limits the effective depth of the EB CFRP sheets.

The effectiveness of both strengthening systems decreased with increasing shear link corrosion level. At the lower shear link corrosion level, the strengthening systems enhanced the normalized shear stresses at failure for B07 and S07, by 7% and 3% respectively, relative to that of N00 (i.e. the un-corroded unstrengthened beam). However, at the higher shear link corrosion level, B15 and S15 had normalized shear stresses at failure that were 4% and 5% lower respectively than the corresponding value for N00. Hence, the strengthening systems were almost, but not quite, effective at returning B15 and S15 to their un-corroded shear strength. The reduced effectiveness of the EB technique, with increasing shear link corrosion levels, may be explained by the reduced friction resistance at the shear link-to-concrete interface. This causes early separation of the lateral concrete cover after the formation of inclined cracks (El-Maaddawy and Chekfeh, 2013), where the DE CFRP rod relied on core concrete and benefits from confinement. This applies generally. Further research is required to identify the factors affecting the reduced effectiveness of the

DE technique with increasing shear link corrosion levels.

4.4. Load deflection results

Figure 4.4.1 to Figure 4.4.3 show the normalized shear stress-deflection curves for the un-corroded, 7% corroded, and 15% corroded beams. Similar to shear force capacity results, comparing the shear force–deflection curves directly was deemed unreasonable due to the difference in the concrete compressive strength. Therefore, the normalized shear stress ($V_{max}/b_w d\sqrt{f_{cu}}$)-deflection curves were used for comparison purposes. The square root of concrete compressive strength is normally used to represent the shear strength, such as BS 5400: Part 4 (or BD 44/95) and ACI 318-08. All beams featured a quasi-linear deflection response up to peak shear stress. The sudden drop in load at peak shear stress was a characteristic of brittle (shear) failure. The load deflection curve of N00 showed snap back at failure load; this was due to unloading of the specimens for safety considerations.

For each beam, the normalized shear stress at failure and the corresponding deflection at loading point are given in Table 4.3.1. Except in the case of the un-corroded beams (Figure 4.4.1), the unstrengthened and DE strengthened beams had comparable stiffness at a given corrosion level, whereas the EB beams had a stiffer response. This trend is particularly evident in Figure 4.4.2 and Figure 4.4.3. Mofidi and Chaallal (2011) suggested that some EB CFRP continuous sheets, although uniaxial, can still carry some load in the direction perpendicular to the fibreorientation. This might explain the higher stiffness of the EB beams compared with those of the unstrengthened and DE strengthened beams.

Figure 4.4.4 to Figure 4.4.6 show the normalized shear stress-deflection curves for un-strengthened, DE strengthened, and EB strengthened beams respectively. For un-strengthened beams (Figure 4.4.4), stiffness decreased with the increase in corrosion levels. As the corrosion level increases, the cross-sectional area decreases, and consequently the stiffness of a shear link decreases. This leads to increased crack widths, which result in higher deflections and consequently lower beam stiffness.

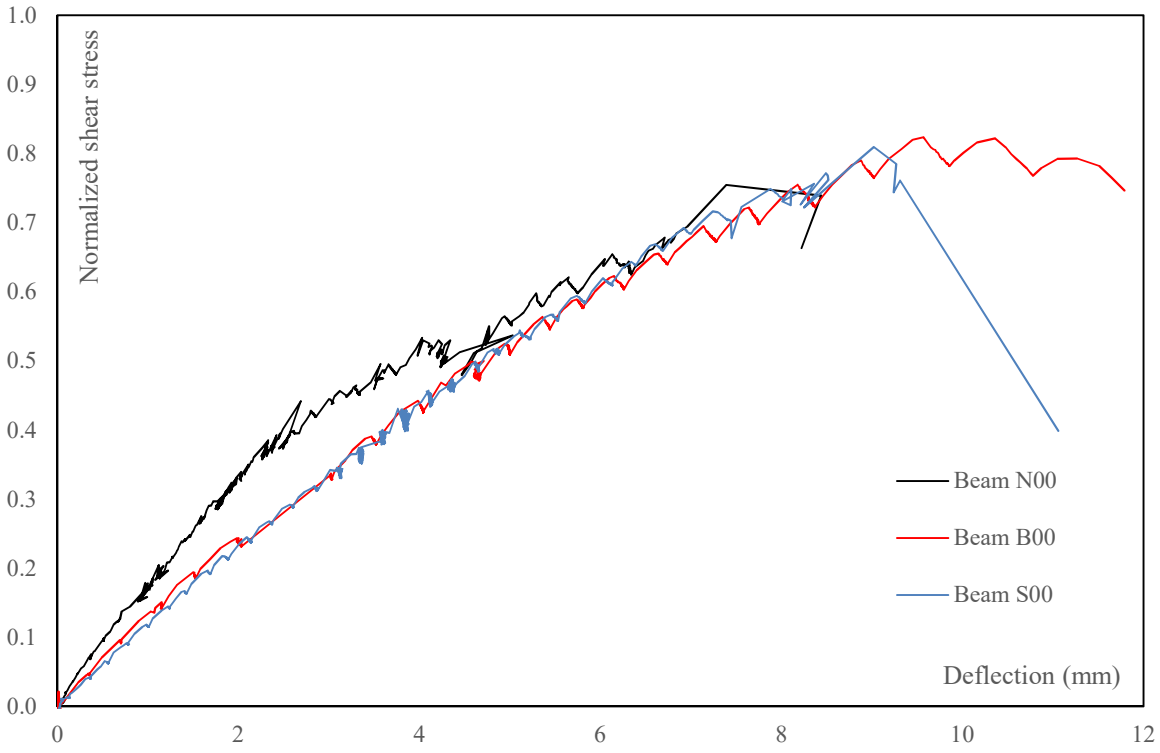

Figure 4.4.1: Normalized shear stress-deflection curves for beams with different strengthening methods at 0% corrosion level

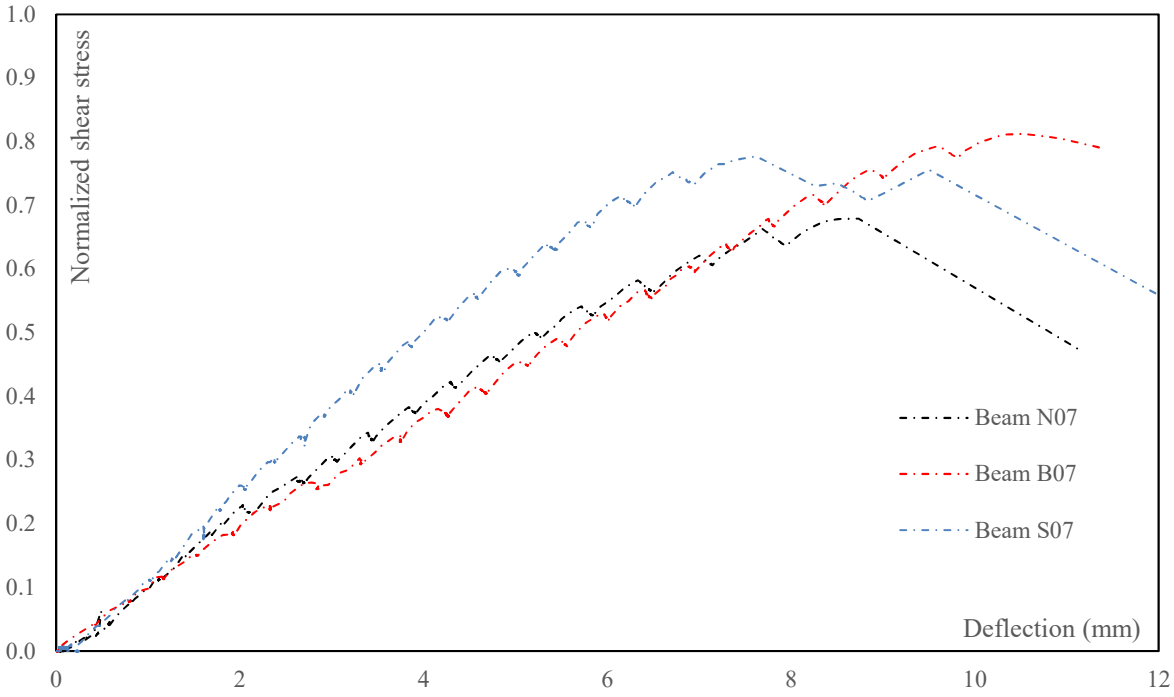

Figure 4.4.2: Normalized shear stress-deflection curves for beams with different strengthening methods at 7% corrosion level

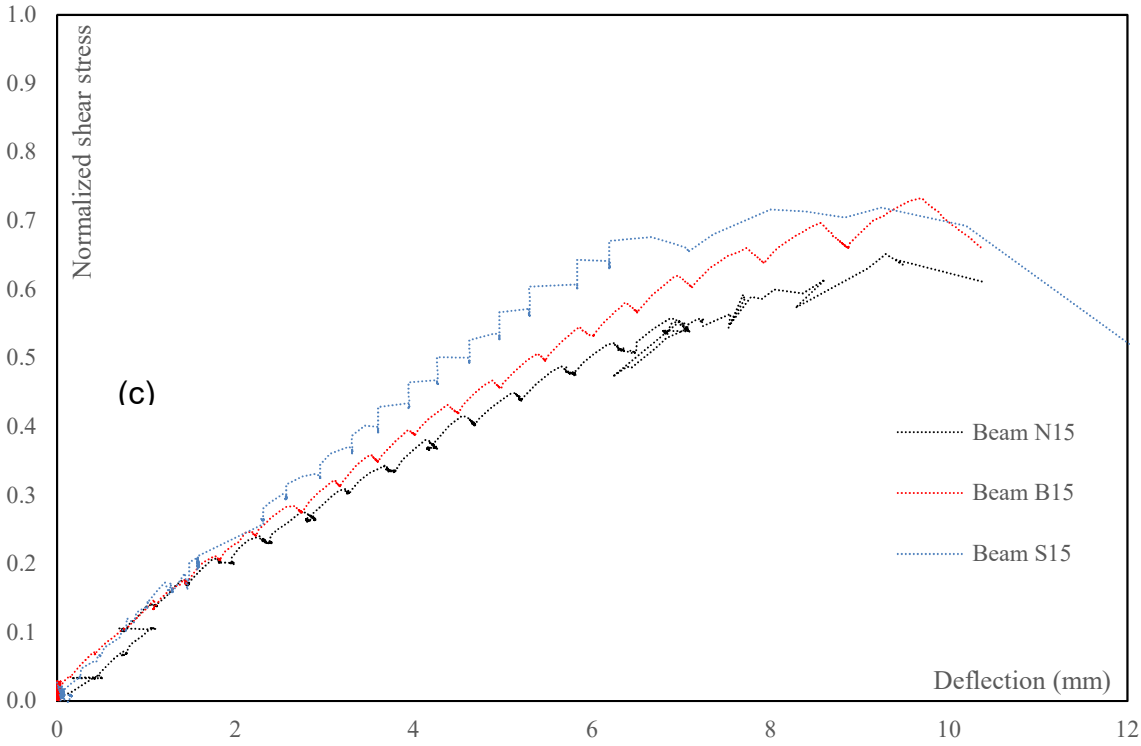

Figure 4.4.3: Normalized shear stress-deflection curves for beams with different strengthening methods at 12% corrosion level

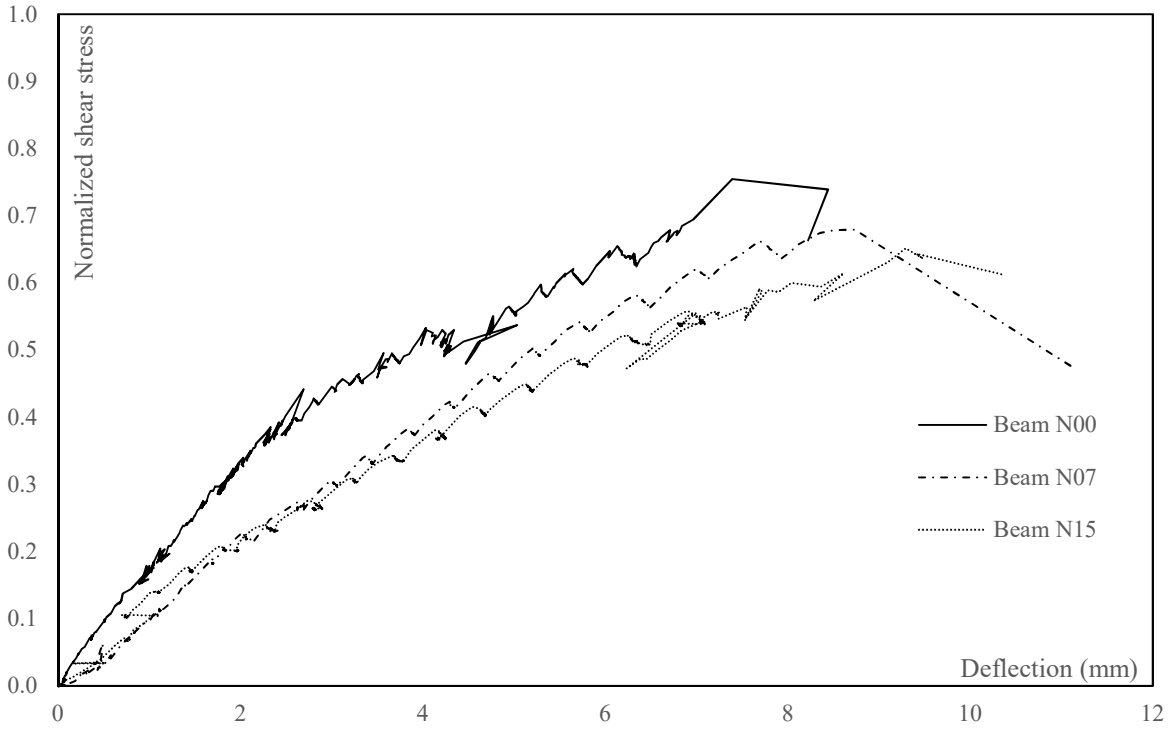

Figure 4.4.4: Normalized shear stress-deflection curves for unstrengthened beams with different corrosion levels

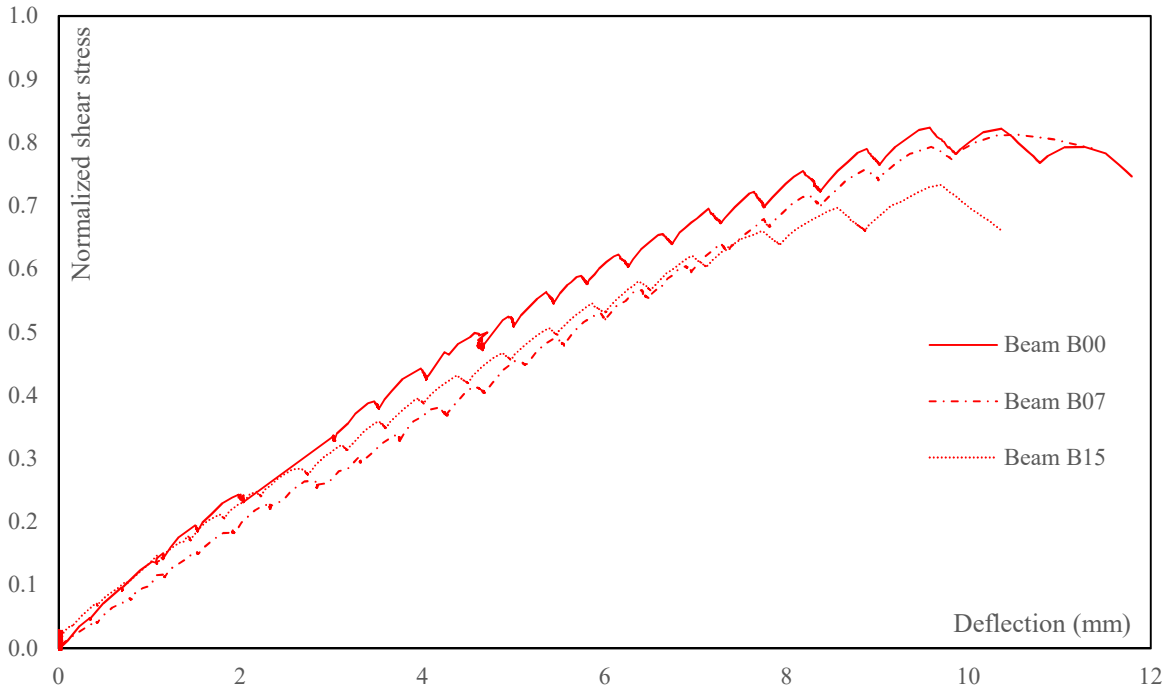

Figure 4.4.5: Normalized shear stress–deflection curves for DE CFRP rod strengthened beams with different corrosion levels

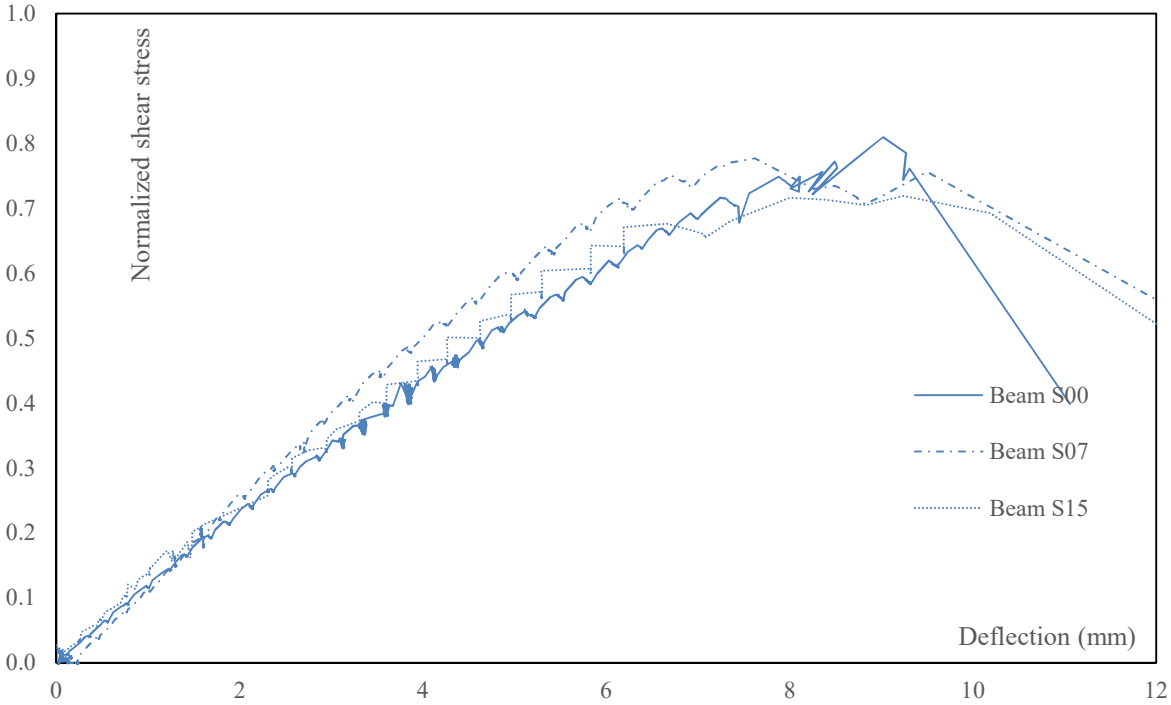

Figure 4.4.6: Normalized shear stress–deflection curves for EB CFRP sheet strengthened beams with different corrosion levels

The stiffness of the DE and EB strengthened beams was less affected by corrosion level. This may be attributable to the higher axial rigidity ratio (see Equation 4.2) in the beams.

$$k = \frac{E_s A_s}{b_w s} + \frac{E_f A_f}{b_w s_f} \qquad (4.2)$$

where:

k Axial rigidity ratio (*N/mm²*).

E_s Elastic modulus of shear links (*N/mm²*).

A_s Cross-sectional area of shear links (*mm²*).

b_w Width of concrete web section (*mm*).

s Spacing of shear links (*mm*).

E_f Elastic modulus of FRP (*N/mm²*).

A_s Cross-sectional area of FRP (*mm²*).

s_f Spacing of FRP (*mm*).

The incorporation of the FRP reinforcement seems to mitigate the effect of shear link corrosion on beam stiffness. Comparable results were reported by El-Maaddawy and Chekfeh (2013), where El-Maaddawy and Chekfeh (2013) tested unstrengthened T-beams with corrosion levels of 0% and 15%, and EB strengthened T-beams with a corrosion level of 15%. The shear span–to–effective depth ratio is 3.00 and the shear span length is 600 *mm*. The uncorroded and unstrengthened T-beam was the stiffest beam, while the stiffness of a 15% corroded and EB strengthened T-beam was higher than the stiffness of a 15% corroded and unstrengthened T-beam.

4.5. Cracking and failure mode

It should be noted that only the cracks on the test span were compared. The non-test span was considered as having less effect on the failure mode of the beams because the beams were simply supported. The failure modes of the unstrengthened beams are shown in Figure 4.5.1. All the unstrengthened beams, regardless of the shear link corrosion level, exhibited a shear mode of failure due to inclined cracks that ran from the support to the load point. In the web, the main inclined cracks followed a path at an angle of approximately 32°, intersecting both the outer and middle shear links. The inclined cracks followed a much shallower path (approximately 20°) in the flange, intersecting the inner shear link just below the top of the flange. Visual inspection of Beam N15 at failure (see Figure 4.5.1) revealed that it had a wider main inclined

crack compared with the corresponding cracks in Beams N00 and N07. This was to be expected, as the shear links with the 12.2% average corrosion level offered less resistance to crack opening.

Figure 4.5.2 shows the failure modes of the beams strengthened with the DE technique. Similar to the unstrengthened beams, B00, B07, and B15 failed in shear due to inclined cracks that extended from the support to the load point. However, the inclined cracks in the beams with embedded CFRP reinforcement were more distributed than the corresponding cracks in the unstrengthened beams. It is well known that increasing the transverse reinforcement ratio in an RC beam results in more distributed and narrower cracks (Zakaria et al., 2009) for shear failure beams. The crack patterns of B00, B07, and B15 can therefore be attributed to the presence of the embedded CFRP rods. Of note is that there was no sign of debonding between the embedded CFRP rods and the surrounding concrete at failure.

Figure 4.5.3 shows the typical failure mode of beams strengthened with EB CFRP sheets; all the EB strengthened beams failed due to debonding of the CFRP sheet, which is very similar. Hence, a typical drawing is provided. The beams failed due to inclined cracks that penetrated the flange and propagated towards the load point. The crack propagation was accompanied by debonding of the EB CFRP sheets, as shown in Figure 4.5.3. The premature debonding of the EB CFRP sheets may be prevented by anchoring the strengthening system to the concrete using compatible composite anchors. This would increase the effectiveness of the EB CFRP sheets, and consequently, the shear force carrying capacity of the beams (Eshwar et al. 2008; Mofidi et al. 2012b; Koutas and Triantafillou 2013). Figure 4.5.4 shows the

typical failure crack of concrete once the EB CFRP sheets were removed.

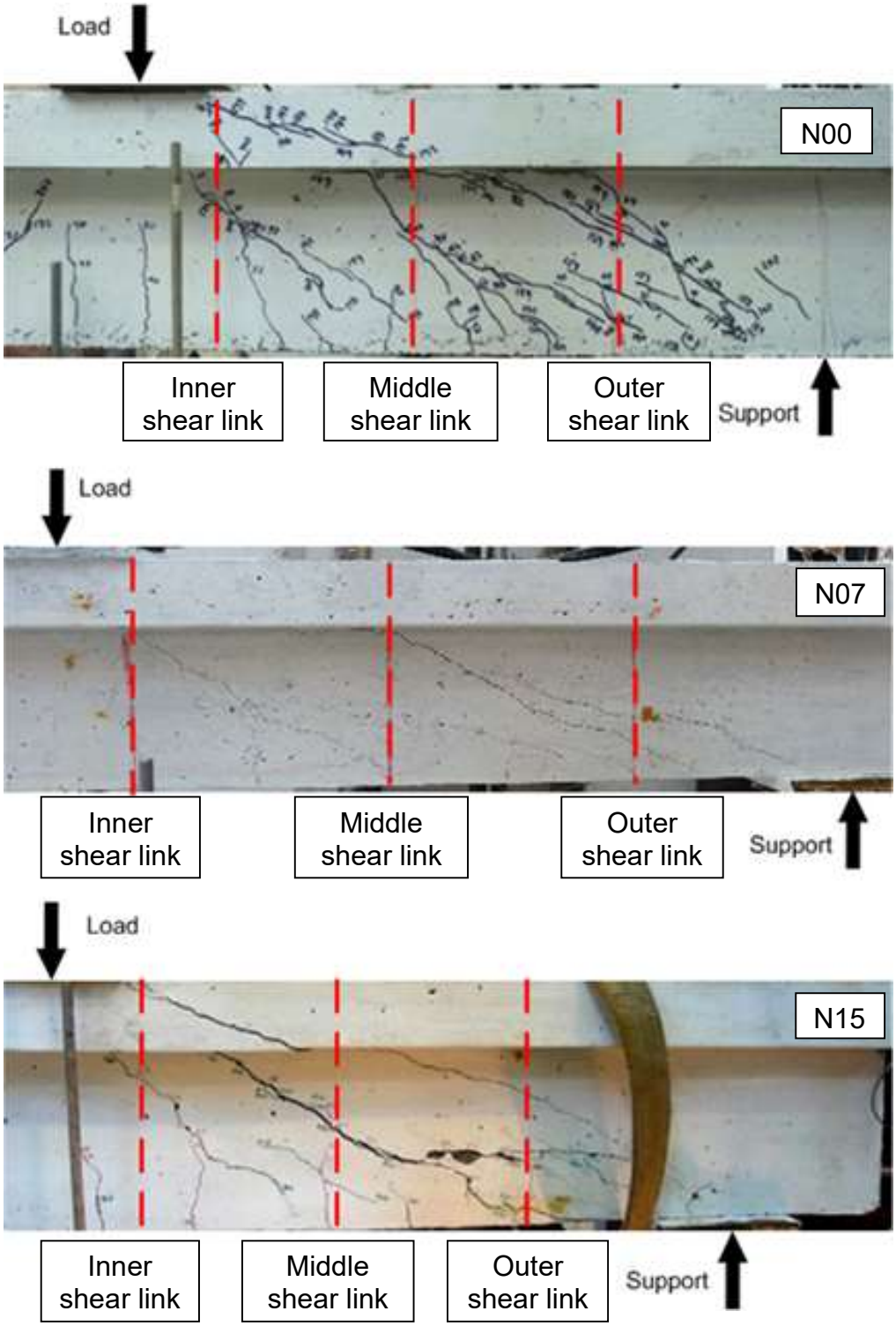

Figure 4.5.1: Unstrengthened beams at failure

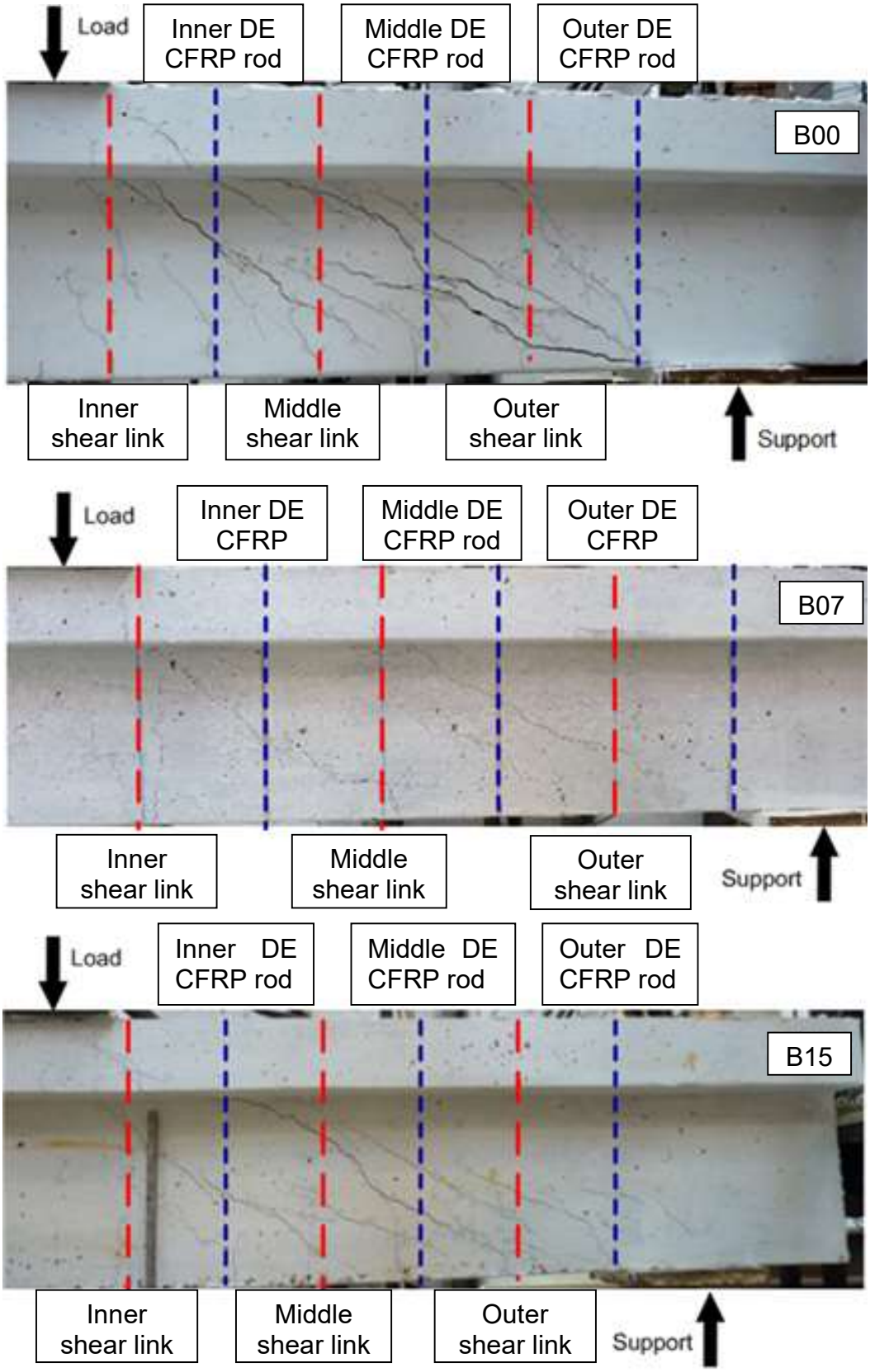

Figure 4.5.2: DE CFRP rod strengthened beams at failure

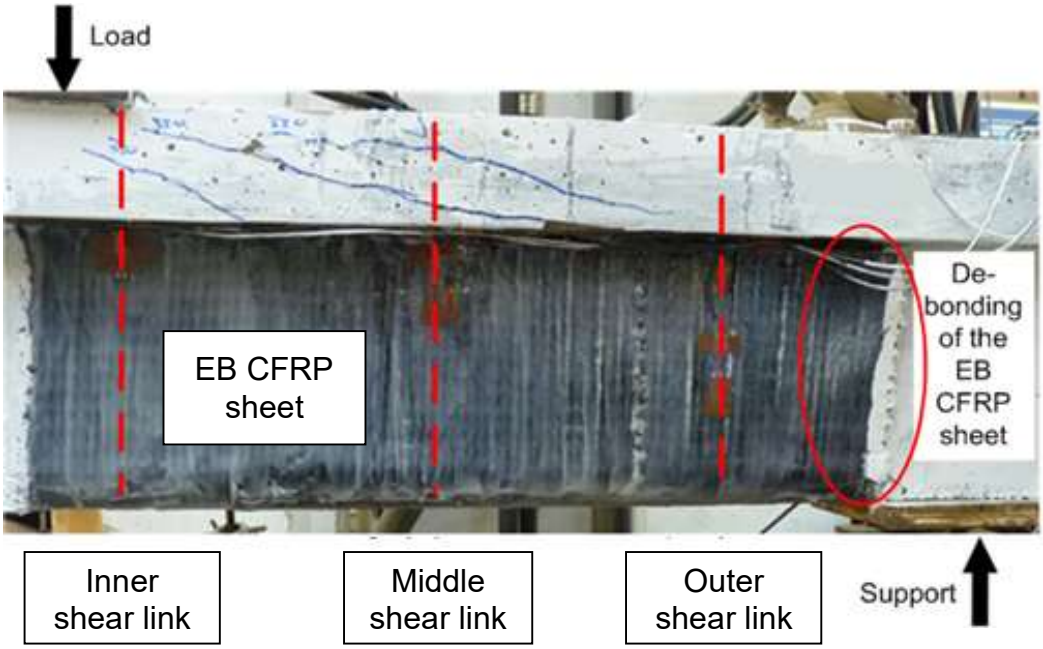

Figure 4.5.3: Typical failure mode of the EB CFRP sheet strengthened beams

Figure 4.5.4: Typical cracks after removing the EB CFRP sheets

4.6. Strain in the steel shear links

This section reports on strain in the steel shear links recorded by the strain gauges. Figure 3.2.1 shows the locations of the strain gauges attached to the test span shear links. For the purpose of interpreting results, the shear links were categorized into outer, middle, and inner shear reinforcement (see Figure 3.2.1). Similarly, the strain

gauges attached to the DE CFRP rods and EB CFRP sheets were categorized into outer, middle, and inner gauges, as shown in Figure 3.2.1. Unfortunately, some strain gauges failed during testing and hence their results were discarded.

Figure 4.6.1 to Figure 4.6.3 shows the normalized shear stress-strain variations for the steel shear links. It should be noted that the backwards movement of some figures was due to unload when the beam failed. In general, the shear links exhibited two stages of response during loading. In the first stage, the shear links were inactive and therefore did not contribute to a significant shear resistance. The second stage is marked by the formation of inclined cracks at a normalized shear stress of approximately 0.2 to 0.3, except for B00 (crack recorded a normalized shear-stress of about 0.05). After the formation of inclined cracks, the shear links developed strain with increasing load until failure occurred.

The outer and middle shear links were more strained when compared with the inner shear links. This can be explained by the fact that the outer and middle shear links were intersected by the main shear cracks. The inner shear links were located at a region which did not experience much cracking.

At a given shear link location (i.e. outer, middle, or inner), a shear link in a beam strengthened with EB CFRP sheets (i.e. S00, S07, or S15) had less strain at a given normalized shear stress than the corresponding shear link in a beam strengthened with DE CFRP rods (i.e. B00, B07, or B15). For example, between a normalized shear stress of 0.3 and 0.55, the strain in the middle shear link in S15 varied between 0.0001 and 0.0010, whereas the strain in the middle shear link in B15 varied between 0.0003 and 0.0020. This result was influenced by two factors. Firstly, the EB CFRP

sheets had higher axial rigidity per unit area (1533 *MPa*) than the DE CFRP rods (283 *MPa* per rod). Secondly, the EB CFRP sheets were continuous, whereas the DE CFRP rods were located between the shear links (see Figure 3.2.1) and therefore could not reduce the strain in the shear links in a similar way to the EB CFRP sheets.

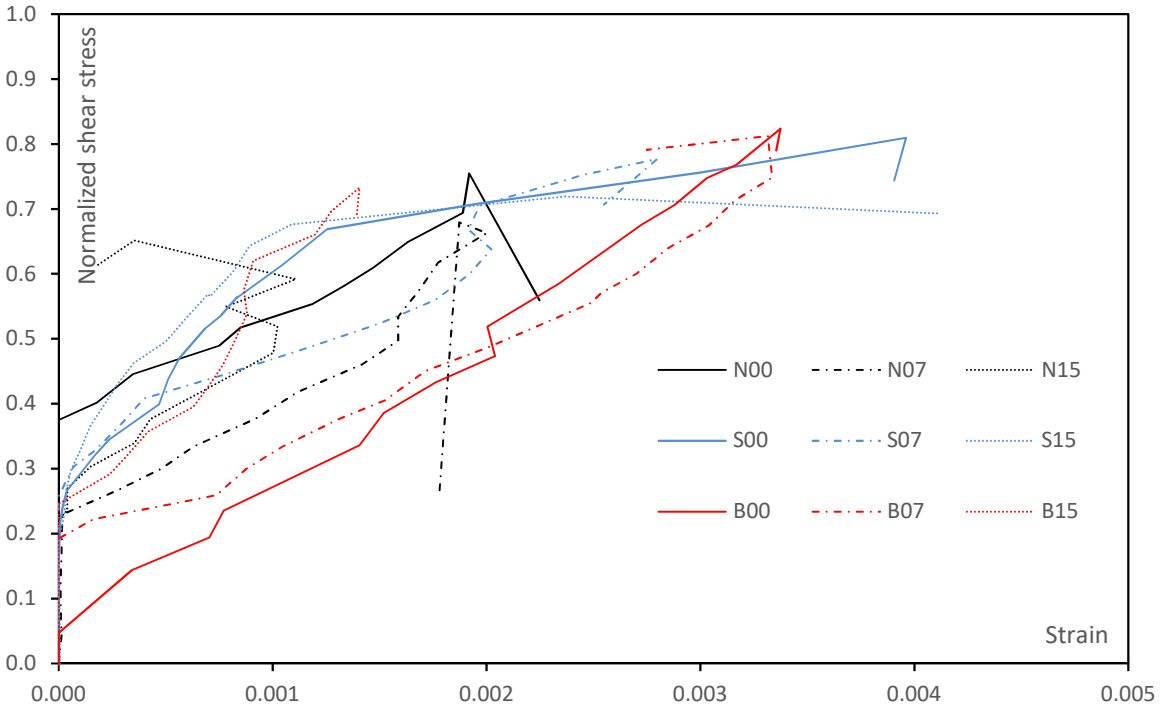

Figure 4.6.1: Normalized shear stress-strain curves for outer shear links

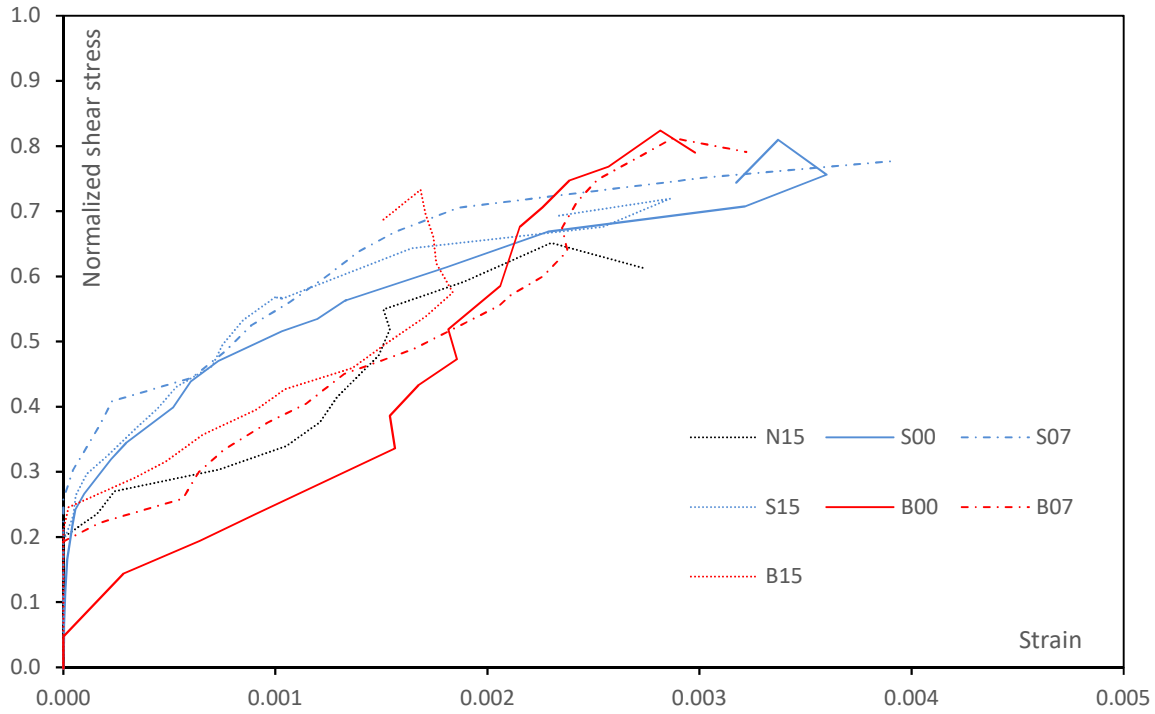

Figure 4.6.2: Normalized shear stress-strain curves for middle shear links

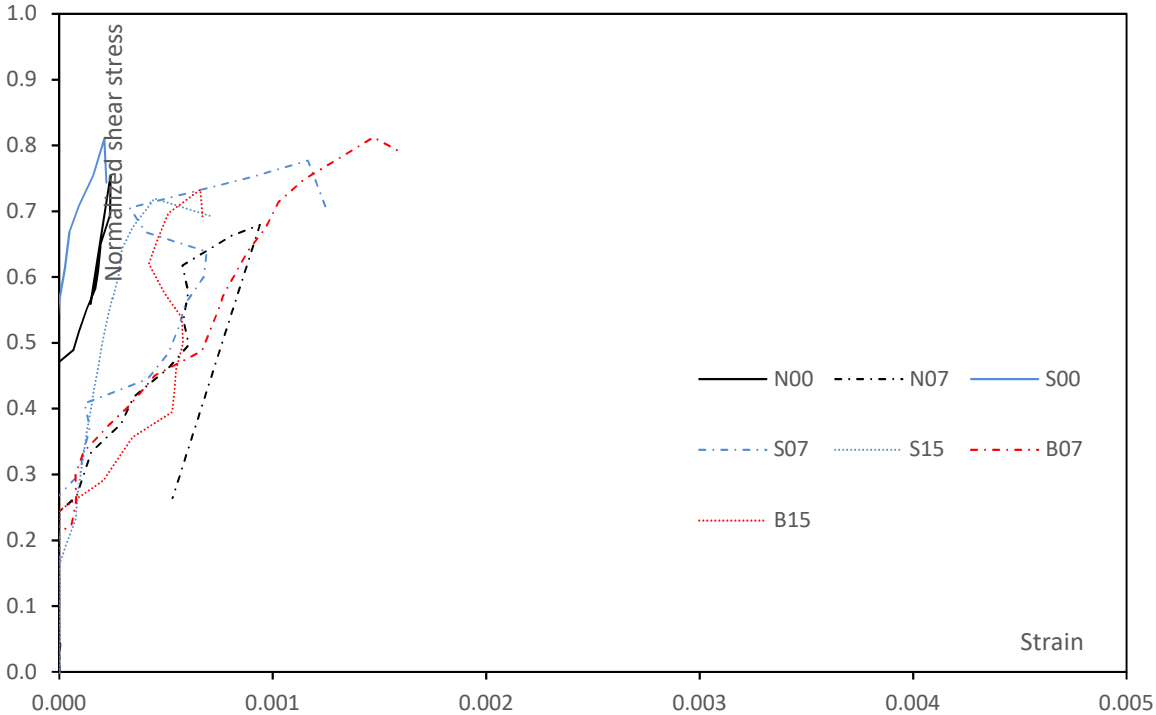

Figure 4.6.3: Normalized shear stress-strain curves for inner shear links

4.7. Strain in the CFRP reinforcement

This section comments on strain in the CFRP composites recorded by the strain gauges. Figure 4.7.1 shows the normalized shear stress-strain variations for the embedded CFRP reinforcement. The behaviour of the embedded CFRP rods was comparable to that of the steel shear links. The normalized shear stresses at which the embedded rods started to function were also in the range of 0.2 to 0.3. For Beam B15, the middle CFRP rod experienced the highest strain at a given load, as it was intersected by the main shear crack (see Figure 4.5.2). At peak load, the strain in the embedded CFRP rods was in the range of 0.0013 to 0.0027.

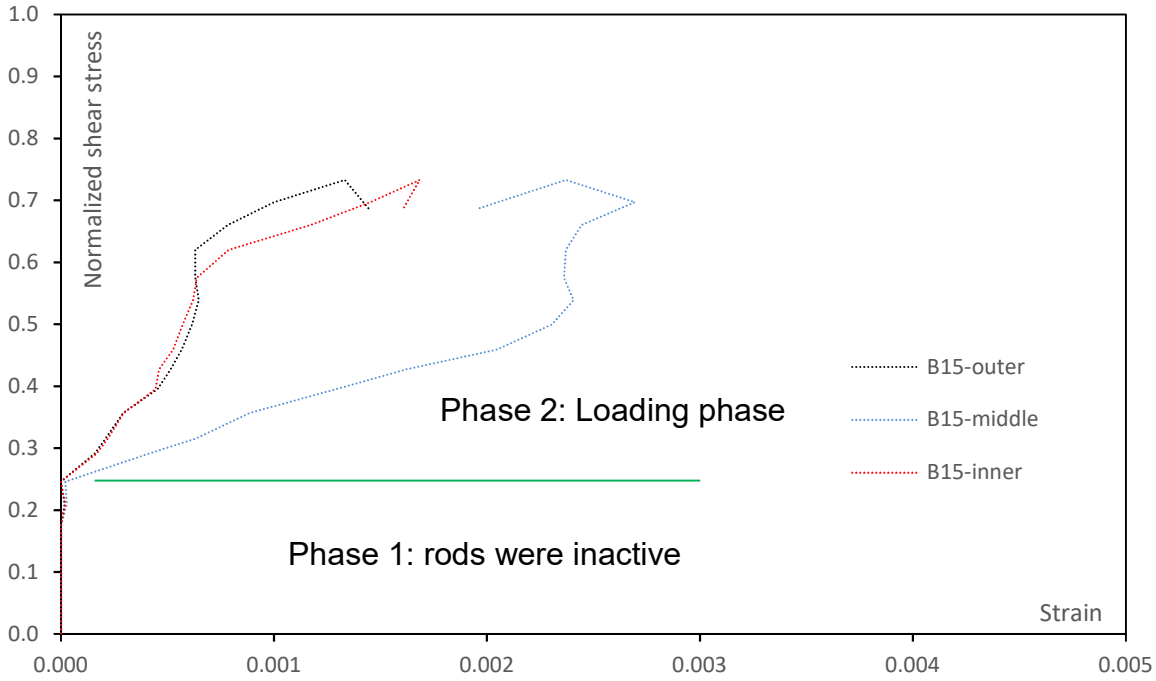

Figure 4.7.1: Normalized shear stress-strain curves for CFRP rods

The normalized shear stress-strain curves for the EB CFRP sheets are shown in Figure 4.7.2. The response of the CFRP sheets can be divided into three phases. Initially, the sheets were inactive up to a normalized shear stress of approximately

0.2 to 0.35. At that load level, which marked the beginning of the second phase, the sheets started to develop tensile strain as they started to resist crack opening. For a given beam, the regions of the CFRP sheets intersected by the inclined cracks developed strain at a higher rate than the remaining regions of the strengthening system. In the third phase, the fabrics started to debond, as shown by the reversing of the normalized shear stress-strain curves, and finally peeled off. At peak load, debonding limited the highest recorded strain in the CFRP sheets to 0.0013.

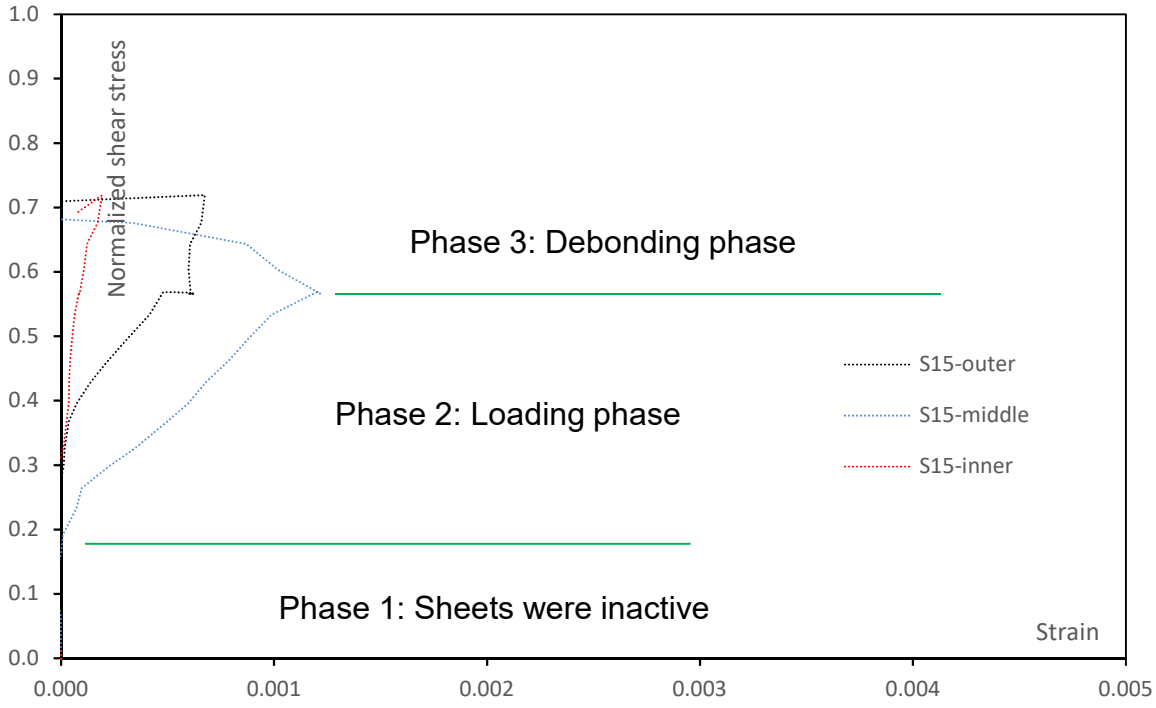

Figure 4.7.2: Normalized shear stress-strain curves for CFRP sheets

Figure 4.7.1 shows that the DE CFRP rods generally had higher strain at failure than the EB CFRP sheets in Figure 4.7.2. This is due to the better bond performance of the DE CFRP rods. Comparable results were reported by Chaallal et al (2011) who also compared EB CFRP sheet strengthened methods to DE CFRP rod strengthened methods for shear strengthening of rectangular RC beams. The DE CFRP rods

generally had higher strain at failure because concrete confinement offers better bond performance of the CFRP rod-to-concrete interface.

4.8. Fibre Bragg grating (FBG) versus strain gauge (SG)

The strain measuring performance of Fibre Bragg grating (FBG) and strain gauge (SG) sensors was also investigated. For comparison purposes, the two systems were installed at about the same locations in selected beams.

The shear links of Beams B00, B07 and S07 were instrumented with FBG and SG sensors. A distributed FBG optical cable consisting of three FBG sensors (i.e. one FBG sensor per shear link) was used for each beam.

The three DE CFRP rods were each instrumented with a SG and a FBG sensor in B07. The FBG monitoring system was made of three FBG cables, with an individual FBG sensor in each cable.

The EB CFRP sheets were instrumented with three SGs and three FBG sensors in S07. Each of the outer, middle and inner regions of the sheets included one SG and one FBG sensor. Due to the FBG cable minimum curvature requirements, the cable was cut into two parts: one part included one FBG sensor which measured the strain in the inner region of the EB CFRP sheet, while the other part included two sensors which measured the strain in the middle and outer regions of the EB CFRP sheet. In this case, the SGs were installed on one side of the sheet whereas the FBGs were attached to the other side.

Figure 4.8.1 compared the readings of SGs and FBG sensors of the strain in the shear links. The shear force and strain gauge readings were recorded using a data

logger. An interrogator was used to obtain the FBG sensor readings, which were matched manually with the shear force readings based on the time at which each dataset was recorded. The results were compared across Beams B00, B07 and S07 in three categories (outer shear link, middle shear link and inner shear link, see Figure 3.2.1).

The curves were designated as either FBG-XXX or SG-XXX-Y. The first part indicates that the reading is from either FBG or SG. The second part, 'XXX', indicates the location (outer, middle or inner, see Figure 3.2.1) of the sensor. Finally, 'Y' indicates that the reading was taken from the SG on the left or right leg of the shear link. For example, SG-middle-L refers to the reading taken from the strain gauge on the left leg of the middle shear link.

The shear force-strain curves generated using the FBG and SG readings were comparable except for the shear links of Beam B00 and the outer shear link in Beam B07. For these shear links, the strain readings of the SG sensor were higher than the strain reading of the FBG sensors under the same shear force. Several factors can affect the SG and FBG readings. Firstly, if the strain gauges are closer to the crack, they will record higher strains. Secondly, Montero et al. (2011) suggested that if the FBG sensors are not correctly protected and if the adhesives are not properly selected, the sensor will give erroneous data. Another possibility is the sensor calibration. Ge et al. (2014) examined the response of four types of strain sensor under controlled temperature changes. Ge et al. (2014) suggested that the variation in the FBG measurements is due to the effect of using inaccurate sensor calibration coefficients. Other factors such as sensor installation (bond between the sensor and

the steel reinforcement) and localised effects (effect of the localised concrete strains on the sensor) could also influence the measurements.

Yielding of the outer and middle shear links in Beam S07 was captured by the FBG sensors, whereas the SG sensors cannot capture the yielding behaviour of steel because of its measurement range. The yielding of the shear links was caused by the sudden opening of the shear crack.

Figure 4.8.2 compares the readings of SGs and FBG sensors of the strain in the CFRP composites. Only four out of six strain gauges produced meaningful results, whereas one FBG sensor produced erroneous results of a shear force of 83.6 *kN* in B07. This erroneous result may be due to sensor failure at the shear force of 83.6 *kN*. The FBG sensor may debond from the CFRP rod, as evinced by the sudden reduction in strain. This might be attributable to the weak bond between the CFRP rod and the FBG sensor. In general, the readings of SGs and FBG sensors were comparable; minor differences might be explained by the proximity of each sensor to the shear crack, installation conditions, and/or calibration factors.

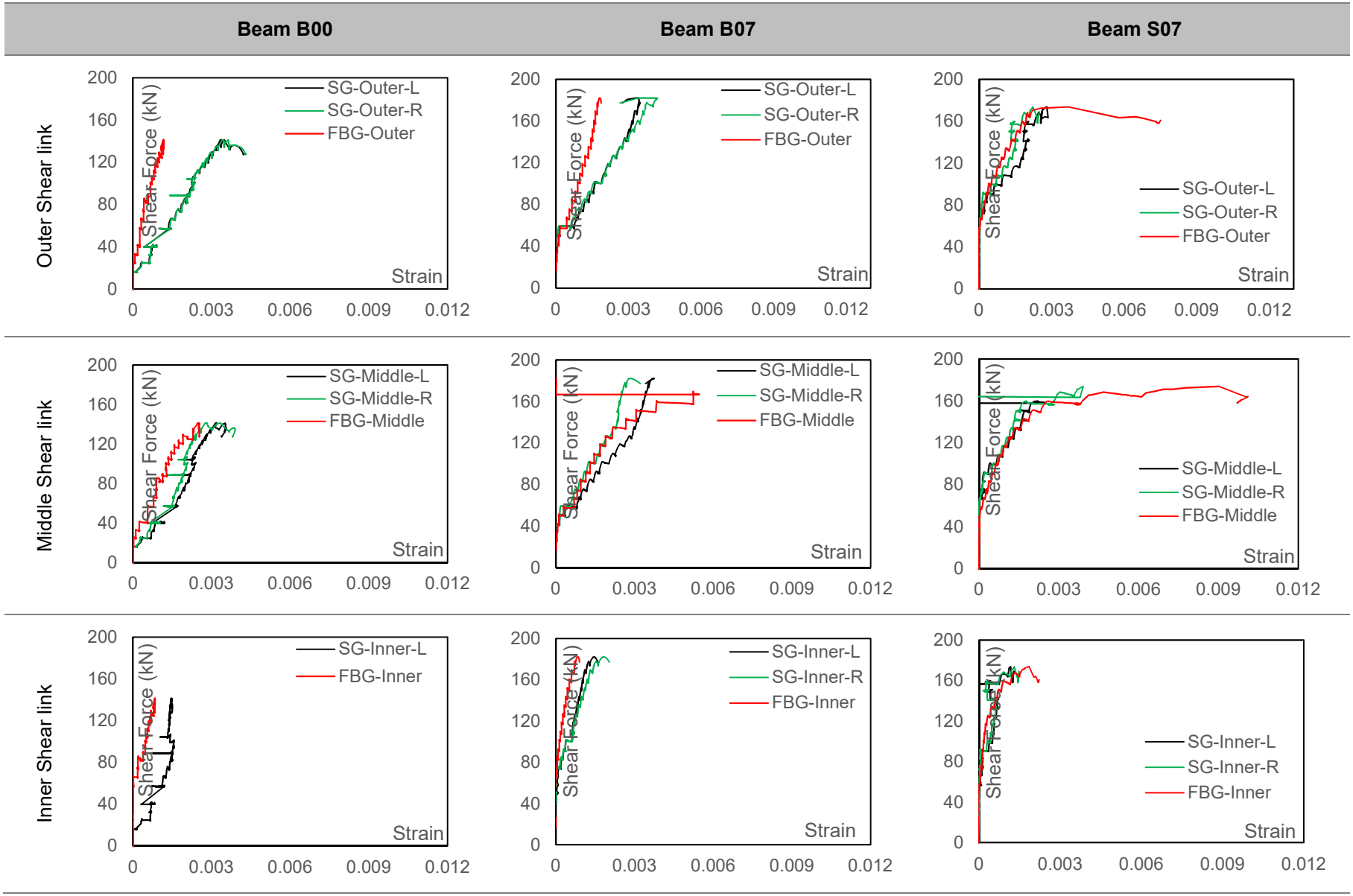

Figure 4.8.1: Comparison between SG and FBG sensor readings for the strain in the steel shear links

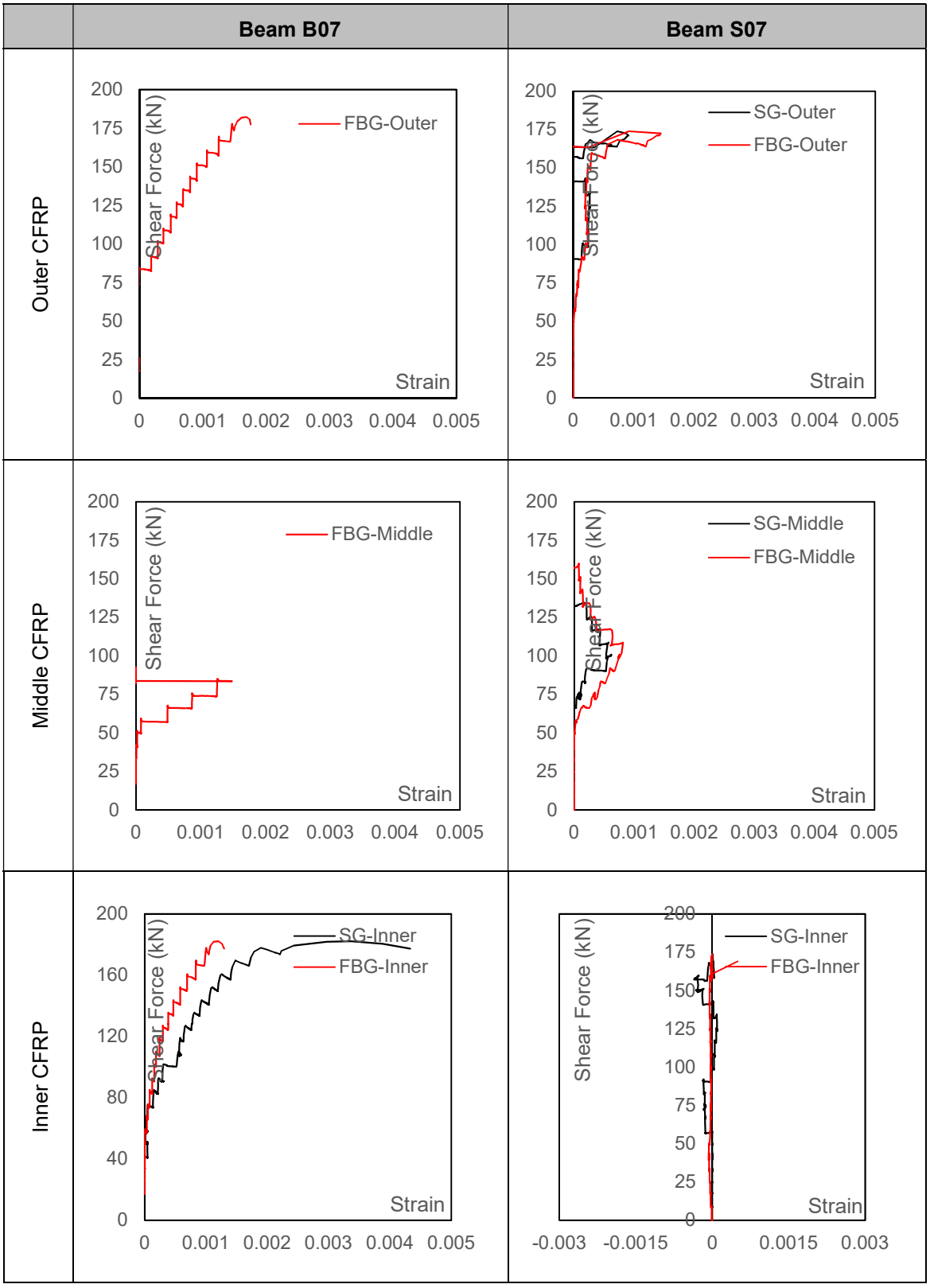

Figure 4.8.2: Comparison between SG and FBG sensor readings for the strain in the CFRP composites

4.9. Influence of corrosion level on the shear capacity components

This section further investigates the effect of corrosion levels on the magnitude of the shear capacity components in unstrengthened RC T-beams.

Beams N00, N07 and N15 were used to illustrate the effect of corrosion levels. The experimentally measured total shear capacity, V_{total}, can be expressed as the sum of the contributions from the concrete, V_c, and the steel, V_s; see Equation 4.3.

$$V_{total} = V_c + V_s \tag{4.3}$$

The shear contribution of each component is based on the free-body diagram of a part of the specimen separated along the critical crack that causes failure. The steel contribution, V_s, can be expressed as the sum of the forces in the shear links crossed by the main shear crack. Depending on whether a shear link yielded at failure or not, its contribution can be calculated according to Equation 4.4. The steel contribution, V_s, is calculated according to Equation 4.5.

$$\begin{cases} V_{si} = A_{si}\varepsilon_{si}E_s & \text{if } \varepsilon_{si} < \varepsilon_y \\ V_{si} = A_{si}f_y & \text{if } \varepsilon_{si} \geq \varepsilon_y \end{cases} \tag{4.4}$$

$$V_s = \sum_{i=1}^{n} V_{si} \tag{4.5}$$

where:

V_{si} Force in the '*i*' - th shear link (*N*).

ε_{si} Strain in the '*i*' - th shear link.

A_{si} Area of the '*i*' - th shear link (mm^2).

E_s Elastic modulus of steel (N/mm^2).

f_y Yield strength (N/mm^2).

ε_y Yield strain

The shear contribution of the concrete, V_c, is calculated by subtracting the steel contribution, V_s, from the total shear capacity measured during the test, V_{total}:

$$V_c = V_{total} - V_s \quad (4.6)$$

Based on the calculations described above, the shear component diagrams were drawn for Beams N00, N07 and N15, as shown in Figure 4.9.1 to Figure 4.9.3.

Figure 4.9.1 to Figure 4.9.3 show that increasing the corrosion level from 0% to 7% did not significantly affect the steel contribution, which varied from 103 *kN* to 105 *kN* respectively. However, when the corrosion level was increased to 12%, the steel contribution dropped to 83 *kN*, which is 19.4% less than the steel contribution in the control beam. As explained in Section 4.2, increasing the corrosion level detrimentally affects the physical and mechanical properties of the shear links. This, in turn, reduces the contribution of the shear links to the total shear capacity.

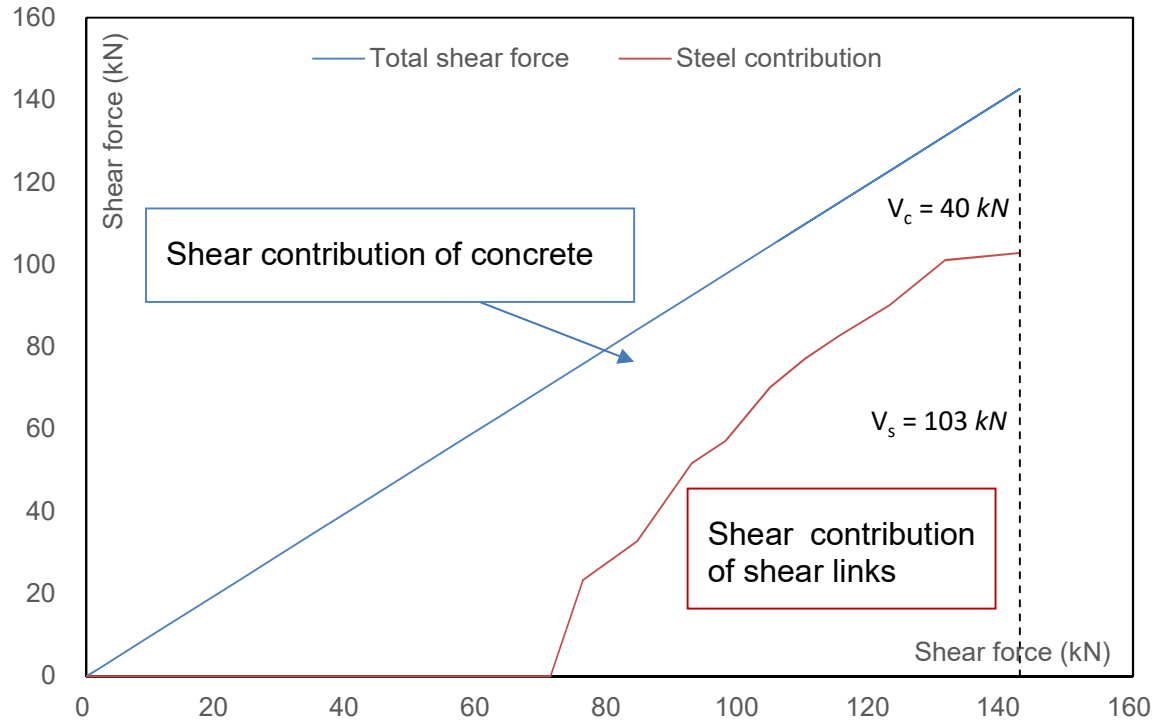

Figure 4.9.1: Shear resistance components diagram for Beam N00

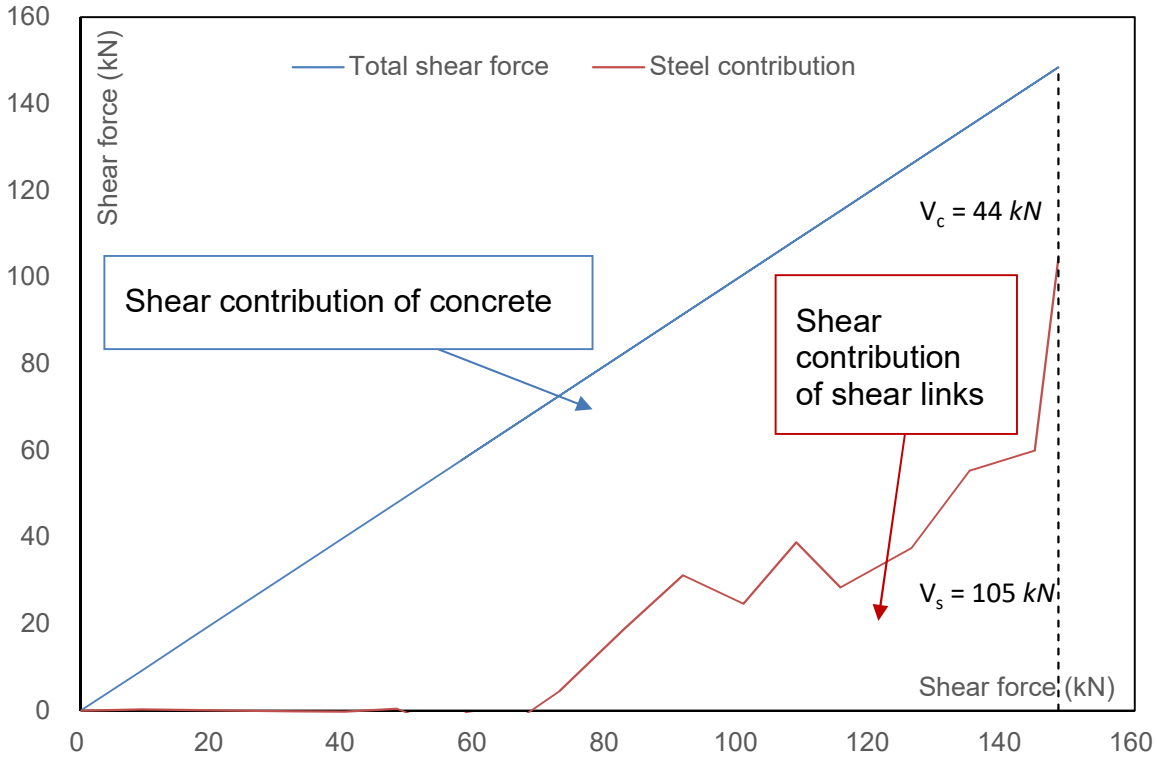

Figure 4.9.2: Shear resistance components diagram for Beam N07

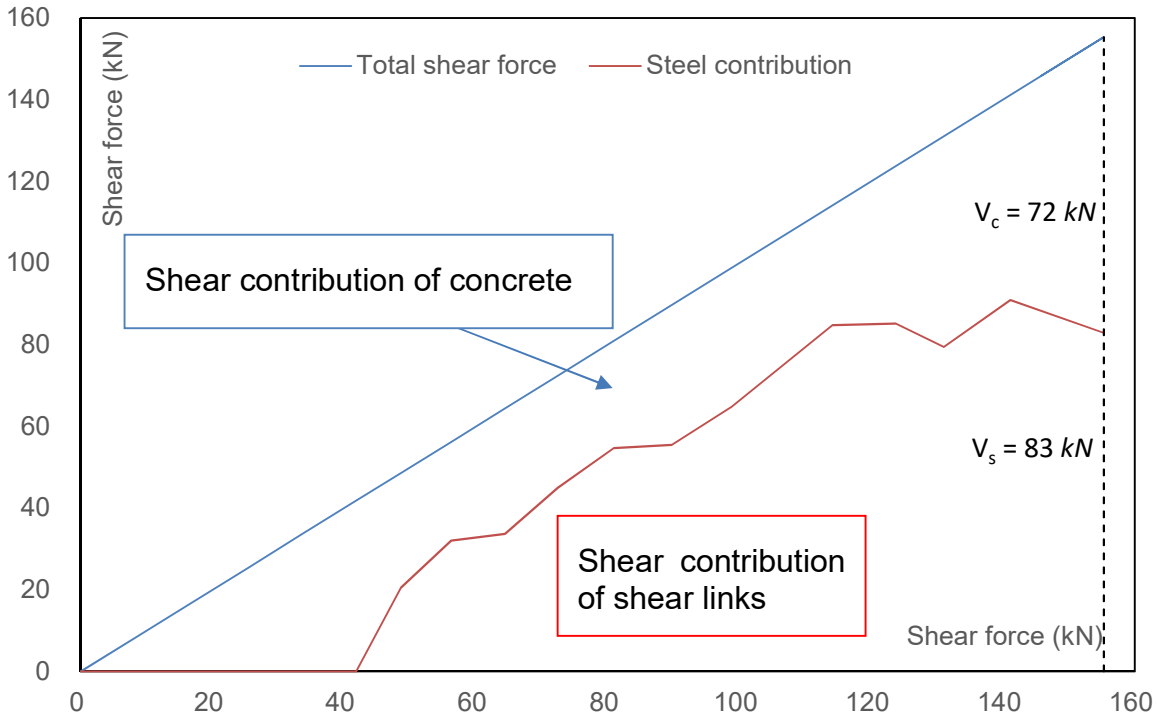

Figure 4.9.3: Shear resistance components diagram for Beam N15

Due to the difference in the concrete strength of the unstrengthened beams, the concrete contribution, V_c, should be normalized according to Equation 4.7.

$$V_{c,nomalized} = \frac{V_{c,actual}}{\sqrt{\frac{f_{cu,exp}}{f_{cu,control}}}} \qquad (4.7)$$

where:

$V_{c,nomalized}$ Normalized concrete contribution (*N*).

$V_{c,actual}$ Actual concrete contribution (*N*).

$f_{cu,exp}$ Beam concrete cube compressive strength (*N/mm²*).

$f_{cu,control}$ Control beam concrete cube compressive strength (*N/mm²*).

In Equation 4.7, $f_{cu,control}$ was taken as 26.3 *N/mm²* which was the concrete cube compressive strength of Beam N00.

Figure 4.9.4 shows the variation of each component with regard to corrosion level. The general trend is that steel contribution decreases with an increasing corrosion level, as explained above. It can also be observed that concrete contribution increases with an increasing corrosion level. This result should be considered cautiously, as it is directly influenced by the normalisation used in Equation 4.7. If the cube root of the concrete strength is used instead of the square root (for example: BS 5400: Part 4 for design RC beams with shear links), concrete contribution will be more pronounced. Further research is required to fully understand the effect of corrosion levels on concrete contribution.

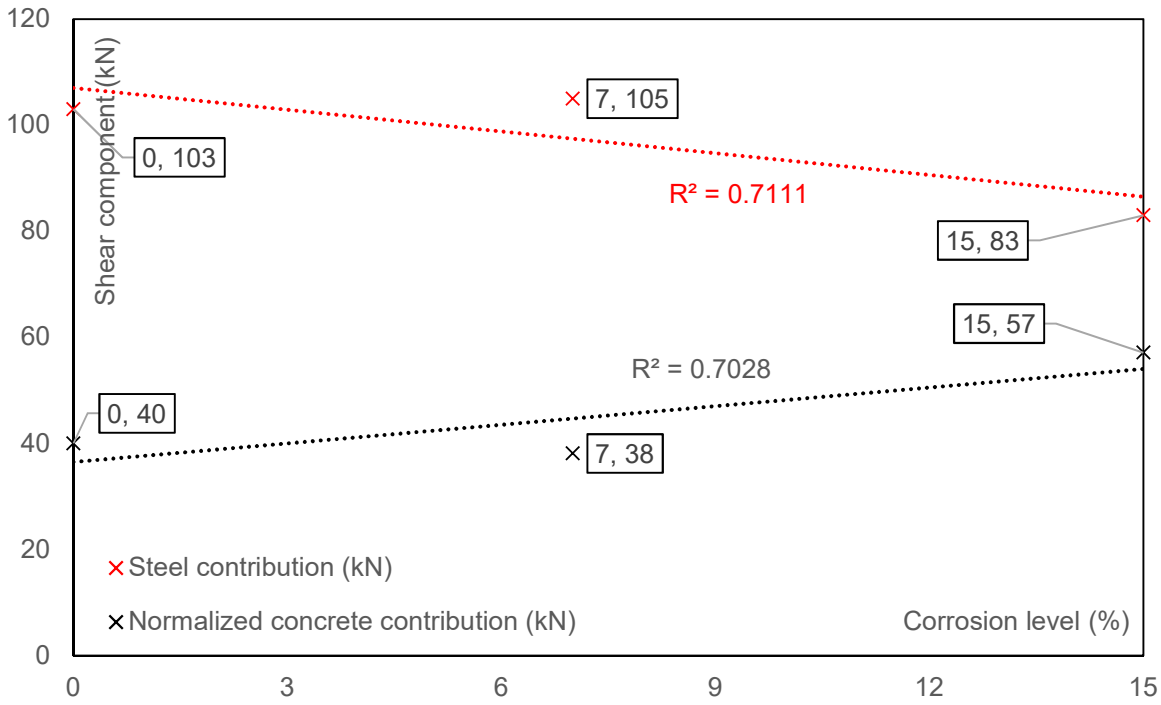

Figure 4.9.4: Effect of corrosion level on shear resistance components

4.10. Contributions of the CFRP strengthening systems

This section further examines the contribution of CFRP strengthening systems to shear force capacity. For CFRP-strengthened beams, the total shear force, V_{total}, was

calculated as the sum of the contribution of the concrete, V_c, the steel, Vs, and the CFRP composites, V_f.

$$V_{total} = V_c + V_s + V_f \quad (4.8)$$

The total shear force carried by the CFRP composites, V_f, was computed using the following equation:

$$V_f = \sum A_{fi} f_{fi} = \sum A_{fi} \varepsilon_{fi} E_f \quad (4.9)$$

A_{fi} is the area where strain is measured. f_{fi} is the CFRP stress. E_f is the modulus of elasticity of the CFRP, and ε_{fi} is the averaged strain in the CFRP composite.

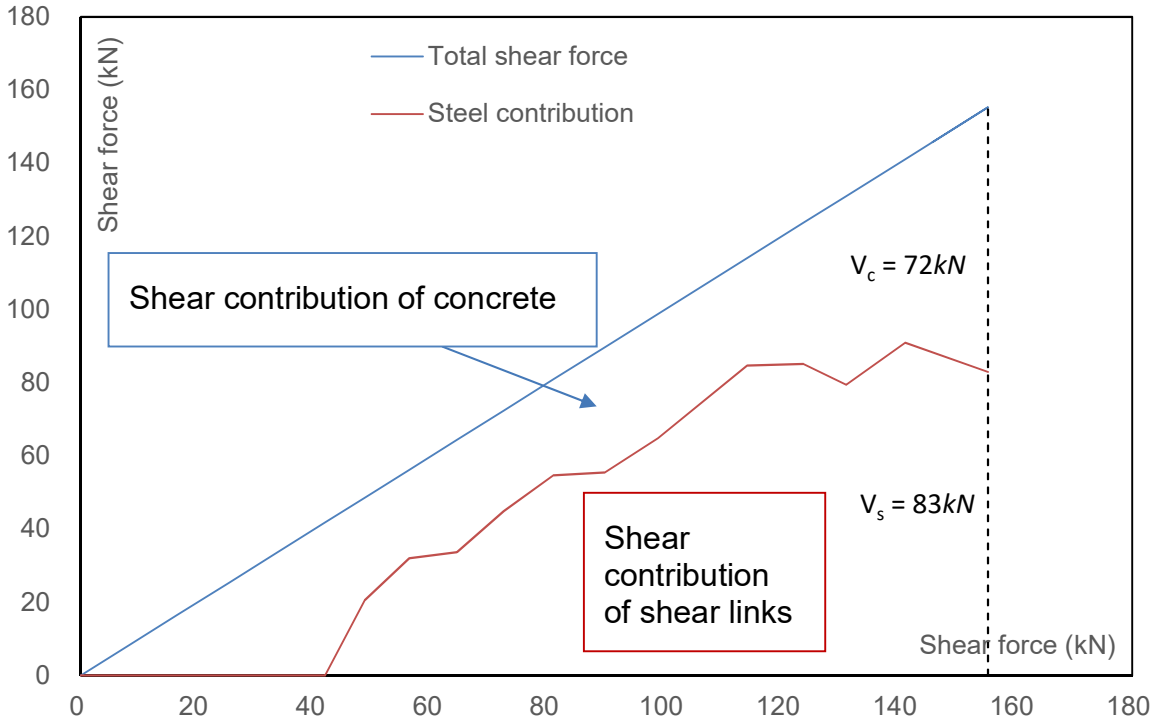

Figure 4.10.1: Shear resistance components diagram for Beam N15

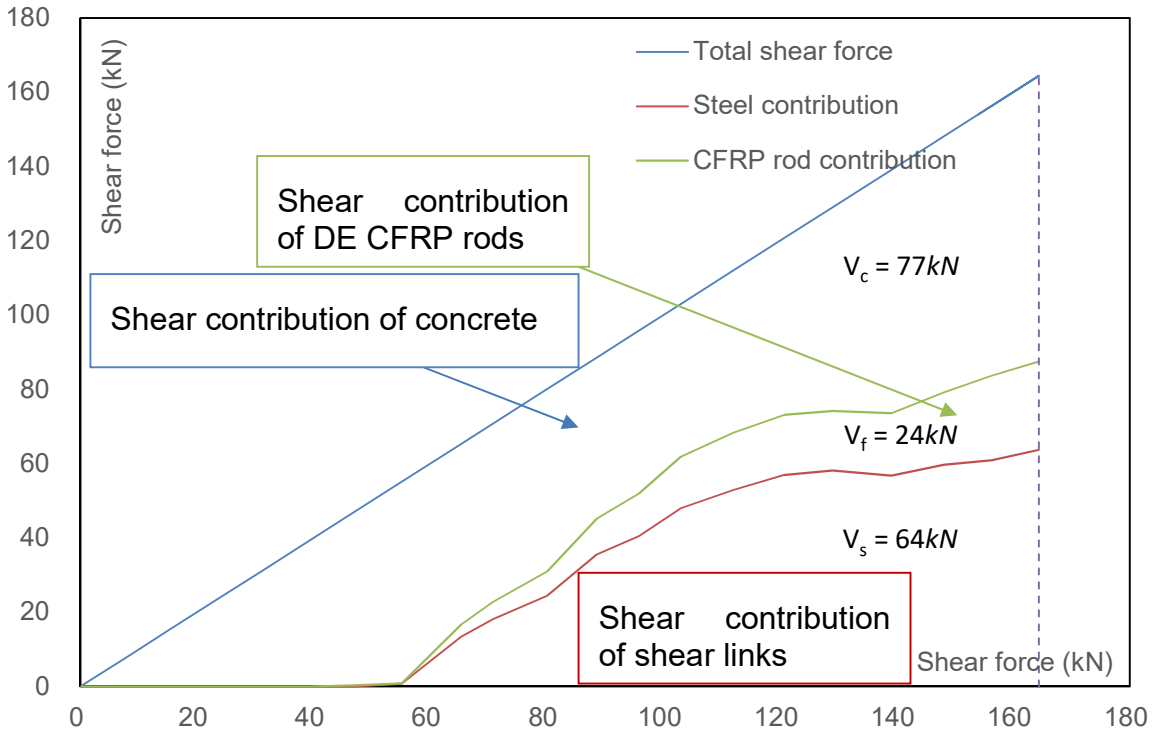

Figure 4.10.2: Shear resistance components diagram for Beam B15

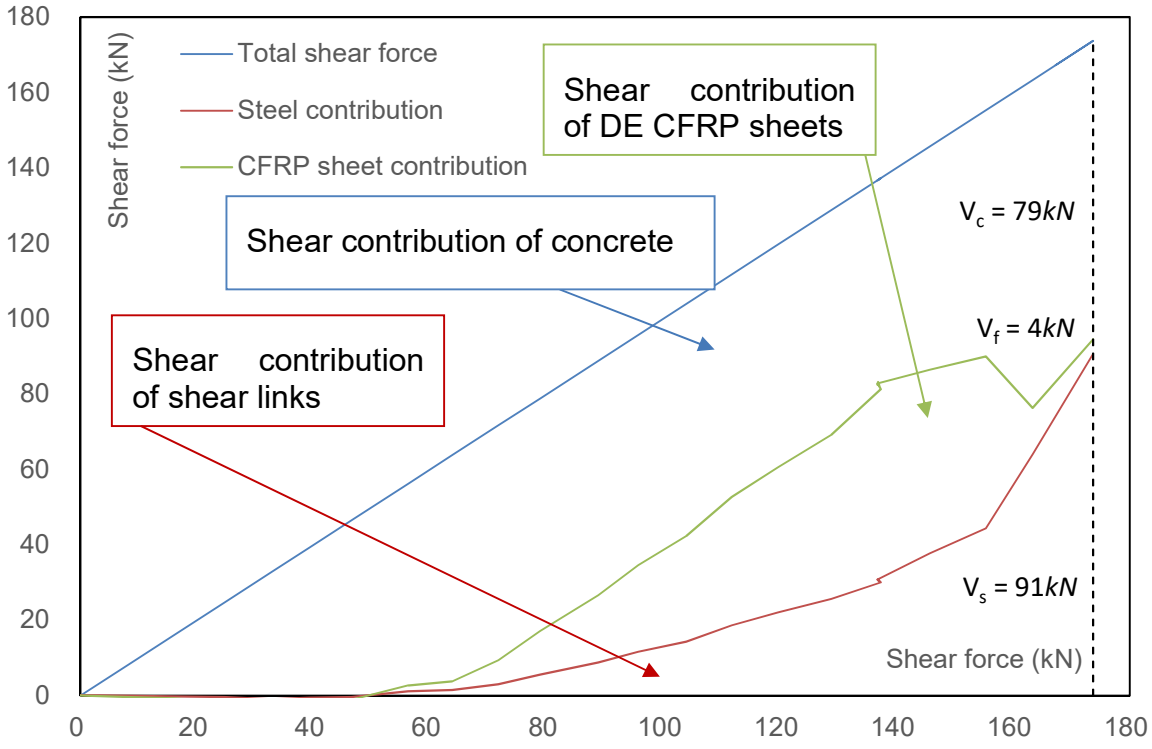

Figure 4.10.3: Shear resistance components diagram for Beam S15

Due to failure of some strain gauges, the contributions of the CFRP strengthening systems were compared among Beams N15, B15 and S15, as shown in Figure 4.10.1 to Figure 4.10.3 respectively.

Figure 4.10.1 to Figure 4.10.3 clearly demonstrate the superiority of the DE technique. At ultimate load, the DE CFRP rods in Beam B15 were carrying 24 *kN* (14.5%), whereas the EB CFRP sheets (4 *kN* / 2.3%) did not significantly contribute to the shear resistance due to debonding.

To eliminate the effect of the concrete cube compressive strength, the normalized concrete contribution, $V_{c,normalized}$, was calculated according to Equation (4.7). Table 4.10.1 suggests that the concrete contribution is about 46% to total shear capacity. In such cases, ignoring the concrete contribution as suggested by some code of practice (e.g. Eurocode 2) would lead to inaccurate estimations of the total shear capacity. Table 4.10.1 also suggests that un-anchored EB CFRP sheets contribute insignificantly to total shear capacity at ultimate load.

Table 4.10.1: Shear resistance components of 15% corroded beams

Beam	Average cube compressive strength (N/mm^2)	Normalized concrete contribution (*kN*)	Steel contribution (*kN*)	CFRP contribution (*kN*)
N15	41.8	72	83	-
B15	37.0	82	64	24
S15	42.9	78	91	4

4.11. Conclusions

The aim of the experimental work was to investigate the shear behaviour of uncorroded and corroded RC T-beams shear strengthened with CFRP systems. This chapter has presented the results of an experimental investigation. The actual shear

link corrosion levels, obtained using gravimetric mass loss, were 0% (un-corroded), 7%, and 12%. Based on the results of this study, the following conclusions were drawn:

1. Both the mechanical and physical properties of the shear links deteriorate with increasing corrosion levels.
2. The unstrengthened beams with shear link corrosion levels of 7% and 12% had shear strengths that were 11% and 14% respectively, less than the shear strength of the un-corroded unstrengthened beam.
3. The shear link corrosion level of 7% did not have a significant effect on the shear strength of the strengthened beams. The beams with a shear link corrosion level of 7%, and strengthened with the DE or EB CFRP systems, had comparable shear strengths to the corresponding un-corroded strengthened beams.
4. At corrosion level of 12%, the strengthened beams had shear strengths that were approximately 12% less than the corresponding values for the un-corroded, strengthened beams. Moreover, the strengthened beams had shear strengths that were approximately 4% to 5% less than the shear strength of the un-corroded, unstrengthened beam. Hence, the strengthening systems were almost, but not quite, effective at returning the beams with the 12% shear link corrosion level to their un-corroded shear strength.
5. The effectiveness of both strengthening systems decreased with increasing shear link corrosion levels. The shear strength enhancement provided by the DE and EB CFRP systems decreased from 19% and 15% respectively, to 12% and 11% respectively, with an increase in shear link corrosion level from 7% to 12%.
6. The corrosion level had an insignificant effect on the deflection response of the strengthened beams. The stiffness of the unstrengthened beams decreased with increasing corrosion levels.
7. The beams strengthened with the EB technique had a stiffer response and less strain in the shear links when compared with the corresponding beams

strengthened with the DE technique.

8. Debonding resulted in limited strain in the CFRP sheets (less than 0.0013). On the other hand, the embedded CFRP rods did not show signs of debonding, and developed higher strains (0.0013 – 0.0027) when compared with the EB sheets.
9. Strain analysis suggested that steel contribution to total shear capacity decreases with an increasing corrosion level. The EB CFRP sheets, which were un-anchored in this study, did not contribute to total shear capacity, whereas concrete contribution was about 46% to total shear capacity of the strengthened beams with a 12% corrosion level.

CHAPTER 5: NUMERICAL SIMULATION

5.1. Introduction

The aim of this chapter is to develop non-linear finite element (NLFE) predictive tools capable of modelling the behaviour of the experimental specimens. In order to achieve this goal, the NLFE analysis and the validation of the proposed finite element (FE) models are presented. The methodology of modelling concrete, reinforcement and carbon fibre reinforced polymer (CFRP) composites are discussed in Sections 5.2, 5.3 and 5.4 respectively. In each section, the material model, section property and element type are discussed. The solution procedure is illustrated in Section 5.5 and Section 5.6 presents the validation of the proposed FE models. The results of experimental tests are used to validate the NLFE models. Sections 5.6.1, 5.6.2 and 5.6.3 compare the predicted shear force capacity, shear force-deflection curves and crack patterns with experimental results respectively. Section 5.7 presents the key findings from the numerical simulation.

5.2. Concrete cracking

To study concrete failure in tension, the cracking behaviour of concrete should be modelled adequately. Tensile failure of concrete involves micro-crack propagation within the concrete, de-bonding between concrete and slave materials, and other internal damages. These damages lead to the softening regime, which eventually causes geometrical discontinuity in the concrete. There are two kinds of concrete cracking models available to simulate cracking behaviour numerically: the discrete

crack model and the smeared crack model.

5.2.1. *Concrete cracking modelling*

Discrete crack concept (Figure 5.2.1a) introduced the crack into FE models manually by means of a separation between element edges (Scordelis and Ngo, 1967 and Nilson, 1968). The discrete crack concept represents the behaviour of crack propagation but, it also has disadvantages. It is difficult to fit with the FE displacement method, especially in three-dimensional (3D) analysis, as it requires an updated meshing configuration with the crack development. Secondly, the crack is constrained to follow a predefined path along the element edges.

Rashid (1968) developed another crack approach which is called the smeared crack concept (Figure 5.2.1b). This approach introduces a weakened material property to mimic the crack development. This treatment allows the cracks and cracking development level to be described using the same notion of stress and strain. It offers a simple solution to the concrete cracking problem. The approach switches from the initial isotropic constitutive law to an orthotropic law upon crack formation, with the orthotropic axis being determined according to a condition of crack initiation. The smeared crack concept produces results that are more representative of the "bands of micro-cracks" that blunt fracture in matrix-aggregate composites like concrete.

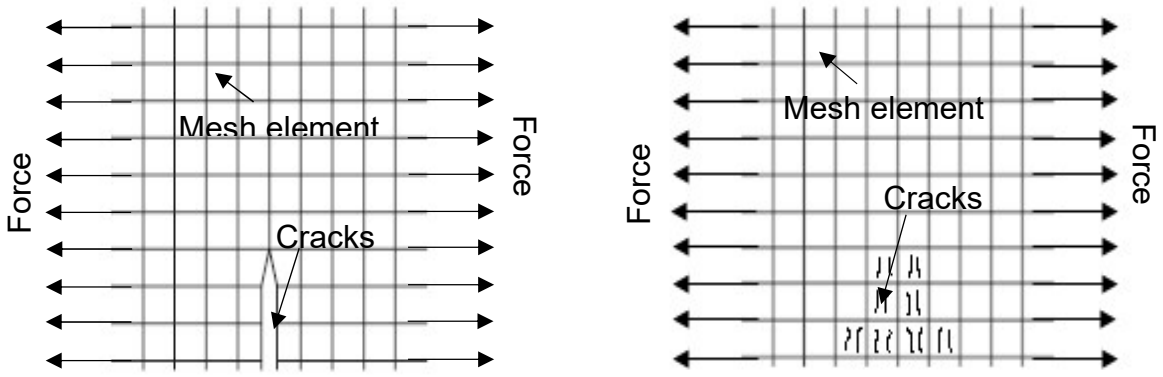

(a) Discrete Crack Concept (b) Smeared Crack Concept

Figure 5.2.1: Concrete cracking concepts
- Rots and Blaauwendraad (1989)

In the FE simulation, the smeared crack concept was adopted. There are two types of smeared crack approaches: the fixed smeared cracking approach and the rotating smeared cracking approach. For the fixed smeared cracking concept, the orientation of the crack is fixed during the numerical computational process, whereas a rotating concept allows the orientation of the crack to co-rotate with the axis of principal strain. Details are described in the following section.

5.2.2. *Smeared crack concept*

With the fixed smeared cracking approach, the orientation of the crack is fixed. This leads to physically unrealistic and distorted crack patterns. To avoid increasing the capacity estimation caused by a fixed angle, a shear retention factor β ($0 \leq \beta \leq 1$) is introduced. This shear retention factor not only reduces numerical difficulties, but also improves the capability of the fixed smeared cracking model. Bédard and Kotsovos (1986) showed that the shear retention factor could vary even for similar experimental tests. The unpredictable shear retention factor is not recommended for use in industrial predictions. Hence, the fixed smeared crack concept is not

considered in the FE simulation.

The rotating smeared crack approach considers the change of crack direction with the change in the direction of the principal tensile stress. Hence, the crack plane is always a principal plane with no shear stresses (Qapo et al., 2014). Therefore, explicit modelling of the concrete shear behaviour after cracking, e.g. via a shear retention factor, is not required. However, Dirar et al (2013) suggested that the predicted shear capacity is normally lower than the experimental results, but that the prediction is acceptable. It should also be noted that, due to the unbalanced loading on the test beams and heterogeneous nature of reinforced concrete beams, the predicted initial crack may differ to the actual crack locations. However, these effects were considered to be insignificant. Hence, the rotating smeared crack concept is adopted to simulate the cracking behaviour of concrete in this research. A description of the crack models can be found in DIANA user manual (2012).

5.2.3. *Concrete geometry*

Qapo et al. (2014) and many other researchers have successfully modelled concrete, by using eight-node isotropic solid brick elements (Figure 5.2.2(a)) that have three translational degrees of freedom at each node, with TNO DIANA. TNO DIANA also offers a six-node isotropic solid wedge element (Figure 5.2.2(b)) that has three translational degrees of freedom at each node. These two elements were compared by simulating the experimental test of Beam N00.

(a) Eight-node brick element (b) Six-node wedge element

Figure 5.2.2: Solid elements for concrete modelling
- TNO DIANA (2012)

The wedge element and brick element gave predicted shear force capacities of 9.5% and 32.4% lower than the experimental results, respectively (see Figure 5.2.3). The shear force-deflection curve also fitted well when comparing the FE predictions to the results of experimental tests on N00. It should be noted that the numerical model predicted a load drop after maximum shear force was achieved, due to beam failure in shear; post behaviour was not investigated in this research. Therefore, wedge elements were used to simulate the concrete.

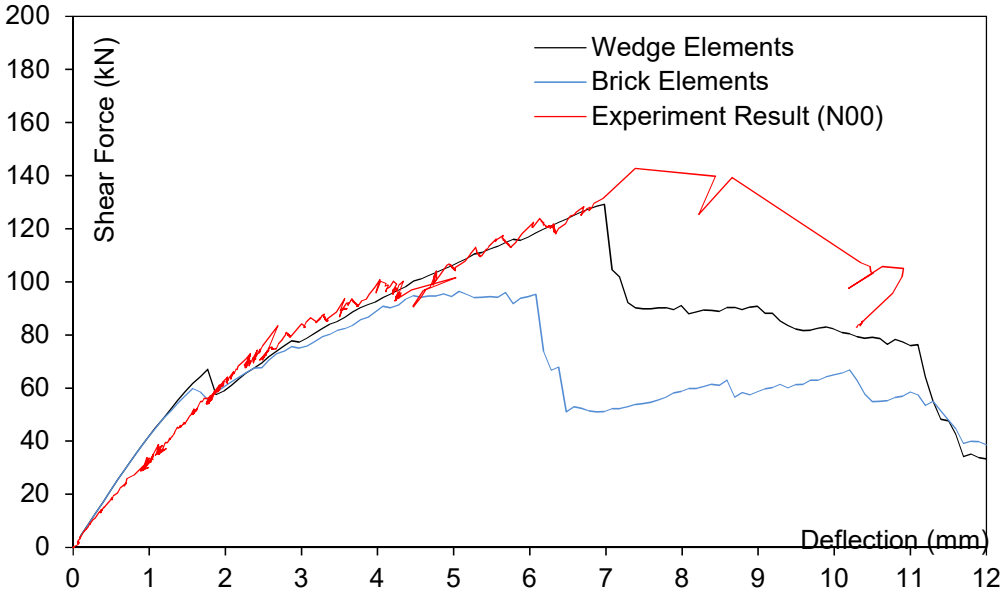

Figure 5.2.3: Effect of element type on the shear force-deflection curves for Beam N00

The improvements using a wedge element may be caused by the flexibility of the wedge element, which is not enough to mesh the object, especially where they are quite crowded. Brick elements may lead to some ‘bad’ elements, such as large aspect ratio and distorted shape etc.

Figure 5.2.4 shows the mesh arrangement of the proposed FE models. Different concrete meshing sizes were examined and a recommendation from Bažant and Oh (1983) suggested that a meshing size of three times the maximum aggregate size, d_a, (3 x 10 *mm* = 30 *mm*) should be used to achieve a good FE simulation. Due to the location of loading pad and bearing plates, the average meshing size of un-strengthened, deep embedded (DE) strengthened and externally bonded (EB) strengthened models were 22 *mm*, 22 *mm* and 21 *mm* respectively. This mesh size gave a good agreement in the results between numerical models and experimental tests.

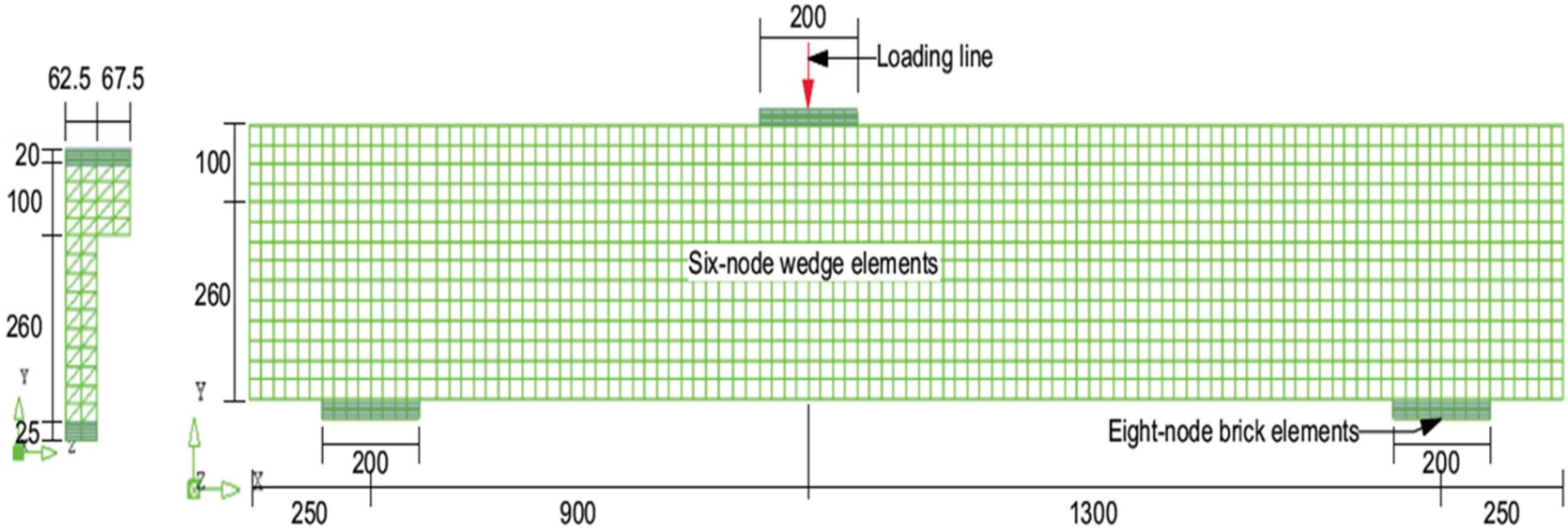

Figure 5.2.4: Mesh arrangement of the proposed model

- dimensions are in *mm*

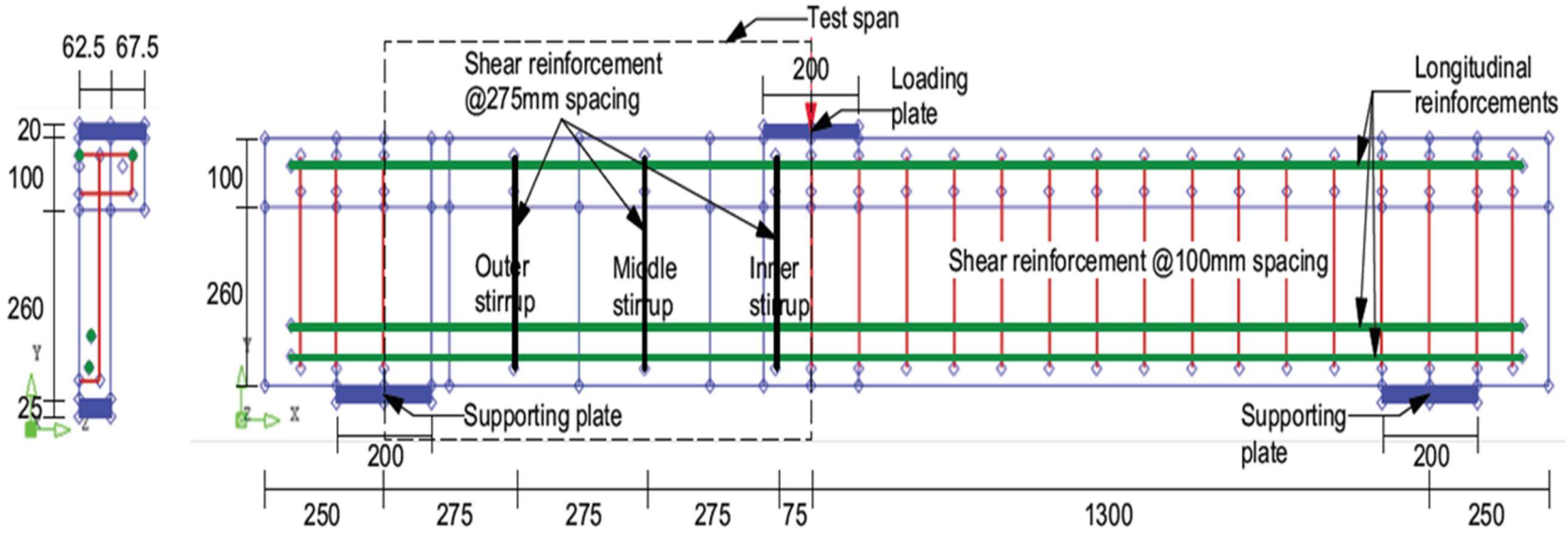

Figure 5.2.5: Proposed FE model for tested beams

- dimensions are in *mm*

Figure 5.2.5 presented the proposed model arrangement of the unstrengthened test beams. As the T-beam was symmetrical about its centreline of cross-section, only half of the beam was modelled. The beam was loaded under a three-point loading test system, where the length of the test span and non-test span were 900 *mm* and 1300 *mm*, respectively, with 250 *mm* overhangs at each end. The overall depth of the T-section was 360 *mm*. Two bearing plates and one loading plate were also simulated with solid elements. Figure 5.2.5 showed the three shear links within the test span, were named as outer, middle and inner shear links, at a centre-to-centre spacing of 275 *mm*. The DE CFRP rods were located at the middle of the centreline of the test span support to the outer shear link, the outer shear link to middle shear link and the middle shear link to inner shear link. The EB CFRP sheets were modelled with two-node truss elements across the test span, at a spacing of element size 22 *mm* for unstrengthened and DE strengthened beams or 21 *mm* for EB strengthened beams.

5.2.4. *Concrete material properties*

The compressive behaviour of concrete was considered as well as the tension behaviour. The compressive behaviour of concrete was represented by the constitutive model proposed by Thorenfeldt et al. (1987). Figure 5.2.6(a) illustrates graphically the possible concrete compressive behaviour of Thorenfeldt et al. (1987). The constitutive relationship can be estimated automatically by giving the concrete cylinder compressive strength. A Poisson's ratio of 0.20 gave the best prediction, as demonstrated in Section 5.6. The same Poisson's ratio was also used by several researchers, such as Potisuk et al. (2011). Time dependent effects, such as creep

and shrinkage of concrete and the effects on strength of sustained load, were not included in the present numerical analysis.

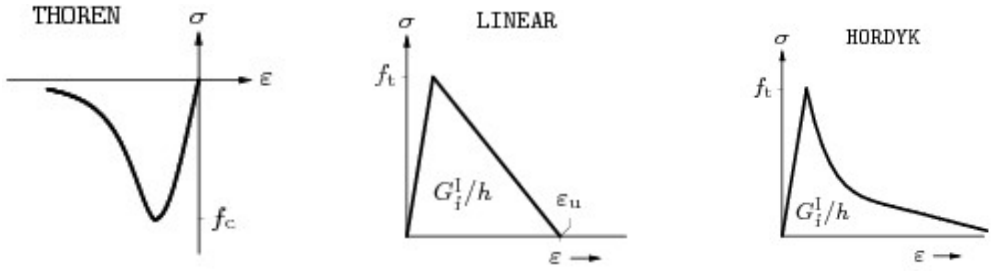

(a) (b) (c)

Figure 5.2.6: Concrete constitutive models
- TNO DIANA (2012)

The tensile behaviour of concrete was determined by comparing two different tensile models. The bi-linear approximation model (Figure 5.2.6b) increases the tensile stress linearly up to the uniaxial tensile strength, f_{ct}. It was followed by a linear softening behaviour. Hordijk et al (1986) proposed a parabolic softening behaviour rather than linear softening (Figure 5.2.6(c)). The parabolic softening model utilises a more realistic representation of the tensile stress-strain curve of concrete in softening behaviour. However, the bi-linear model gives a comparable prediction to Hordijk et al (1986), when simulating N00 and comparing the FE predictions with experimental results (see Figure 5.2.7). Hence, the bi-linear tensile model was adopted because of the simplicity of model requirement.

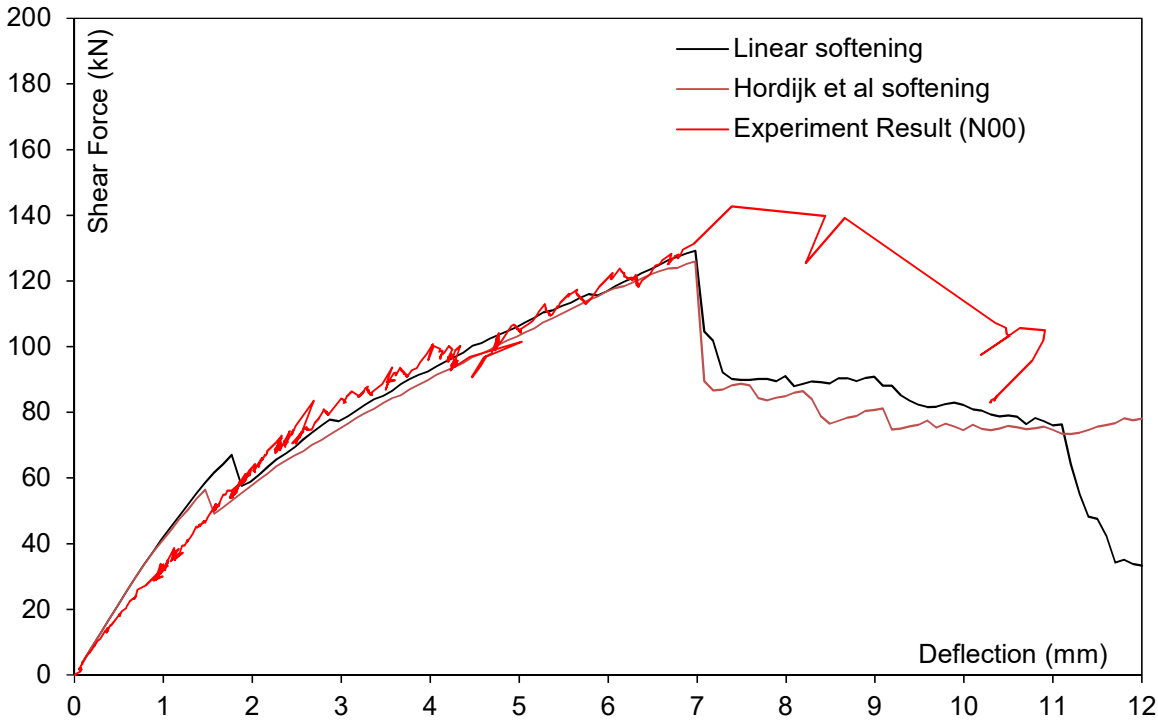

Figure 5.2.7: Effect of concrete tensile models on the shear force-deflection curves for Beam N00

The modulus of elasticity, E_c, was calculated based on the formulae proposed by Wang et al. (1978). The concrete cube compressive strength, f_{cu}, was obtained from the concrete cube compression test, which was tested on the day of the beam testing. The cylinder compressive strength, f_{cy}, was expressed as Equation 5.1, which was a function of cube compressive strength (Eurocode 2: EN 1992-1-1).

$$f_{cy} = 0.8 f_{cu} \qquad (5.1)$$

where:

f_{cy} Concrete cylinder compressive strength (N/mm^2).

f_{cu} Concrete cube compressive strength (N/mm^2).

Several models are available to predict the concrete uniaxial tensile strength, f_{ct}. In Section 5.6, it shows that the Equation 5.2 (ACI 318-11) offered a more accurate FE

prediction. Hence, the uniaxial tensile strength of concrete is derived from Equation 5.2.

$$f_{ct} = 0.56 f_{cy}^{0.5} \tag{5.2}$$

where:

f_{ct} Concrete tensile strength (*N/mm²*).

f_{cy} Concrete cylinder compressive strength (*N/mm²*).

The averaged crack bandwidth, *h*, is given by Equation 5.3, which is recommended by TNO DIANA:

$$h = \sqrt[3]{\frac{b_f d_f l + b_w d_w l}{n_e}} \tag{5.3}$$

where:

h The crack bandwidth (*mm*).

b_f Modelled flange width (130 *mm*).

d_f Modelled flange depth (100 *mm*).

l Modelled beam length (2700 *mm*).

b_w Modelled web width (62.5 *mm*).

d_w Modelled web depth (260 *mm*).

n_e Modelled number of concrete element

The fracture energy, G_f, was expressed as Equation 5.4 which was proposed by Phillips and Binsheng (1993). Dirar et al. (2012) carried out a series of successful FE simulations on pre-cracked RC T-beams repaired in shear with CFRP sheets, by using the same fracture energy model.

$$G_f = (43.2 + 1.13f_{cu}) \times 10^3 \quad (5.4)$$

where:

G_f Concrete fracture energy (*N/mm*).

f_{cu} Concrete cube compressive strength (*N/mm²*).

The ultimate concrete tensile strain, $\varepsilon_{c,ult}$, can be expressed as Equation 5.5 because of the assumption of linear softening.

$$\varepsilon_{c,ult} = \frac{2G_f}{hf_t} \times 10^{-3} \quad (5.5)$$

where:

$\varepsilon_{c,ult}$ Ultimate concrete tensile strain.

G_f Concrete fracture energy (*N/mm*).

h The crack bandwidth (*mm*).

f_t Concrete cylinder tensile splitting strength on the day of test (*N/mm²*).

5.3. Modelling of steel reinforcement

Steel reinforcement is another major component in the RC structure. Hence, truly representing the behaviour of steel reinforcement is also important.

5.3.1. *Geometry properties of steel reinforcement in FE analysis*

The reinforcement can be modelled as a two-node truss element in most commercial software. However, DIANA offers a more comprehensive element known as embedded reinforcement element. The strain in the reinforcements (slave element) is calculated from the displacement field of the concrete (master element). This implies a perfect bond (no relative displacement between the master and slave elements)

between the reinforcement and the surrounding material. DIANA also offers a user-defined bond-slip relationship, integrated with the embedded reinforcement element, to present the interface behaviour of reinforcement to concrete.

After the experimental test, no longitudinal crack was noticed along the longitudinal reinforcement. Menzel and Woods (1952) also suggested that end anchorage with steel plates could be a sufficient reinforcement anchorage method. Hence, the aluminium pigmented epoxy coated reinforcement was simulated with a perfect-bond behaviour of the steel-to-concrete interfaces. The longitudinal reinforcement anchorage plates were not simulated in the FE models. The material properties and section dimensions were based on the data obtained from the experimental test.

For the corroded shear links at test span, many forms of corrosion may develop. Uniform corrosion (Figure 5.3.1a) and localised pitting corrosion (Figure 5.3.1b) are commonly considered as the dominant corrosion types in most numerical analysis.

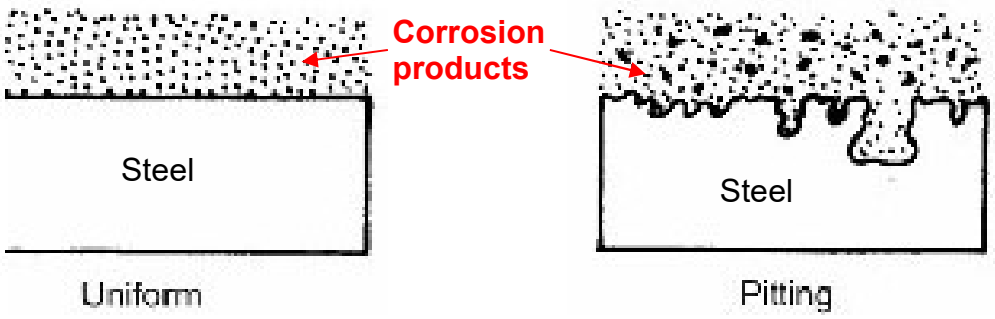

(a) Uniform corrosion attack (b) Pitting corrosion attack

Figure 5.3.1: Type of corrosion attacks
- Landolt (2007)

Uniform corrosion has an insignificant effect on the stress-strain relationship and is modelled simply by reducing the cross-sectional area of steel reinforcement (see RILEM Report 14). To simulate this behaviour, the remaining diameter, d_R, is given

by Equation 5.6

$$d_R = d_s\sqrt{1 - Q_{corr}} \qquad (5.6)$$

where:

d_R Remaining corroded reinforcement diameter (*mm*).

d_s Un-corroded reinforcement diameter (*mm*).

Q_{corr} Corrosion level (%).

The presence of pitting corrosion, however, may cause significant degradation of the mechanical properties due to the localised stress concentrations. Hence, the local pitting effect should be considered in the material properties. Kallias and Rafiq (2010) considered the same solution to simulate the effect of pitting corrosion in their FE analysis.

5.3.2. *Material properties of steel reinforcement in FE analysis*

All the uncorroded reinforcements were modelled with a standard elastic-ideally plastic material. The modulus of elasticity, E_s, and yield strength, f_s, were obtained from the steel tensile test. The hardening effect was not considered due to the current study being focused on the shear failure of RC T-beams. Shear failure is a sudden and brittle failure, so the post failure mode is out of research interest. It should also be noted that the maximum failure strain of steel shear links was 0.004, as demonstrated in Section 4.6. Such strain is within the range of the steel yield platform; hence, ignoring the steel hardening effect was acceptable. Similar reinforcement modelling technique was adopted by Dirar et al (2013) and Qapo et al (2014).

The corroded reinforcements were modelled with a standard elastic-ideally plastic material. The effect of mechanical properties was mainly due to pitting corrosion. Pitting corrosion may cause significant degradation of the mechanical properties due to localised stress concentrations. Several researchers, including Cairns et al. (2005) and Du et al. (2005), have studied this behaviour. Du et al. (2005) proposed a formula to predict the corrosion level, Q_{corr}, based on Faraday's law (see Equation 5.7). The tensile strength of corroded reinforcement, f_{corr}, can be determined by Equation 5.8.

$$Q_{corr} = 0.0145 \frac{I_{corr}}{d_s} t \qquad (5.7)$$

where:

Q_{corr} Corrosion level (%).

I_{corr} Applied corrosion current density (A/mm^2).

d_s Original reinforcement diameter (mm).

t Time elapsed since the initiation of corrosion (s).

$$f_{corr} = (1.0 - \beta Q_{corr}) f_s \qquad (5.8)$$

where:

f_{corr} Tensile strength of corroded reinforcement (N/mm^2).

β Strength factor = 0.0048.

Q_{corr} Corrosion level (%).

f_s Tensile strength of un-corroded reinforcement (N/mm^2).

It should be noted that a limited number of tensile tests were carried out in the

experimental test because of some parts of the bend and the heavily corroded reinforcements were not suitable for testing. Therefore, using such results of tensile testing will lead to inaccurate estimates in the FE analysis. The theoretical corrosion level, which was calculated by Equation (5.7), was also much higher than the actual corrosion level. This is due to the newly formed rust layer which will slow down the corrosion progress: however, the theoretical formula cannot capture this behaviour. Hence, only the actual corrosion level, Q_{corr}, was used. The tensile strength of corroded shear links was then estimated by Equation 5.8.

5.3.3. *Bond-slip behaviour of shear link-to-concrete interface*

The steel reinforcement was modelled by the embedded reinforcement elements. Perfect bonding behaviour (also known as tie-node model) was assumed to all the reinforcements which were coated with aluminium pigmented epoxy. Hence, no slip was allowed between the concrete and reinforcement in the FE simulation.

For the corroded shear links within the test span, the higher the corrosion level, the more corrosion products form (normally as unhydrated ferric oxide, Fe_2O_3). Unhydrated ferric oxide, Fe_2O_3, has a volume of about twice that of the steel. It will replace the steel when fully dense. Hence, the unhydrated ferric oxide, Fe_2O_3, initially increased the bond strength of the concrete-to-steel interface before corrosion cracks form due to the expansive force. Eventually the steel will be debonded from the concrete and corrosion induced cracks form. Therefore, a bond-slip model should be considered to simulate this behaviour.

Harajli et al. (2004) proposed three bond-slip models for uncorroded steel

reinforcement. An illustrated diagram of these models is given in Figure 5.3.2. The bond-slip model of the envelope for the pull-out failure model was used in the FE simulation. Equation 5.9 to Equation 5.14 shows the behaviour of the envelope for the pull-out failure numerically.

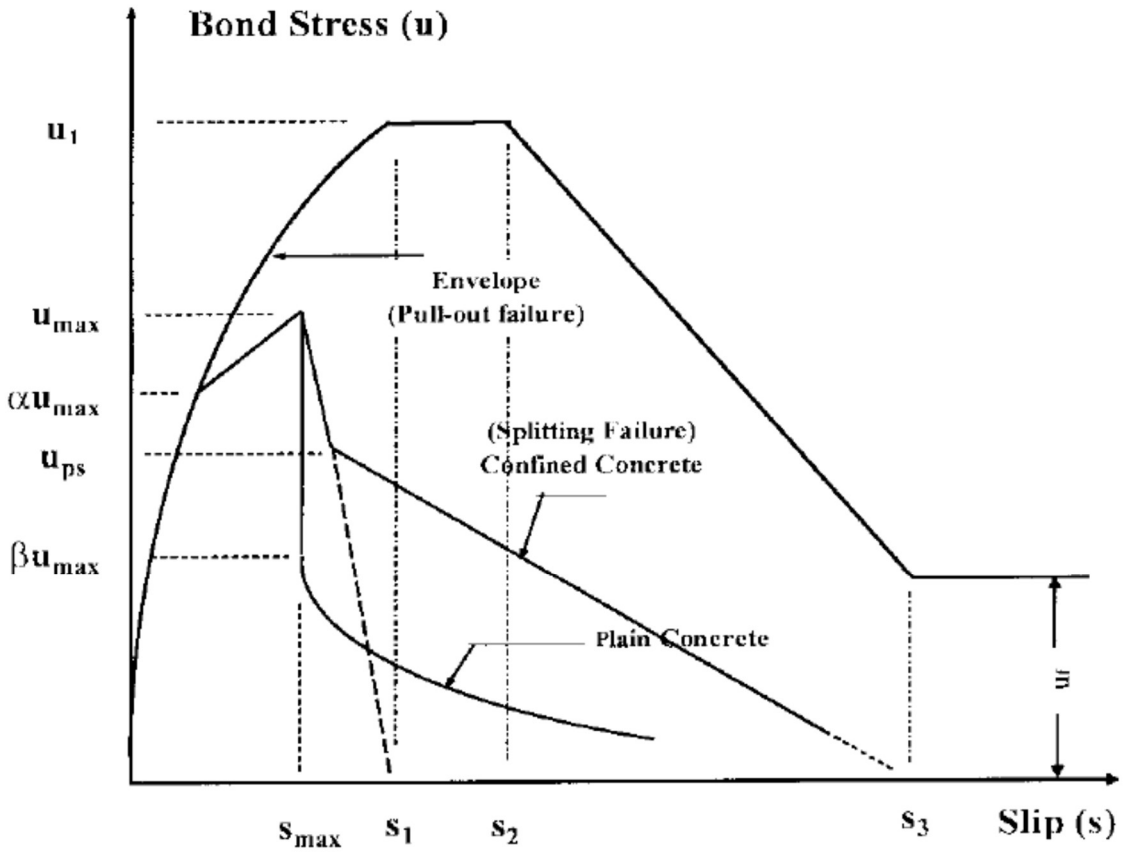

Figure 5.3.2: Bond-slip model for uncorroded steel reinforcement - Harajli et al. (2004)

$$u(s) = \begin{cases} u_1 \left(\frac{s}{s_1}\right)^{0.3}, & 0 < s \leq s_1 \\ 2.57\sqrt{f_{cy}}, & s_1 < s \leq s_2 \\ \left[u_1 + (u_1 - u_f)\left(\frac{s - s_2}{s_2 - s_3}\right)\right], & s_2 < s \leq s_3 \\ 0.35u_1, & s_3 < s \end{cases} \quad (5.9)$$

where:

$$u_1 = 2.57\sqrt{f_c'} \quad (5.10)$$

$$s_1 = 0.15c_0 \quad (5.11)$$

$$u_f = 0.35u_1 \quad (5.12)$$

$$s_2 = 0.35c_0 \quad (5.13)$$

$$s_3 = c_0 \quad (5.14)$$

$u(s)$ Bond stress at slip = s (*N/mm²*).

u_1 Maximum concrete pull-out failure stress (*N/mm²*).

f_{cy} Concrete cylinder compressive strength (*N/mm²*).

s Slip between steel and concrete (*mm*).

s_1 Variables that depend on bond conditions (*mm*).

c_0 Clear distance between the ribs of the reinforcement (*mm*).

u_f Ultimate failure bond slip stress (*N/mm²*).

s_2 Variables that depend on bond conditions (*mm*).

s_3 Variables that depend on bond conditions (*mm*).

Saifullah and Clark (1994) proposed a corrosion impact factor (also known as 'empirical factor'), *R*, to present the effect of corrosion on the bond-slip relationship between concrete and reinforcement. This factor initially increases to represent the increase in the bond strength due to the forming of rust (before the concrete cracks). It then decreases (after the concrete cracks) once a certain corrosion level is reached, as de-bonding and crack propagation take place. The proposed factor applies directly to the Harajli et al. (2004) bond strength model (see Equations 5.15 to 5.20 for details). It should be noted that the corrosion impact factor was adjusted to find a best fit shear force-deflection curve for each of the tested beams. The same value was then adopted to simulate the corresponding RC T-beam in the parametric

study.

$$u(s) = \begin{cases} u_1 R \left(\frac{s}{s_1}\right)^{0.3}, & 0 < s \leq s_1 \\ 2.57R\sqrt{f_{cy}}, & s_1 < s \leq s_2 \\ R\left[u_1 + (u_1 - u_f)\left(\frac{s - s_2}{s_2 - s_3}\right)\right], & s_2 < s \leq s_3 \\ 0.35Ru_1, & s_3 < s \end{cases} \quad (5.15)$$

where:

$$u_1 = 2.57\sqrt{f_c'} \quad (5.16)$$

$$s_1 = 0.15c_0 \quad (5.17)$$

$$u_f = 0.35u_1 \quad (5.18)$$

$$s_2 = 0.35c_0 \quad (5.19)$$

$$s_3 = c_0 \quad (5.20)$$

$u(s)$ Bond stress at slip = s (*N/mm²*).

u_1 Maximum concrete pull-out failure stress (*N/mm²*).

f_{cy} Concrete cylinder compressive strength (*N/mm²*).

R Corrosion empirical factor.

s Slip between steel and concrete (*mm*).

s_1 Variables that depend on bond conditions (*mm*).

c_0 Clear distance between the ribs of the reinforcement (*mm*).

u_f Ultimate failure bond slip stress (*N/mm²*).

s_2 Variables that depend on bond conditions (*mm*).

s_3 Variables that depend on bond conditions (*mm*).

The bond slip model of Harajli et al. (2004), with the Saifullah and Clark (1993) proposed empirical factor = 1.0, was compared with the perfect bond model (also

known as the tie-node model) on the test beam of N00. Figure 5.3.3 shows the N00 shear force-deflection curves of the experimental result, the FE models with perfect bond model and the bond slip model of steel-to-concrete interface. It shows that the bond slip model of Harajli et al. (2004), with the Saifullah and Clark (1993) proposed empirical factor, was more comparable to the experimental result.

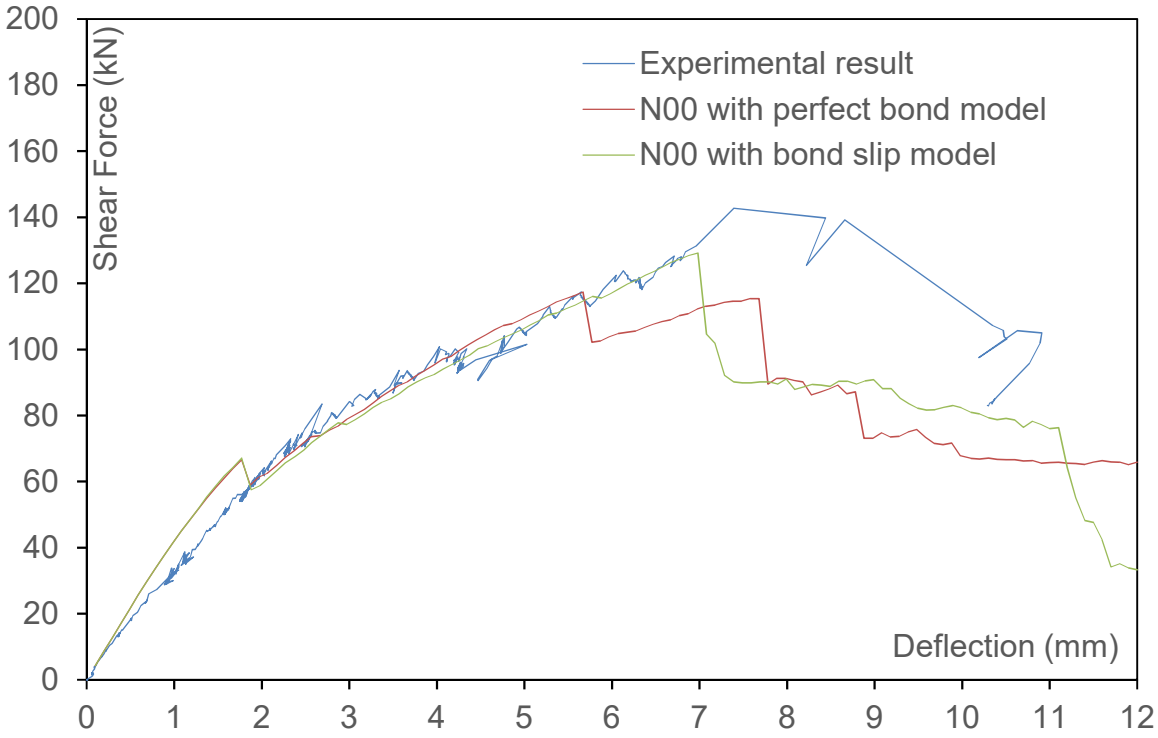

Figure 5.3.3: Effect of bond-slip models on the shear force-deflection curves for Beam N00

5.3.4. *Summary of the steel reinforcement modelling*

The steel reinforcement was modelled with embedded reinforcement elements. The interface of uncorroded steel-to-concrete was assumed as a perfect-bond. The cross section area and yield strength of the uncorroded steel reinforcement were obtained from the experimental test. As the longitudinal reinforcement was considered to be perfectly bonded at the interface of steel-to-concrete, the end anchorage plates were

not simulated in the FE models.

The corroded reinforcement was simulated by considering the effects of uniform corrosion and pitting corrosion. A reduced diameter was calculated from the actual corrosion level to simulate the uniform corrosion. An adjustment in the reinforcement yield strength was adopted to simulate the pitting corrosion effect, based on Du et al. (2005). Saifullah and Clark (1994) proposed a corrosion impact factor, accompanied by the Harajli et al (2004) proposed bond-slip model, which were integrated into the test-span shear links to simulate the bond-slip behaviour of shear link-to-concrete interfaces.

5.4. Modelling of CFRP composites

Two types of CFRP composites were simulated in the FE models. In this section, the modelling concept of CFRP composites is illustrated.

5.4.1. *Deep embedded CFRP rods*

The DE CFRP rods were modelled in a similar fashion to the steel reinforcement, by using the embedded reinforcement element. The DE CFRP rods have a centre-to-centre spacing of 275 *mm* at the test span. The total embedded length of the rod was 360 *mm,* with 100 *mm* and 260 *mm* in the concrete flange and web respectively. For details refer to Figure 5.4.1.

The physical and mechanical properties of the DE CFRP rods were taken from the manufacturer's data sheet (see Section 3.3.3 for details). Only half of the cross section area was required as the rods were modelled at the symmetrical face.

The embedded reinforcement element allows the material to be modelled as an elastic-plastic material. However, CFRP rods are brittle materials. Hence, the predicted CFRP strain at failure should be compared with its limiting strain (0.0175). If the strain of CFRP rods exceeds the limiting strain, the fracture of the CFRP rods takes place.

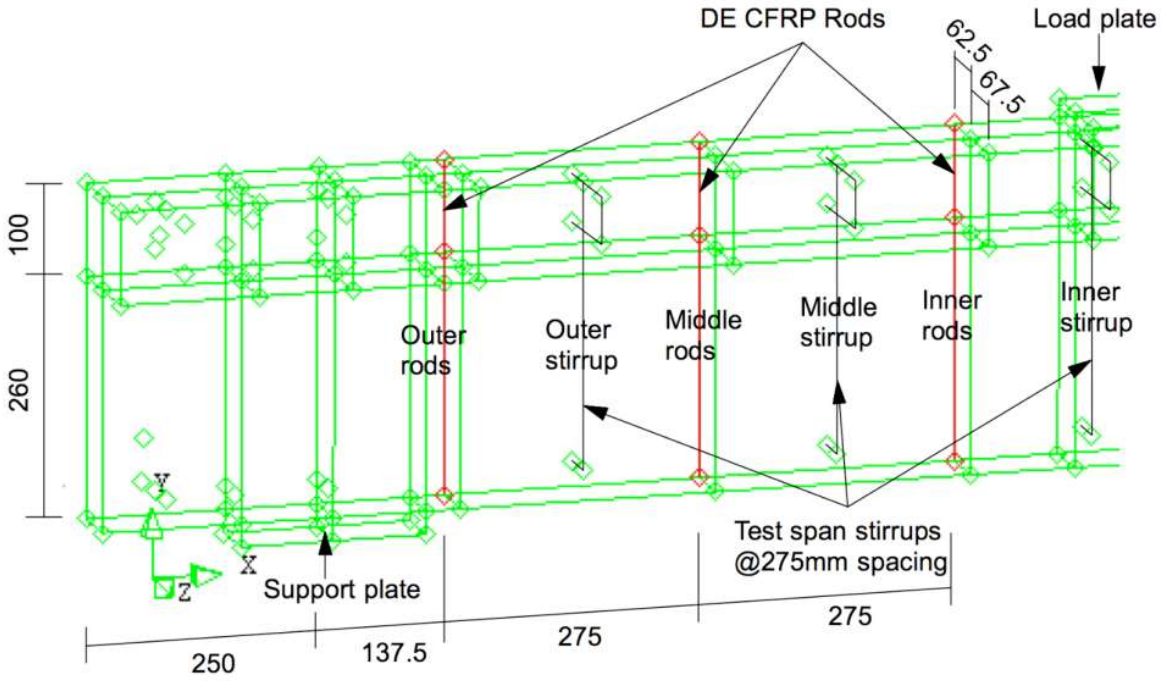

Figure 5.4.1: Typical FE model for DE CFRP-strengthened beams - dimensions in *mm*

5.4.2. *Externally bonded CFRP sheets*

It should be noted that the externally bonded CFRP sheet has been well studied. CFRP sheets are normally simulated with plate elements, especially for bidirectional CFRP sheets. However, the CFRP sheet used in this experimental test was a unidirectional sheet. Therefore, two-node truss elements offer an easier solution in FE analysis. Dirar et al. (2013) successfully studied the nonlinear behaviour of pre-cracked RC T-beams repaired in shear with CFRP sheets, where the unidirectional

EB CFRP sheets were simulated with two-node truss elements. Hence, the unidirectional CFRP sheet was also modelled as a two-node truss element in this research. The spacing of the EB CFRP sheet element was 30 *mm* centre-to-centre across the test span, from the edge of the supporting plate to the centre of the loading plate (see Figure 5.4.2). All elements have a uniform cross section area equal to the centre-to-centre distance of the truss element multiplied by the thickness of the CFRP sheet: 30 *mm* (width) x 1 *mm* (thickness) = 30 mm^2. The CFRP sheet was modelled as an elastic brittle material. The modulus of elasticity and strength were taken from the manufacturer's data sheet, as specified in Section 3.3.4.

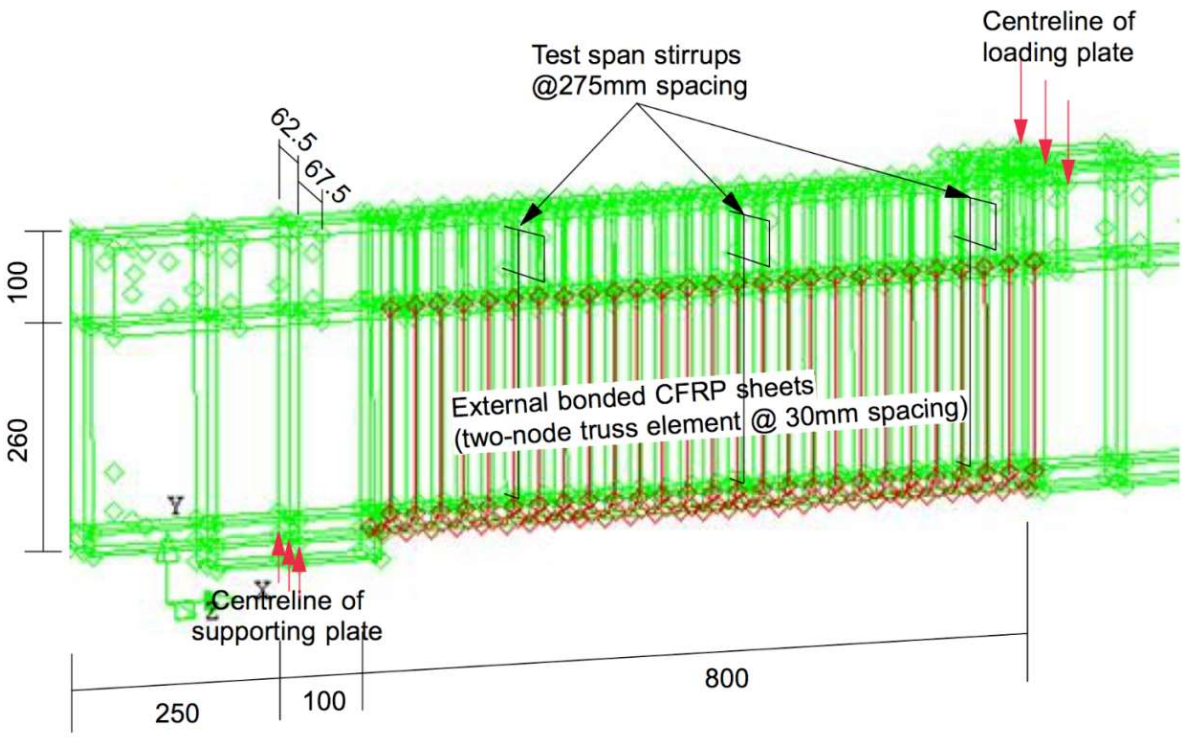

Figure 5.4.2: Typical FE model for EB CFRP-strengthened beams
- dimensions in *mm*

5.4.3. *CFRP-to-concrete Interface*

Bond-slip behaviour of CFRP composite-to-concrete interfaces is reviewed in this

section. The DE CFRP rod is a newly developed retrofitting technique to enhance the capacity of the existing RC structure. Limited research has been carried out on the bond behaviour of DE CFRP rod-to-concrete interfaces. Godat et al. (2012) compared two bond-slip models which were named as Eligehausen, Popov, and Bertero (BPE), and Cosenza, Manfredi, and Realfonzon (CMR). Godat et al. (2012) modified the BPE model and the CMR model with new curve-fitting parameters to simulate the FRP rod-to-concrete interfacial behaviour. The CMR model showed a good agreement with his experimental result. Hence, the CMR model was reviewed. The CMR model is given by Equation 5.21.

$$\frac{\tau}{\tau_m} = \left(1 - e^{-\frac{s}{s_r}}\right)^{\beta} \tag{5.21}$$

where:

τ Slip stress (*N/mm²*).

τ_m Maximum slip stress (*N/mm²*).

s Slip distance (*mm*).

s_r Parameter (0.028 for sand-coated rods)

β Parameter (0.33 for sand-coated rods)

It should be noted that the suggested values of s_r and β are only suitable for Godat et al. (2012). The CMR model is more close to the actual behaviour of the interaction between the DE CFRP rod and concrete. When comparing the simulation results of B00 with the CMR model and the perfect bond model, the CMR model did not give a better prediction due to the sensitivity of the parameters. Therefore, the perfect-bond model was used for the interface behaviour of the DE CFRP rod-to-concrete.

For the EB CFRP sheets, the interfaces of EB CFRP sheet-to-concrete were modelled with eight-node bond-slip interface elements. The bi-linear bond-slip models, which were developed by Sato and Vecchio (2003) and Lu et al. (2005), were compared. Both models assumed that bond failure occurs within a thin layer of concrete adjacent to the interface of adhesive-to-concrete, because the adhesive is usually stronger than the concrete. Hence, the bond-slip model simulates the overall behaviour of the CFRP sheet-to-concrete interface, rather than the adhesive material. Equations 5.22 to 5.25 show the Sato and Vecchio (2003) model while Equations 5.26 to 5.31 show the Lu et al. (2005) model.

Proposed bi-linear bond-slip model by Sato and Vecchio (2003):

$$\tau_{max} = (54f'_c)^{0.19} \quad (5.22)$$

$$s_0 = 0.057\sqrt{G_{f,i}} \quad (5.23)$$

$$s_u = \frac{2G_{f,i}}{\tau_{max}} \quad (5.24)$$

$$G_{f,i} = \left(\frac{\tau_{max}}{6.6}\right)^2 \quad (5.25)$$

where:

τ_{max} The peak bond stress (*N/mm²*).

f'_c Concrete compressive strength (*N/mm²*).

s_0 Slip corresponding to the peak bond stress (*mm*).

s_u Ultimate slip

$G_{f,i}$ Interfacial fracture energy

Proposed bi-linear bond-slip model by Lu et al. (2005):

$$\tau = \begin{cases} \tau_{max}\dfrac{s}{s_0} & if\ s \le s_0 \\ \tau_{max}\dfrac{s_{max}-s}{s_{max}-s_0} & if\ s_0 < s \le s_{max} \end{cases} \quad (5.26)$$

$$\beta_{\mathrm{w}} = \sqrt{\frac{2.25 - b_f/b_c}{1.25 + b_f/b_c}} \quad (5.27)$$

$$s_{max} = \frac{2G_{f,int}}{\tau_{max}} \quad (5.28)$$

$$G_{f,int} = 0.308\beta_w^2\sqrt{f_t} \quad (5.29)$$

$$s_0 = 0.0195\beta_w f_t \quad (5.30)$$

$$\tau_{max} = 1.5\beta_w f_t \quad (5.31)$$

where:

τ_{max}	The peak bond stress (*N/mm²*).
f_t	Concrete tensile strength (*N/mm²*).
s_0	Slip corresponding to the peak bond stress (*mm*).
s_{max}	Ultimate slip (*mm*).
$G_{f,i}$	Interfacial fracture energy.
b_{f}	Width of CFRP sheets (*mm*).
b_{c}	Width of concrete (*mm*).
β_{w}	Width factor

As depicted in the linear equations, the bond stress-slip relationship is linear up to the peak bond stress. Debonding initiates if the slip exceeds the limiting value, the slip value corresponding to the peak bond stress. The debonding process is modelled by a linear softening function, which relates the ultimate slip to the interfacial fracture energy. Complete debonding occurs when the slip value exceeds

maximum slip. In this research, the Sato and Vecchio (2003) model was adopted as it gave a better agreement in the FE predictions with the experimental result, as validated in Section 5.6.

5.5. Solution procedure

To achieve convergence in the analysis of failure load, an incremental iterative procedure was adopted by using the vertical displacement increments of 0.1 *mm* for 120 steps. The Quasi-Newton iteration method (or Secant iteration method) was employed, together with a displacement-based convergence criterion, to achieve equilibrium at the end of each increment. Similar procedures were adopted by Qapo et al. (2014).

Based on Hee and Jefferson (2008) and Dirar et al. (2013), a displacement norm value of 0.001 was adopted to specify convergence. A maximum of 10,000 iterations was allowed at each step before termination of the analysis due to non-convergence. This strategy proved successful, as convergence was achieved at every load step for the unstrengthened and DE strengthened FE models. More iteration steps were required for the EB strengthened FE models, particularly in the corroded models. Dirar et al. (2013) mentioned that it could have been possible to use a variable incremental solution procedure (Chen et al. 2011, 2012) to achieve convergence with less iteration steps. However, the employed solution strategy was relatively accepted as the main aim was predicting the structural behaviour up to and including peak loads, rather than predicting the complete post-peak behaviour. It should be noted that the FE program allows the user to define the terminated criteria if non-convergence is found in the analysis. The output reports showed that convergence

was met at each load analysis step.

5.6. Validation of proposed FE model

In this section, the results of a comparative study between the numerical approach using finite element analysis and the laboratory tests are presented. The comparative study was undertaken to determine the validity of the finite element analysis in predicting the nonlinear behaviour of the corroded RC T-beam repaired with CFRP composites. Shear force capacity, shear force-deflection curves and failure crack patterns are compared in Sections 5.6.1, 5.6.2 and 5.6.3 respectively. With the aid of tables, graphs and diagrams, the results of the comparative study between FE models and experiment tests are presented.

5.6.1. *Shear capacity*

The experimental results of shear capacity, V_{exp}, and the FE-predicted values, V_{rot}, are given in Table 5.6.1. The FE predicted shear capacity is the maximum shear force in the test span. It can be calculated as a sum of test span reactions. The FE predictions were in good agreement with the experimental results. The proposed FE model underestimates shear capacity, with a mean experimental/predicted ratio of 1.17 and a standard deviation of 0.06. This is to be expected since the rotating crack model assumes that the crack planes are always principal planes and hence, underestimates the amount of shear stress transferred across the cracks. Similar results were reported by Dirar et al. (2012).

The un-strengthened beam showed a gradual increase in the experimental/prediction ratio, V_{exp}/V_{rot}, as the corrosion level increased. This may be due to three reasons:

the underestimation of the bond stress in the adopted corrosion rate related bond-slip model at the shear link-to-concrete interfaces, the underestimation of the yield strength of the corroded reinforcements, and the overestimation of the steel reinforcement degradation model. However, a standard deviation of 0.02 showed the consistency in the prediction, with an acceptable mean V_{exp}/V_{rot} of 1.12. The FE predictions were expected to be lower than the experimental result because of the rotational smeared crack model.

Table 5.6.1: Comparison between experiment and FE-predicted shear force capacity results

Specimen	Experimental result of shear capacity, V_{exp} (kN)	FE predicted shear capacity, V_{rot} (kN)	V_{exp}/V_{rot} ratio	Average (V_{exp}/V_{rot})	Standard deviation
N00	143	129	1.10	1.12	0.02
N07	148	133	1.11		
N15	156	136	1.15		
B00	142	127	1.12	1.13[a]	0.02[a]
B07	182	141	1.29		
B15	164	144	1.14		
S00	182	148	1.23	1.19	0.05
S07	174	144	1.21		
S15	174	154	1.13		

[a] The predictions of the rotating crack model for B07 is excluded due to higher V_{exp}/V_{rot}.

For the DE strengthened specimens, B00 and B15 showed the predicted shear force capacities with a mean V_{exp}/V_{rot} of 1.13 and a standard deviation of 0.02. It should be noted that the prediction of B07 was not included in calculating the average ratio and standard deviation, due to errors in the FE predictions. It might be caused by the low

corrosion level that does not introduce corrosion cracking but enhances the concrete strength of the test beam. However, the FE simulation cannot capture this behaviour. With the low standard deviation and an average ratio of 1.13, the modelling concept of the DE CFRP rod strengthened models was acceptable. Due to the erroneous prediction of B07, the proposed model for Beam B07 was not considered in the parametric study.

The EB strengthened specimens have a mean experimental/prediction ratio of 1.19 and a standard deviation of 0.05. The low standard deviation showed the consistency of the predictions. However, the mean experimental/predicted ratio of EB strengthened specimens was relatively higher than the mean experimental/prediction ratio of the unstrengthened and DE strengthened beams. The results showed that the FE predictions were improving with the increase of the corrosion level. This contradicts the case of the unstrengthened beams, where the FE predictions became less accurate with increasing corrosion levels. It might be explained by corrosion development, where expansive forces acted on the concrete which was also constrained by the CFRP sheet: thus, concrete strength will be enhanced gradually. Alternatively, it seems that the CFRP sheet-to-concrete bond-slip model underestimated the stress transfer between the two materials, especially in the cases of S00 and S07.

5.6.2. *Shear force-deflection curves*

Figure 5.6.1 to Figure 5.6.3 present shear force-deflection curves for the results of experimental tests and FE predictions. It should be noted that the ‘stiffness’ discussed in this section refers to the ratio of maximum shear force, V_{max}, to the

deflection at the bottom of the FE beams along the centre line of the loading point. These curves are referenced in the format “AXX YYY”, where ‘A’ denotes the strengthening scheme, ‘XX’ indicates the target corrosion level and ‘YYY’ identifies whether the result is an experimental result or an FE prediction. For example, “N15 FEA” means the curve represents the FE result of 15% corrosion level for an unstrengthened beam.

In general, the stiffness of the FE model was greater than experimental results before the crack forms, and then, it was the same, or lower, than experimental results until failure. It should be noted that the 15% corroded FE models have the highest stiffness in the same strengthening scheme model. This can be explained by the different concrete compressive strengths used in the model, combined with the following factors:

1. The ignorance of the micro-cracking (cracks due to creep and shrinkage and accelerated corrosion process),
2. The assumption of perfect bond in some interfaces,
3. The alleviation of stress concentration due to the smeared model, and
4. Noise due to crack opening.

The shear force-deflection curves can be divided into two stages: loading up to crack formation stage and loading until failure stage. During the first stage, the stiffness of the proposed model was generally higher than the experimental results. Cracks are normally formed after casting due to shrinkage. An increase in the applied shear force extends these discrete cracks and gradually forms a major crack. However, the model was simulated using the smeared crack method, which means that cracks due to shrinkage were not captured. Consequently, the stiffness of the FE model was

higher than the experimental tests before the initial tension crack appears in the model. It is more significant when comparing the corroded beams with uncorroded beams (see Figure 5.6.1). For this stage of the simulation, the discrete crack approach may be more realistic in modelling shear failure of concrete beams.

Comparing the inclinations of the experimental and predicted shear force-deflection curves, it can be seen that the FE models accurately predicted the stiffness of most of the beams and slightly underestimated the stiffness of Beams S07 and S15 at the second stage. This might be explained thus: as the surface of the concrete suffers to introduce new cracks, the stiffness of the beam will be reduced gradually as the existing loading cracks join with the corrosion induced concrete cracks.

Figure 5.6.2 and Figure 5.6.3 show shear force-deflection curves of DE strengthened beams and EB strengthened beams respectively. The higher stiffness of the DE strengthened FE model might be caused by the overestimation of the un-cracked stiffness, such as the concrete cover being considered as fully effective. In fact, the cover can either be ignored, or considered to have weaker material properties due to the surface cracks and for casting reasons. The other reason could be caused by the selected bond-slip model of the CFRP rod-to-concrete interfaces. However, the number of available CFRP rod-to-concrete interface bond-slip models is very limited. Hence, the interface behaviour should be further investigated in future research. For FE models of corroded and DE CFRP rod strengthened beams, the over-stiffness was higher than the unstrengthened FE models. These further prove that the perfect-bond model between CFRP rod-to-concrete interfaces may overestimate the bond behaviour.

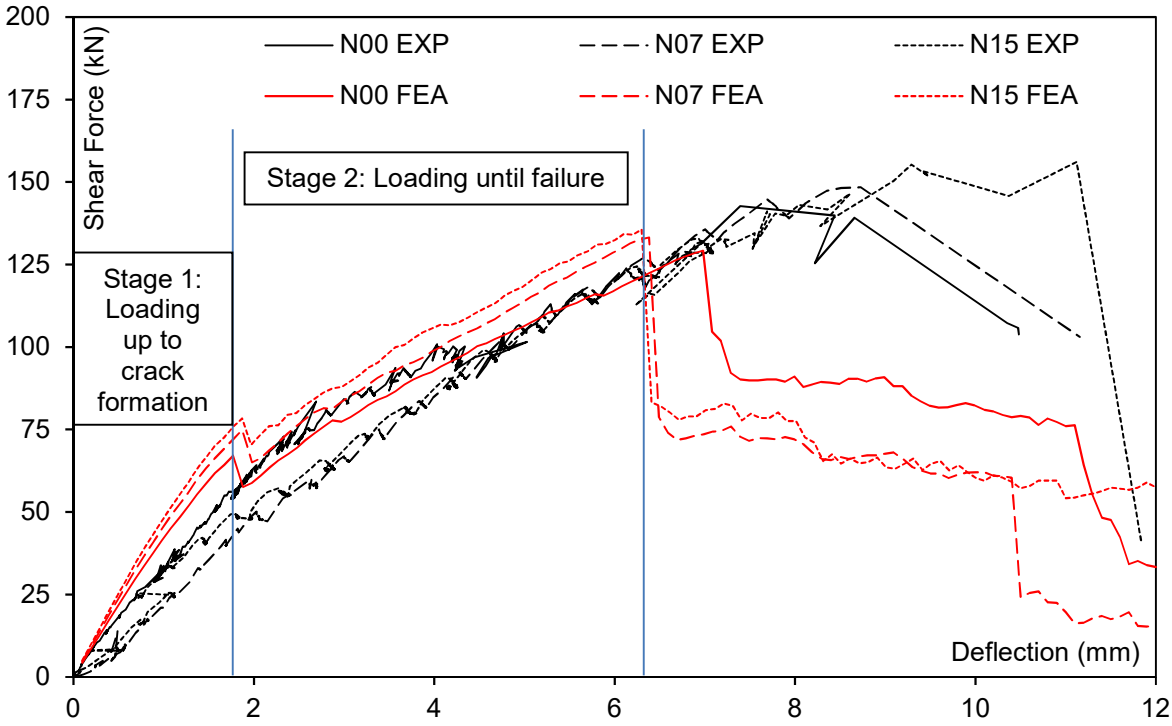

Figure 5.6.1: Shear force-deflection curves for unstrengthened beams

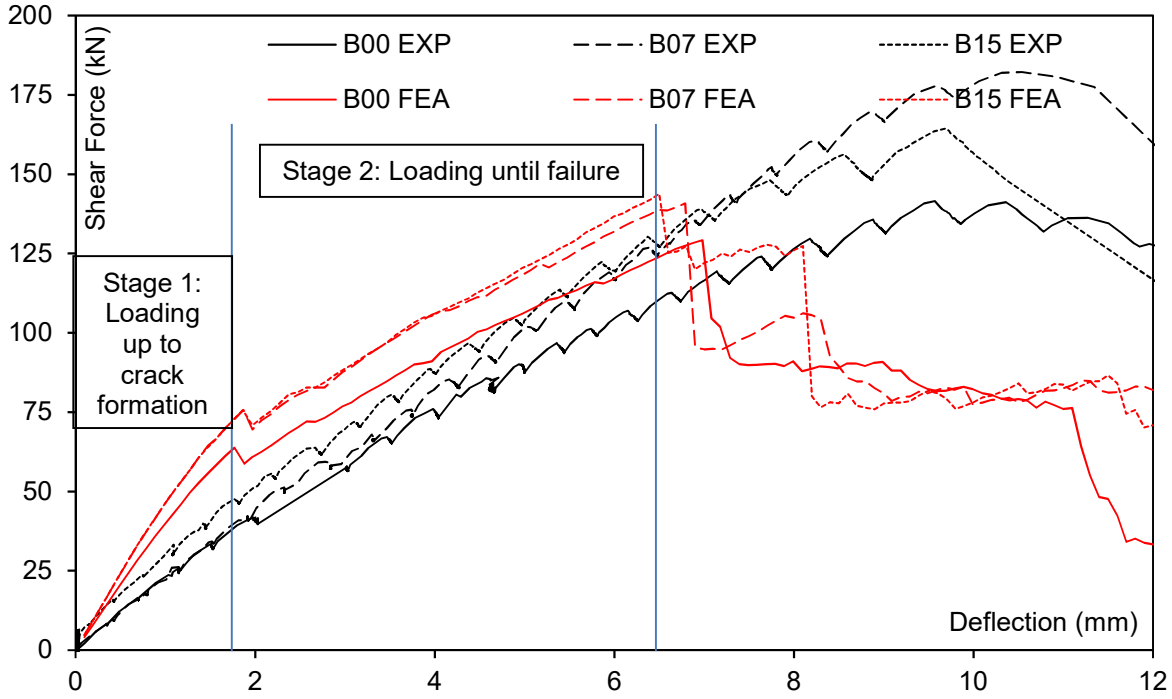

Figure 5.6.2: Shear force-deflection curves for DE strengthened beams

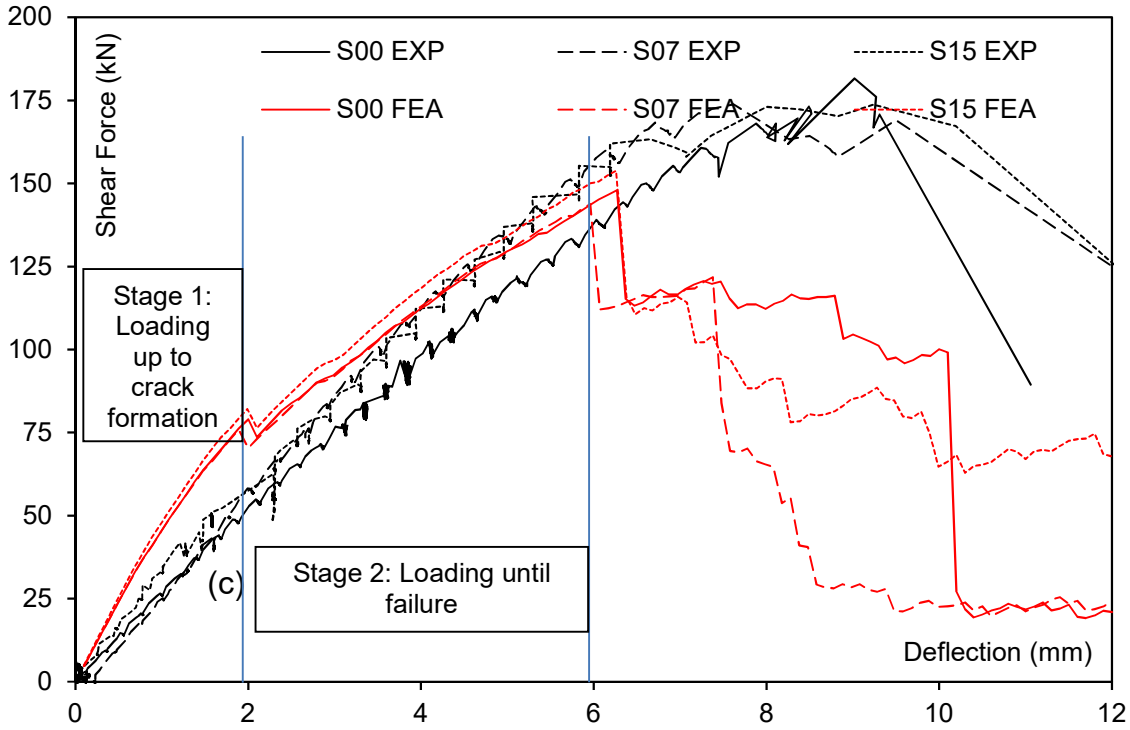

Figure 5.6.3: Shear force-deflection curves for EB strengthened beams

For models corroded and strengthened with EB CFRP sheets, the FE predictions showed that stiffness was less than experimental results at the second stage. The bond-slip model may have underestimated stress transfer, and consequently the strain in CFRP sheets. If that is the case, then the CFRP resistance to crack opening was underestimated as well, which might explain the lower predicted stiffness. Alternatively, it may be explained as the CFRP sheet (modelled as unidirectional) still carrying some load perpendicular to the fibre orientation; however, the truss element cannot simulate this effect.

5.6.3. *Predicted crack patterns*

A significant strength of using FE applications is their ability to show the development of cracks. It should be noted that only the test span was compared; the non-test was

considered as having less effect on the test span and is outside research interest. Figure 5.6.4 and Figure 5.6.5 show the comparison between the experimental and predicted concrete crack patterns at failure for the unstrengthened and DE strengthened beams respectively. The predicted crack pattern is presented by the contour plots of the principal tensile strain. It can be seen that the FE model adequately predicted the failure cracks of the unstrengthened and DE strengthened beams, and was due to a major diagonal crack that ran from the bearing plate up to the loading plate at the test span. It should be noted that the higher the strain value in the contour showed as the wider the crack.

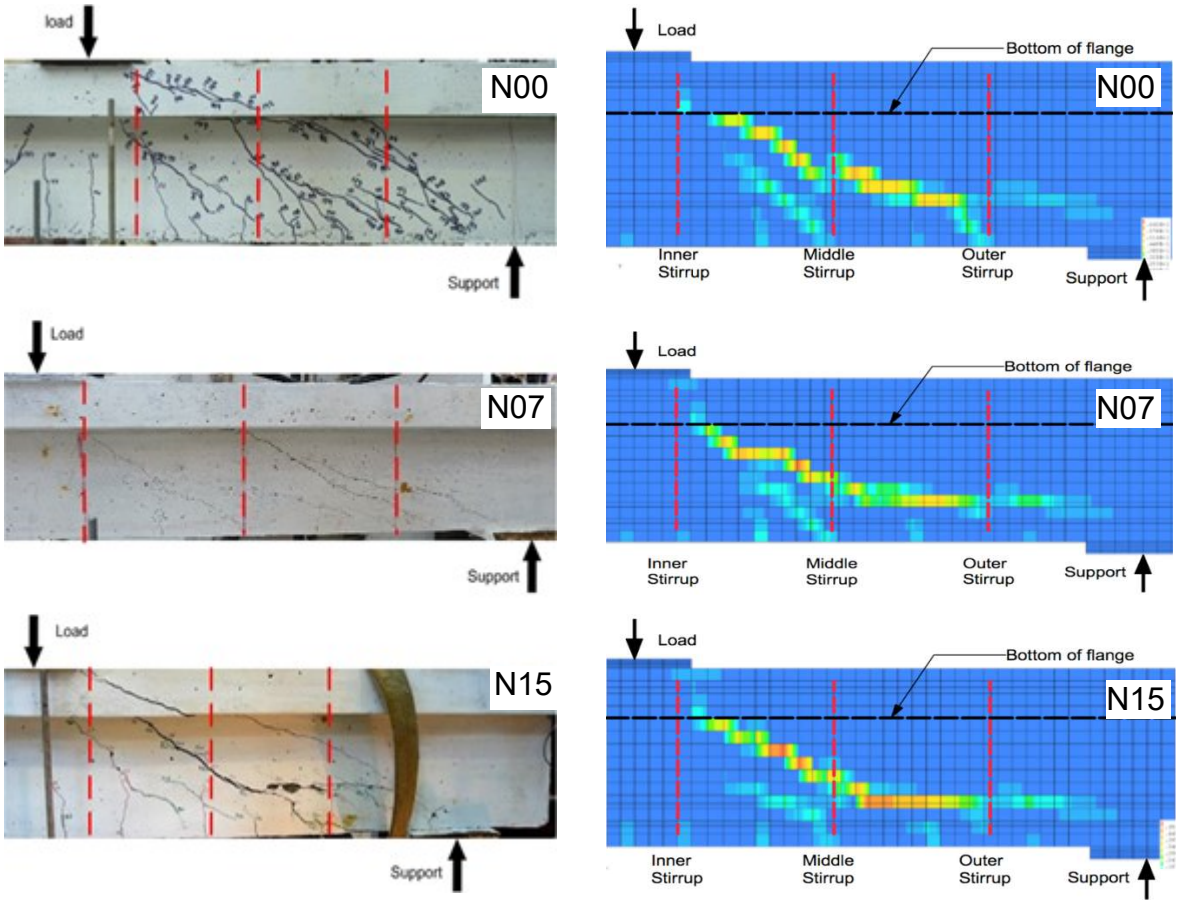

Figure 5.6.4: Predicted crack pattern for unstrengthened beams

The DE strengthened models showed more distributed diagonal cracks compared to

the unstrengthened models (see Figure 5.6.5). It was explained in Section 4.5 that increasing the transverse reinforcement ratio results in more distributed cracks. It should be noted that the predicted crack patterns seem slightly different to the experimental result of DE strengthened beams. This may be due to the heterogeneous nature of RC T-beams, but FE models cannot capture this behaviour. However, the differences were insignificant and the FE models predicted that the DE strengthened beams failed in shear.

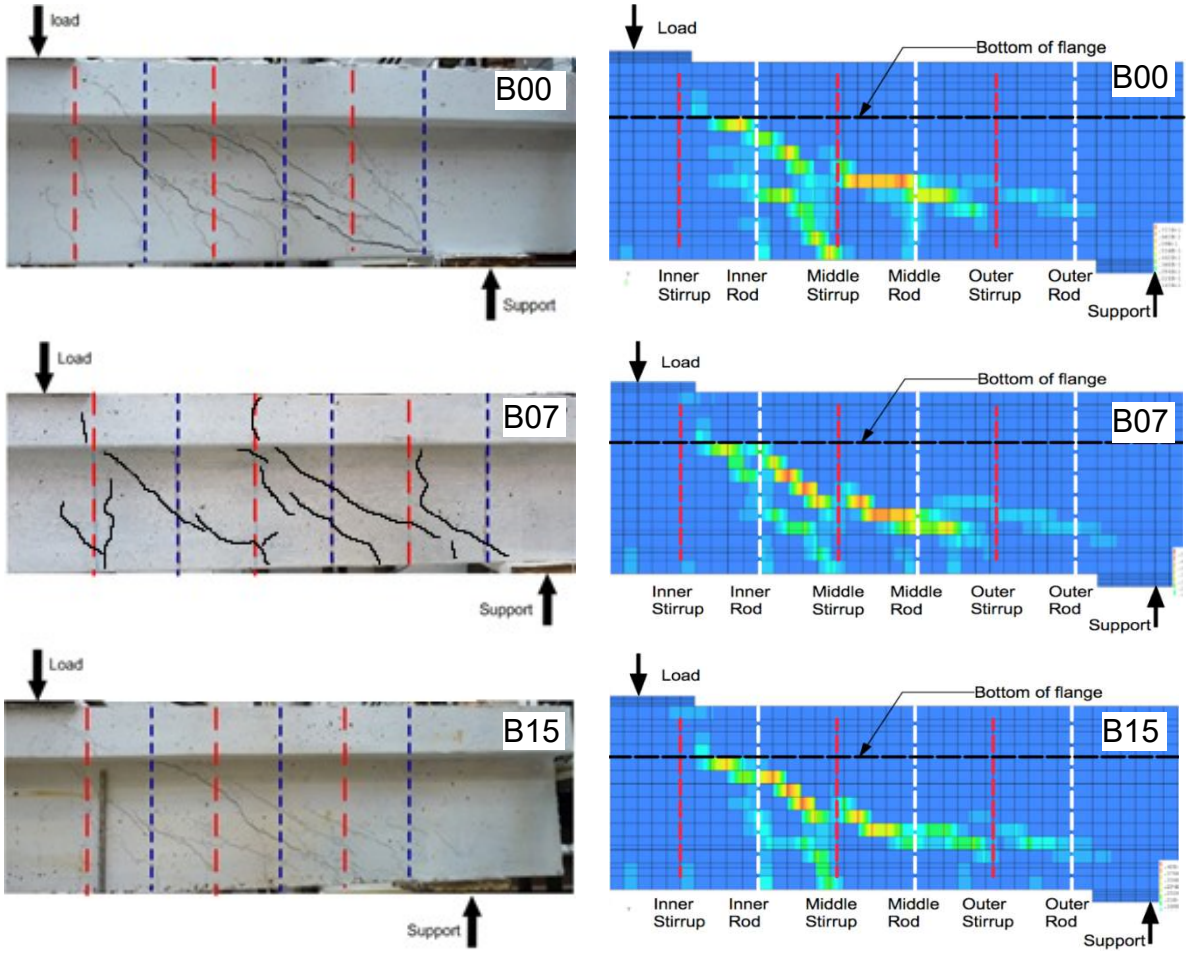

Figure 5.6.5: Predicted crack pattern for DE CFRP-strengthened beams

Figure 4.5.3 shows the typical experimental failure mode of the EB CFRP sheet strengthened beams. The web of concrete was fully wrapped with EB CFRP sheets,

so no crack can be observed except the debonding of the EB CFRP sheet at failure. However, Figure 5.6.6 presents the predicted concrete cracks of the FE model by using the principal tensile strain method. As shear force capacity and shear force-deflection curves of the EB strengthened beams were adequately simulated, the crack may be used to illustrate the development of concrete cracks in the EB strengthened beams.

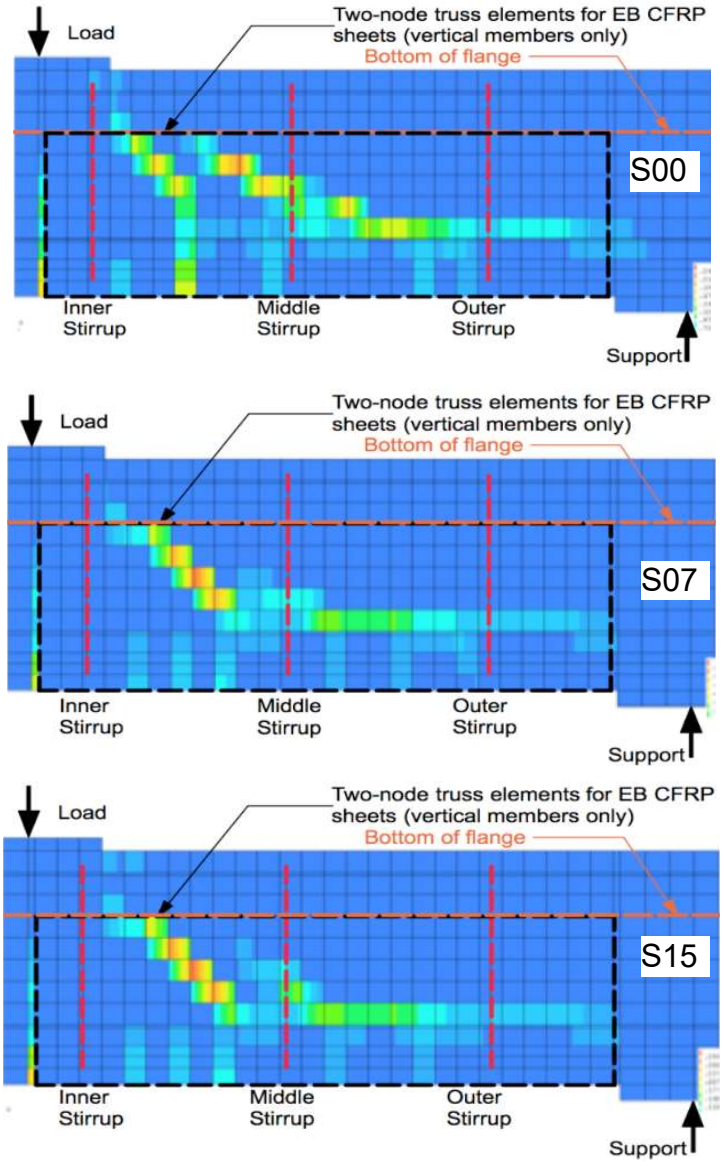

Figure 5.6.6: Predicted crack pattern for EB CFRP-strengthened beams

5.7. Summary

The aim of this chapter was to develop NLFE predictive tools capable of modelling the behaviour of experimental specimens. This chapter has reviewed the existing literature about the FE simulation of corroded RC T-beams repaired with CFRP composites. 3D nonlinear FE models of corroded and strengthened beams were developed. The FE models were validated using the experimental results.

The FE model simulated the concrete with six-node solid wedge elements, the steel reinforcement and DE CFRP rods with embedded reinforcement elements, and the EB CFRP sheets with two-node truss elements. The bond-slip interfaces between stirrup-to-concrete and CFRP sheet-to-concrete were adequately simulated. The adopted geometrical and material properties were either obtained from the experimental tests or calculated based on well-used models. The solution procedure used was described in Section 5.5.

Shear behaviour was verified by comparing the predicted shear force capacity, shear force-deflection curves and crack patterns to the experimental results. The other behaviours were not considered, such as strain in reinforcement and CFRP composites. Although the strain in the reinforcement and CFRP composites were recorded by strain gauges and FBG sensors, the use of the rotating smeared crack concept, and sensitivity of the location of strain gauge, led to the comparison of strain between experimental results and FE predictions being unreliable.

Based on the comparative results between numerical predictions and experimental results, the following conclusions were drawn.

1. Shear force capacity predictions were in fair agreement with the experimental

results. The mean experimental/predicted capacity ratios achieved by the rotating crack model were 1.12, 1.13 and 1.19, and the standard deviations were 0.02, 0.02, and 0.05 for unstrengthened, DE strengthened and EB strengthened beams respectively.

2. The shear force-deflection curves showed that the stiffness of the FE model was generally higher than the experimental result before the concrete crack forms. Once the crack forms, the stiffness was comparable between the FE predictions and experimental results, because of the rotational smeared crack model of concrete.
3. The numerical prediction of crack patterns showed that all of the beams were characterised by shear failure, which were compatible with the shear failure of test beams.
4. The predicted crack patterns have a good alignment with the crack patterns observed in the experimental tests.

CHAPTER 6: REVIEW OF TECHNICAL REPORT 55 AND PARAMETRIC STUDY

6.1. Introduction

The aim of this chapter is to compare the TR-55 predicted DE CFRP shear contributions to the predictions of NLFE models and experimental results. In order to achieve this goal, the objectives were as follows:

1. *To identify the critical parameters on the shear performance of uncorroded RC T-beams strengthened with DE CFRP rods*
2. *To compare the results of experimental tests, numerical models and predictions of TR-55.*

Section 6.2 reviews the latest version of TR-55 (2012) with amendment No.1, which was published in October 2013. The calculated CFRP contributions are also compared with selected experimental results.

Section 6.3 presents the results of the parametric study. The EB CFRP sheet strengthened FE models were excluded from the parametric study due to the relatively high experimental-to-predicted shear resistance ratio (1.19); furthermore, this has been well studied in the past. Only the DE CFRP rod strengthened beams were used in the parametric study.

Sections 6.3.1, 6.3.2, 6.3.3 and 6.3.4 investigate the effect of bond-slip model of corroded shear links, concrete cube compressive strength, steel-to-CFRP shear reinforcement ratio and shear span-to-effective depth ratio. A total of eighteen FE models was used to investigate the effects of the above parameters on the shear

strength of RC T-beams strengthened with DE CFRP rods.

Section 6.4 compares the results of TR-55 (2012) with the predictions of the FE models, as well as experimental results. Finally, Section 6.5 comments on the accuracy of TR-55 predictions and summarises the key findings of the parametric study.

6.2. Review of Concrete Society Technical Report 55 (2012)

A number of design guidelines for concrete shear strengthening using Fibre Reinforced Polymer (FRP) reinforcement have been developed around the world. In the UK, the Concrete Society Technical Report 55 (TR-55) is the first, and currently the sole, standard document to give guidance on the design of FRP shear strengthening systems. The first edition of TR-55 was published in 2000. In the light of this guidance document and ongoing research, a second edition of TR-55 was published in 2004. Materials and techniques were developing, as is the range of applications. Hence, it was necessary to update the guidance and publish the third edition of TR-55 in 2012, which was followed by amendment No. 1, added in October 2013.

As mentioned in Section 2.4.6, TR-55 (2012) recommends that the shear contribution of internal steel shear reinforcement should be calculated according to Clause 6.2.3 of BS EN 1992-1-1. It also recommends a design model to estimate the shear contribution of FRP shear reinforcement in order to determine the overall shear capacity of an RC section. This approach can be presented numerically by Equation 2.26 for deep embedded FRP strengthened sections. It should be noted that the FRP

contribution is determined by adopting the truss analogy, and assuming the inclination angle of the shear cracks to be 45° in TR-55 (2012).

As the DE CFRP rods are bonded to the concrete using adhesives, there is an effective anchorage length beyond which no increase in resistance can be achieved. This anchorage length is calculated by Equation 2.29. The effective width over which the deep embedment rods will act should be calculated based on the effective anchorage length. For short anchorage lengths, the force which can be generated in the rod is low and can conservatively be neglected.

It should be noted that all safety factors were set equal to 1.00 for comparison purposes in this study. Dirar et al. (2012) commented that the predicted shear force has not been compared to the total experimental shear force because such a comparison can lead to erroneous conclusions. Such a comparison also requires the use of conventional design codes, such as BS EN 1992-1-1 to calculate the steel contribution to total shear capacity. BS EN 1992-1-1 often gives inaccurate predictions for steel contribution to total shear force, because it assumes that only shear reinforcement will contribute to shear force resistance of a section. For example, the total predicted shear force resistance of Beam N00 using the BS EN 1992-1-1 is 111 *kN*. As the total experimental shear capacity of Beam N00 (see Section 4.3) was 143 *kN*, BS EN 1992-1-1 underestimates the shear capacity by 22.4%. When considering FRP strengthened beams, underestimating the steel contribution may lead to the erroneous conclusion that an over-conservative FRP design model is safe, when comparing the total experimental shear force resistance to the total predicted shear force resistance.

Section 6.2.1 presents a design example for a DE-strengthened concrete beam. Section 6.2.2 comments on the findings of the comparison between the experimental results and the FE predictions. The comparison was carried out for B15 only, due to the limited strain readings obtained in the steel reinforcement and CFRP composites.

6.2.1. *Example of shear contribution due to DE CFRP rods*

The following is a calculation of the DE CFRP rod shear contribution for B15 based on TR-55 (2012). When calculating DE CFRP rod shear contribution, all safety factors were set to 1.00. The relevant typical test values were used in this calculation. For notations, refer to Chapter 3, Equations 2.26 and 6.3.

Anchorage length

Average bond stress over length of anchor, τ_b = 15 *N/mm²* (TR55 2012)

Limiting effective strain in CFRP, ε_{fse} = 0.004 (TR55 2012)

Young's modulus of CFRP rod, E_{fd} = 124000 *N/mm²* (data sheet)

Deep embedded FRP rod diameter, d_b = 10 *mm* (data sheet)

Rod cross-sectional area, A_f = 71.3 *mm²* (data sheet)

Hence:

$$l_{b,max} = \frac{\varepsilon_{fse} E_{fd} A_f}{\left(\pi d_b \frac{\tau_b}{\gamma_A}\right)} = \frac{0.004 \times 124000 \times 71.3}{\left(\pi \times 10 \times \frac{15}{1}\right)} = 75\ mm$$

Effective width over which the deep embedment rods will act

The strengthened depth of the structure, h = 360 *mm* (beam dimension)

$w_{eff} = \left(h - 2l_{b,max}\right) = (360 - 2 \times 75) = 210\ mm$

Shear contribution of DE CFRP rods

Spacing of the deep embedded rods, s_b = 275 *mm*

$V_{Rd,f} = \frac{\varepsilon_{fse} E_{fd} A_f}{s_b} w_{eff} = \frac{0.004 \times 124000 \times 71.3}{275} \times 210 \times 10^{-3} = 27\ kN$

Therefore, the shear contribution of DE CFRP rods is 27 *kN.*

6.2.2. Comments

In the previous example, TR-55 (2012) slightly overestimates the shear contribution of DE CFRP rods (predicted as 27 *kN*) compared to the experimental result (23.8 *kN*). In general, this is a good prediction. However, recent research (Mofidi et al. 2012) suggests that TR-55 (2012) overestimates the average bond strength (15 *MPa*); see Section 6.4 for details. This might lead to overestimating the contribution of DE CFRP rods.

It should also be noted that TR-55 (2012) assumes that the strain in the DE FRP rods is 0.004. However, the experimentally measured maximum strain in the CFRP rods of B15 was 0.0024 (only 60% of the assumed strain). This seems to be another source of inaccuracy in the TR-55 (2012) design model for DE FRP rods.

6.3. Parametric study

The following subsections detail the parametric study. As mentioned in Section 6.1, the parametric study focused on beams strengthened with DE CFRP rods. The beams strengthened with EB CFRP sheets were excluded because of the relatively

high predicted-to-experimental shear strength ratio.

Three values of concrete cube compressive strength (f_{cu}) were considered in the parametric study. The value of 37 N/mm^2 was considered as representative of the concrete cube compressive strength for the majority of the tested beams. The other two values of 25 N/mm^2 and 50 N/mm^2 were representative of the concrete cube compressive strength for existing old and recently built structures respectively.

In the physical testing, DE-strengthened beams had a steel-to-CFRP shear reinforcement ratio of 2.12. This value was therefore included in the parametric study. From a practical point of view, the diameters of CFRP rods used in shear strengthening applications are about 10 *mm* and 13 *mm* respectively (refer to Aslan 200 product data sheet). These diameters result in additional steel-to-CFRP shear reinforcement ratios of 0.67 and 1.19. The three steel-to-CFRP shear reinforcement ratios considered in the parametric study were therefore 1.19, 2.12 and 0.67.

To evaluate the effect of shear span-to-effective depth ratio (a_v/d), three a_v/d values were considered. All tested beams had a_v/d ratio of 3.05 and therefore this value was selected. Two additional a_v/d values of 2.59 and 3.70 were adopted to provide a range of a_v/d values over which the shear strength enhancement can be measured.

A total of 18 nonlinear analyses were carried out to investigate the effect of the above parameters influencing the strength of RC T-beams strengthened in shear with DE CFRP rods. It should be noted that the FE models for the corroded beams were not considered in the parameter study. For further details, refer to Section 6.3.1.

In order to investigate the effect of a given parameter, only its value was varied and the values of the other parameters remained unchanged. A similar method was

adopted by Qapo et al. (2014). The shear force gain of DE CFRP rods was calculated by subtracting the predicted unstrengthened shear force resistance from the corresponding predicted strengthened shear force resistance. The predictions showed the performance ability of the FE modelling. Further physical tests are recommended to approve the predicted results.

Table 6.3.1 summarises the FE models developed for the parametric study. The designation A/B/C/D was used to refer to the FE models, where 'A' refers to the strengthening scheme ('N' for unstrengthened FE model and 'B' for DE CFRP rod strengthened model), 'B' refers to the concrete cube compressive strength ('25' for 25*MPa*, '37' for 37*MPa* or '50' for 50*MPa*), 'C' refers to the steel-to-CFRP shear reinforcement ratio (0.67, 1.19 or 2.12) and 'D' refers to the a_v/d ratio (2.59, 3.05 or 3.70). For example, B/37/0.67/3.05 is an FE model for a DE strengthened T-beam with a concrete cube compressive strength of 37 *MPa*, A steel-to-CFRP shear reinforcement ratio of 0.67, and a shear span-to-effective depth ratio of 3.05.

Table 6.3.1: Developed FE models for the parametric study

Cube Compressive Strength			**Steel-to-CFRP Shear Reinforcement Ratio**			**Shear Span-to-Effective Depth Ratio**		
25 *N/mm²*	**37 *N/mm²***	**50 *N/mm²***	**1.19**	**2.12**	**0.67**	**2.59**	**3.05**	**3.70**
N/25/2.12/3.05	N/37/2.12/3.05	N/50/2.12/3.05	N/37/1.19/3.05	N/37/2.12/3.05	N/37/0.67/3.05	N/37/2.12/2.59	N/37/2.12/3.05	N/37/2.12/3.70
B/25/2.12/3.05	B/37/2.12/3.05	B/50/2.12/3.05	B/37/1.19/3.05	B/37/2.12/3.05	B/37/0.67/3.05	B/37/2.12/2.59	B/37/2.12/3.05	B/37/2.12/3.70

6.3.1. *Effect of bond-slip model of corroded shear links*

Section 5.3 discussed the methodology of modelling bond-slip behaviour between steel shear reinforcement and concrete. Harajli et al. (2004) proposed a bond slip

model which was combined with the Saifullah and Clack (1994) proposed corrosion impact factor (also known as 'empirical factor 'R''); these were used to simulate the interface of the steel shear links to concrete in the test span.

All validated FE models included bond-slip modelling between the steel shear links and the concrete, as detailed in Section 5.6. Although the overall predictions were good (with an average experimental to FE model ratio of 1.17 and a standard deviation of 0.06), detailed analysis showed that some corroded beams had higher predicted shear force capacities than those of the uncorroded beams when other parameters were the same (see Figure 6.3.1b). This result disagrees with the experimental results. This discrepancy may be attributable to the bond-slip model. El-Maaddawy and Soudki (2003) suggested that the steel shear link-to-concrete bond initially increases, and then decreases due to corrosion level increase. The corrosion impact factor may be used to represent this behaviour numerically, and it may be related to the applied current density. For example, it showed that the bond stress increases until a shear link corrosion level of 14.8% (due to the rust forms), and decreases thereafter (due to the appearance of cracks). However, El-Maaddawy and Soudki (2003) induced the corrosion with a current density of 250 $\mu A/cm^2$. Hence, the recommended corrosion impact factor cannot be used in this FE modelling (this study is using a current density of 200 $\mu A/cm^2$). The adopted corrosion impact factor is based on the best-fit curve of shear force-to-deflection between the experimental results and FE predictions.

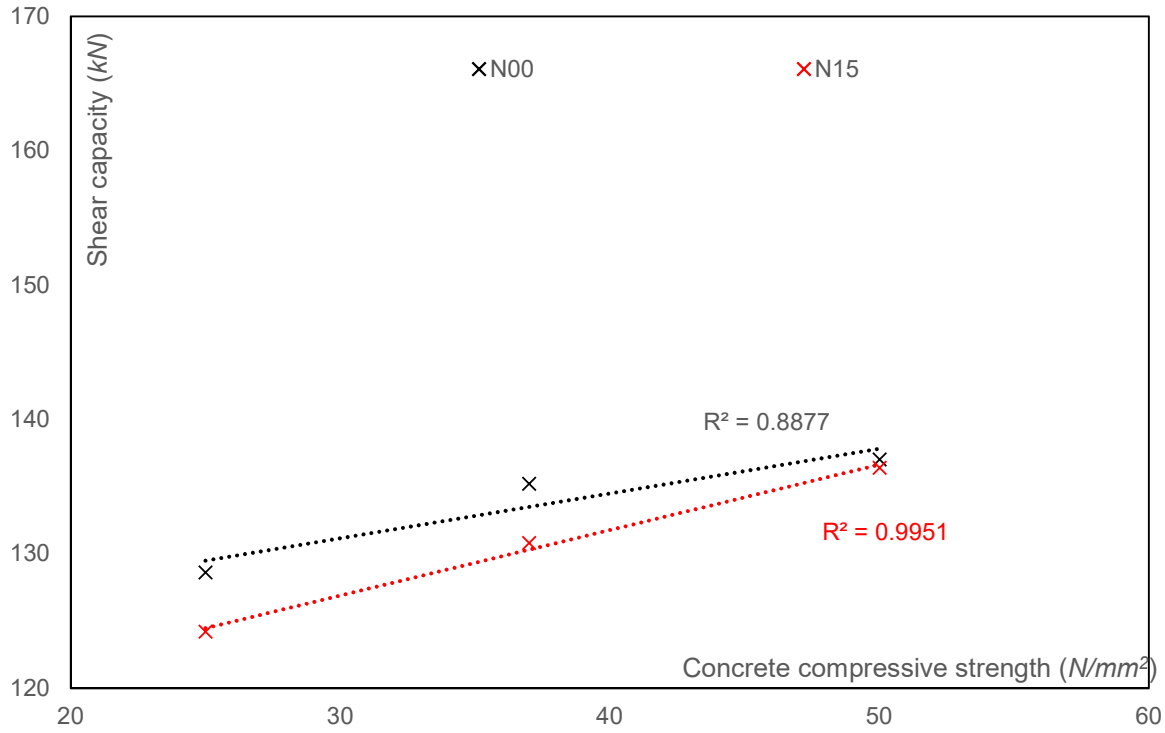

Figure 6.3.1: Effect of concrete compressive strength on shear force capacity of unstrengthened beams

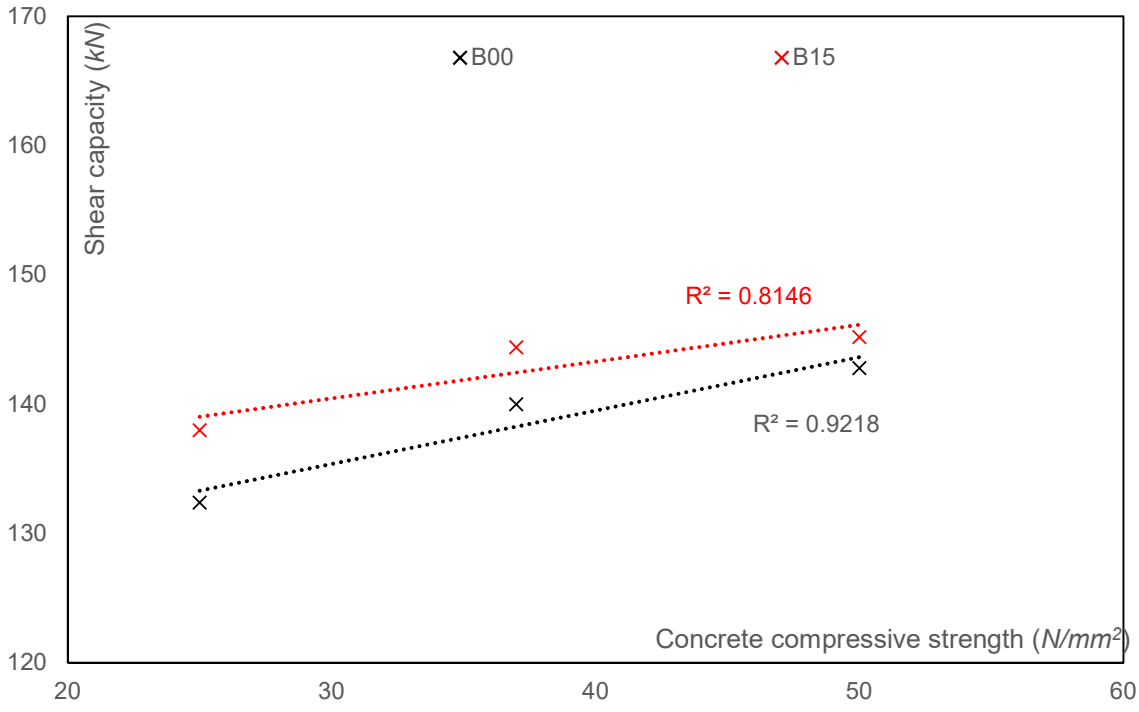

Figure 6.3.2: Effect of concrete compressive strength on shear force capacity DE strengthened beams

Based on the FE-predicted results and the limitations of the bond-slip model, the corroded beams were excluded from the parametric study because the adopted corrosion impact factor gave inexplicable predictions; the shear capacity of corroded beams was less in the unstrengthened beams, but higher in the DE strengthened beams when compared to the uncorroded beams. Hence, only the FE models for Beams N00 and B00 were considered reliable enough to be included in the parametric study.

6.3.2. *Effect of concrete compressive strength*

Figure 6.3.3 depicts the influence of concrete (cube) compressive strength on the predicted shear force resistance. The FE model predicted that shear force capacity increased approximately linearly with the increase in cube compressive strength, where the R-square (R^2), a measure of goodness-of-fit of linear regression, was 0.8877 and 0.9218 for unstrengthened and DE strengthened FE models, respectively. This may be explained by the fact that the increase in cube compressive strength enhances the concrete contribution to shear force capacity. Shear force resistance increased from 129 *kN* to 137 *kN* (by 6*%*) and 132 *kN* to 143 *kN* (by 8*%*), when the cube compressive strength was increased from 25 N/mm^2 to 50 N/mm^2 for unstrengthened and strengthened beams respectively.

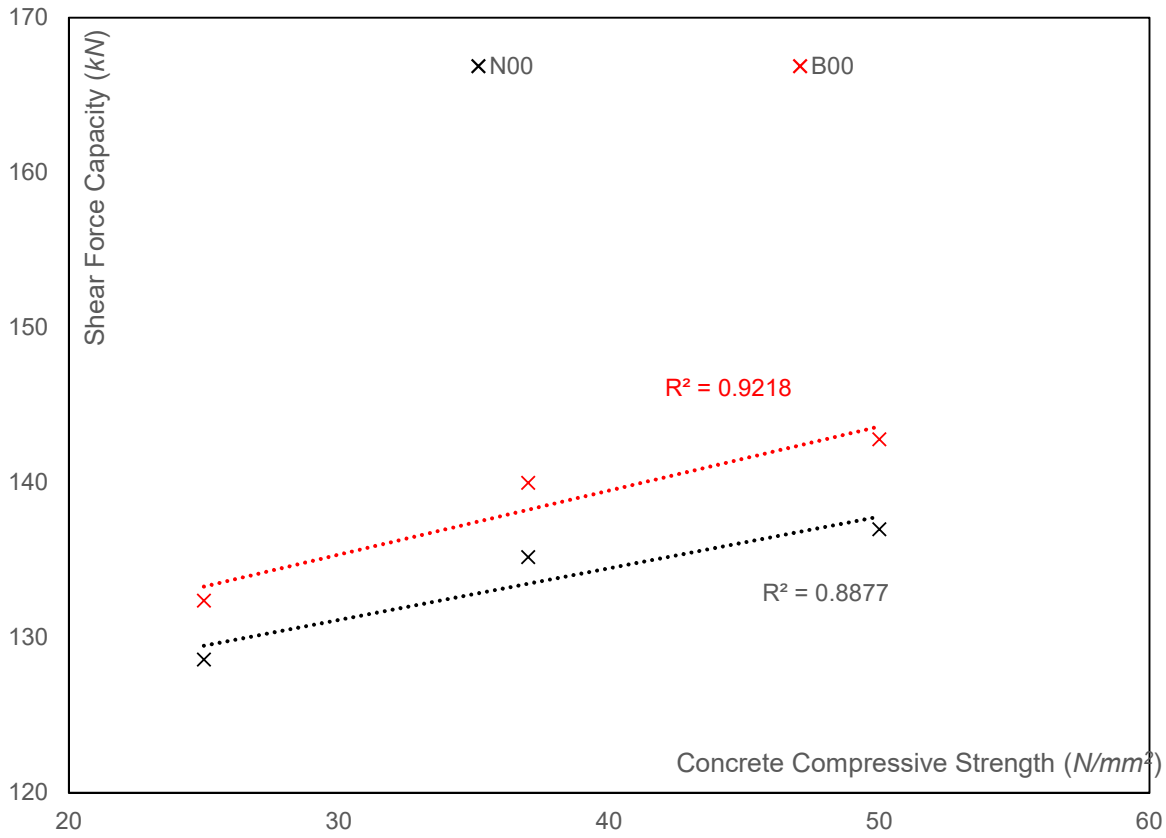

Figure 6.3.3: Effect of concrete compressive strength on shear force capacity

Figure 6.3.4 presents the variation of shear force gain due to the CFRP rods with concrete compressive strength. The increase in concrete compressive strength had an insignificant effect on the CFRP shear force gain. The increase in concrete compressive strength from 25 N/mm^2 to 50 N/mm^2 resulted in 2 *kN* (about 52.6% increase in CFRP rods and 19.2% increase when compared to overall shear capacity) shear strength enhancement (R^2 = 0.9995). TR-55 (2012) assumes that the CFRP contribution to shear force is unaffected by the variation in concrete compressive strength (R^2 = 1.0000). However, TR-55 (2012) predicted a much higher shear strength enhancement (about 27 *kN*) compared to that predicted by the FE model. Further testing is required to establish the effect of concrete compressive strength on shear force gain and investigate the accuracy of the numerical (FE) and

analytical (TR-55, 2012) models.

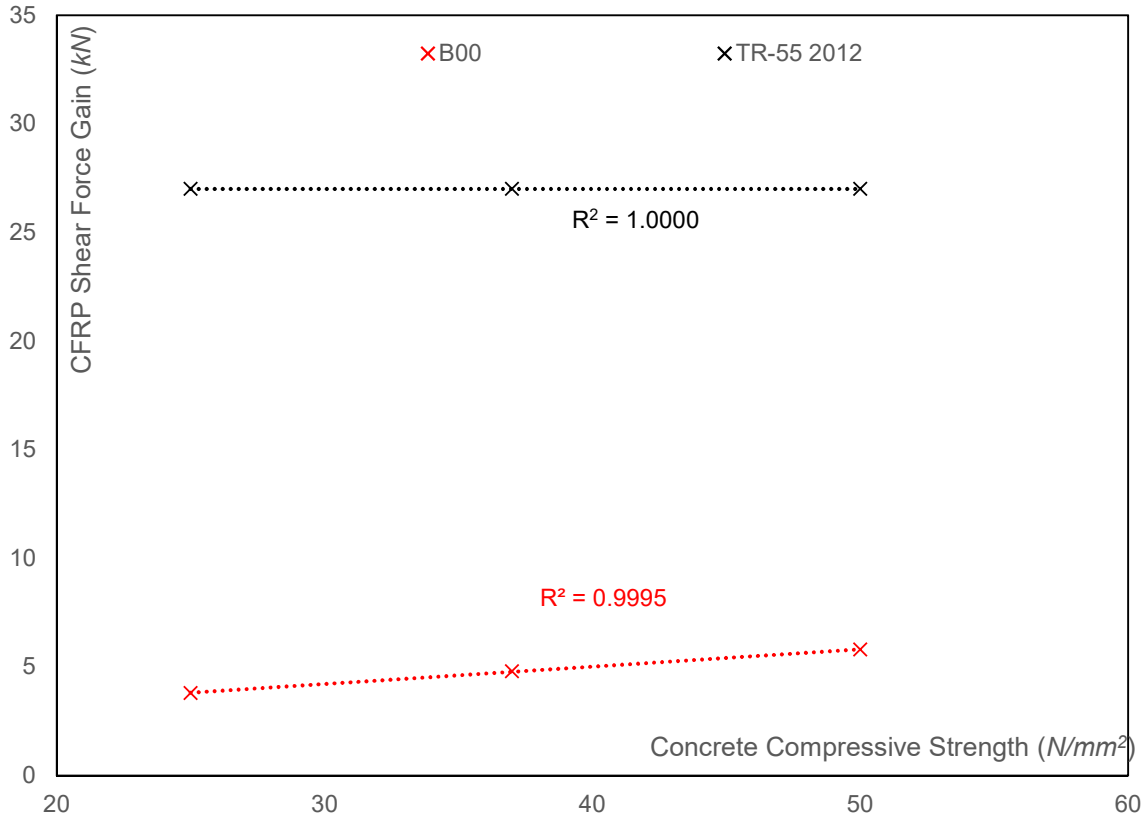

Figure 6.3.4: Effect of concrete compressive strength on shear force gain due to DE CFRP rods

6.3.3. *Effect of steel-to-CFRP shear reinforcement ratio*

This effect was investigated by modelling T-beams with various steel-to-CFRP ratios, $\rho_{s,f}$, (by varying the diameters of the steel shear link and CFRP rods). Other parameters, such as concrete compressive strength (37 N/mm^2) and shear span-to-effective depth ratio (3.05) were kept constant.

Three values were used to investigate the effect of steel-to-CFRP shear reinforcement ratio on shear force resistance, as well as the shear contribution of CFRP rods. These ratios of 0.67 (6 *mm* diameter shear links with 13 *mm* diameter

DE CFRP rods), 1.19 (6 *mm* diameter shear links with 10 *mm* diameter DE CFRP rods) and 2.12 (8 *mm* diameter shear links with 10 *mm* diameter DE CFRP rods), were calculated using Equation 6.1.

$$\rho_{s,f} = \frac{s_{frp} A_{st} E_{st}}{s_{st} A_{frp} E_{frp}} \quad (6.1)$$

where 'A_{st}' is the total area of shear links per location (mm^2), 'E_{st}' is the modulus of elasticity of shear links (N/mm^2), 'A_{frp}' is the total area of FRP reinforcement at the location (mm^2), 'E_{frp}' is the modulus of elasticity of FRP reinforcement (N/mm^2), 's_{st}' is the spacing between the shear links (*mm*) and 's_{frp}' is the spacing between the CFRP rods (*mm*).

Figure 6.3.5 and Figure 6.3.6 show the variation of predicted shear capacity and predicted shear force gain with steel-to-CFRP shear reinforcement ratio respectively. The shear capacity of DE-strengthened beams increased from 130 *kN* to 140 *kN* with the increase in steel-to-CFRP shear reinforcement ratio (i.e. from 0.67 to 2.12, R^2 = 0.8019). However, the shear contribution of DE CFRP rods decreased when the steel-to-DE shear reinforcement ratio increased (R^2 = 0.6361). Comparable results were reported by Breveglieri et al. (2015) who suggested that DE CFRP rods will increase overall shear capacity, but shear contribution of the DE rods decreases when the steel-to-DE shear reinforcement ratio increases.

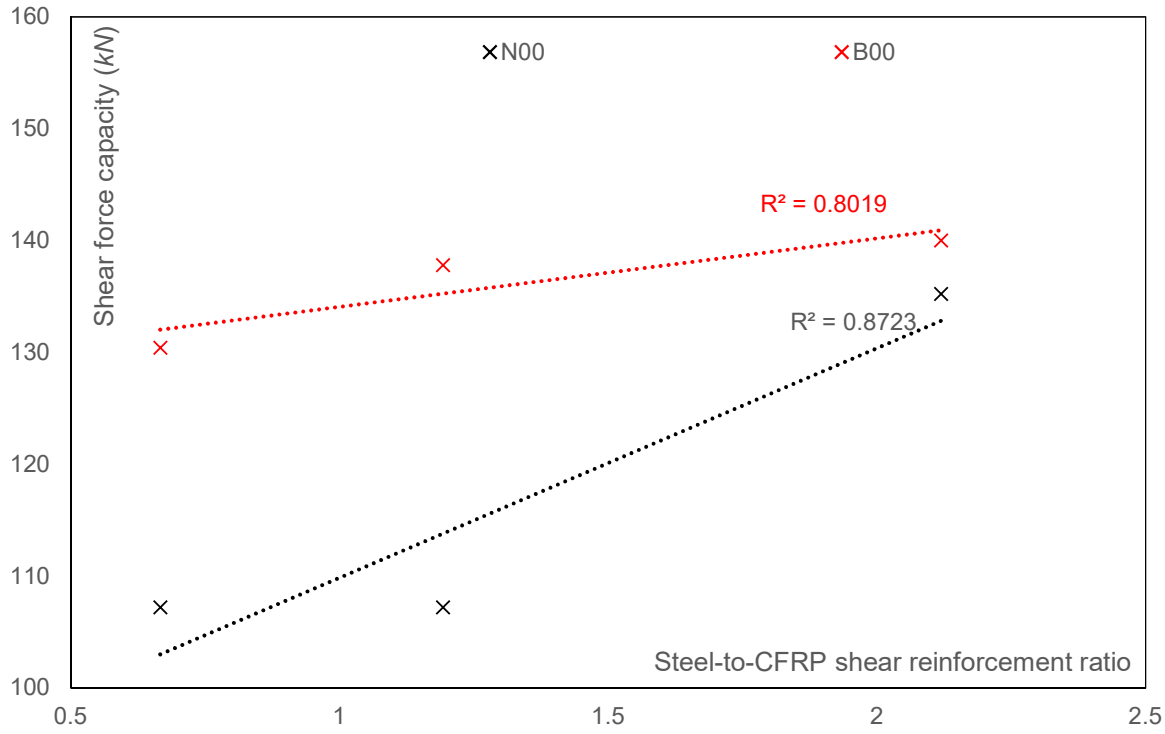

Figure 6.3.5: Effect of steel-to-CFRP shear reinforcement ratio on shear capacity

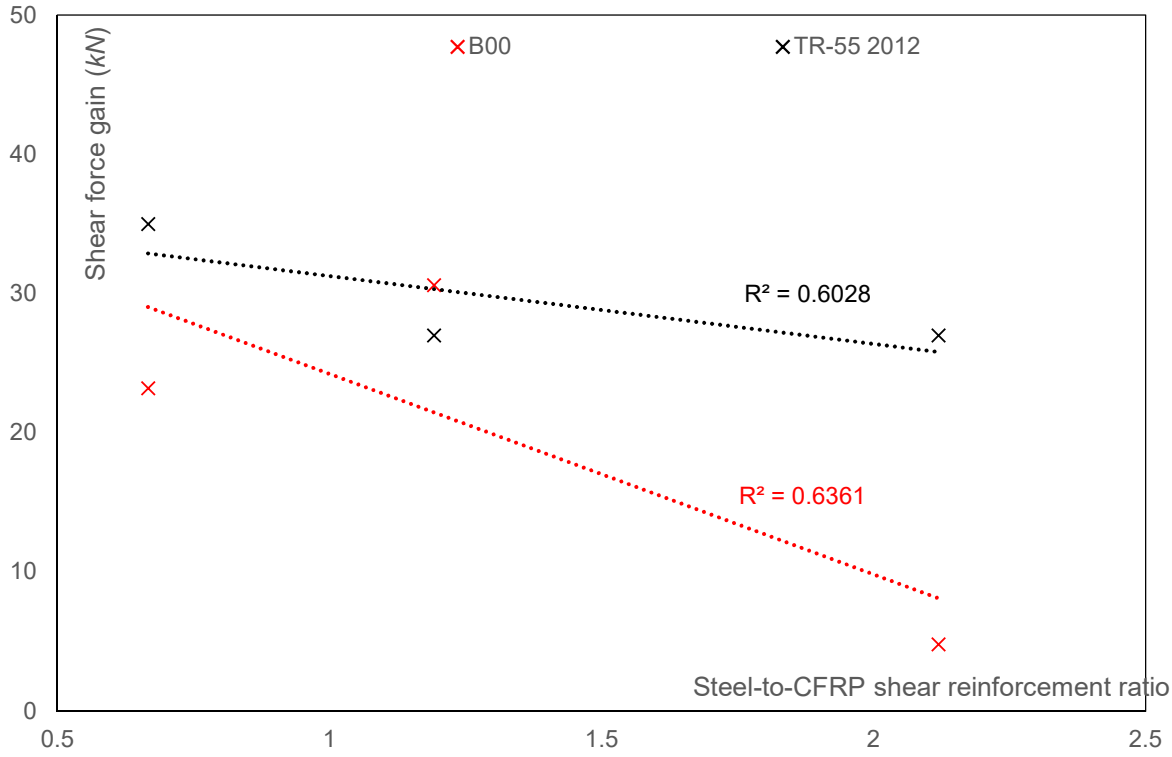

Figure 6.3.6: Effect of steel-to-CFRP shear reinforcement ratio on shear force gain

TR-55 predicted that the shear contributions of the 10 *mm* and 13 *mm* CFRP rods are 27 *kN* and 35 *kN* (R^2 = 0.6028) respectively. The effect of the steel-to-CFRP reinforcement ratio is not considered by TR-55 (2012). It can be observed that TR-55 (2012) generally predicted higher shear contribution values than those predicted by the FE model. This is particularly the case when the value of $\rho_{s,f}$ is 2.12, which is typical for all tested beams. A detailed comparison between the FE and TR-55 (2012) predictions is given in Section 6.4.

6.3.4. *Effect of shear span-to-effective depth ratio*

The shear span-to-effective depth ratio, a_v/d, is one of the significant parameters that influences shear behaviour and failure mode (see Chapter 2). Sayed et al. (2013) suggested that FRP shear contribution is strongly affected by a_v/d. However, the research investigation on such an effect is still limited, especially for RC beams shear-strengthened with DE FRP rods.

FE models nominally identical to those validated in Chapter 5, but with varying effective depths, were considered. Three effective depth values (243 *mm*, 295 *mm* and 347 *mm*) were used, which resulted in three a_v/d ratios (3.70, 3.05 and 2.59, respectively). Other parameters, such as concrete compressive strength (37 N/mm^2) and steel-to-CFRP shear reinforcement ratio (2.12), remained unchanged.

Figure 6.3.7 presents the influence of a_v/d ratio on shear force predictions. The results were comparable with the findings of Kani et al. (1979). For RC beams, the higher the a_v/d ratio, the lower the shear force resistance. Qapo et al. (2014) modelled beams strengthened with EB CFRP strips and suggested that the reduction

may be related to the shift from arch-action, which provides higher resistance, to beam-action. The total shear capacity decreased by 36% and 40% when the a_v/d ratio was increased from 2.59 to 3.70 for unstrengthened (R^2 = 0.9980) and DE CFRP-strengthened (R^2 = 0.9999) FE models respectively.

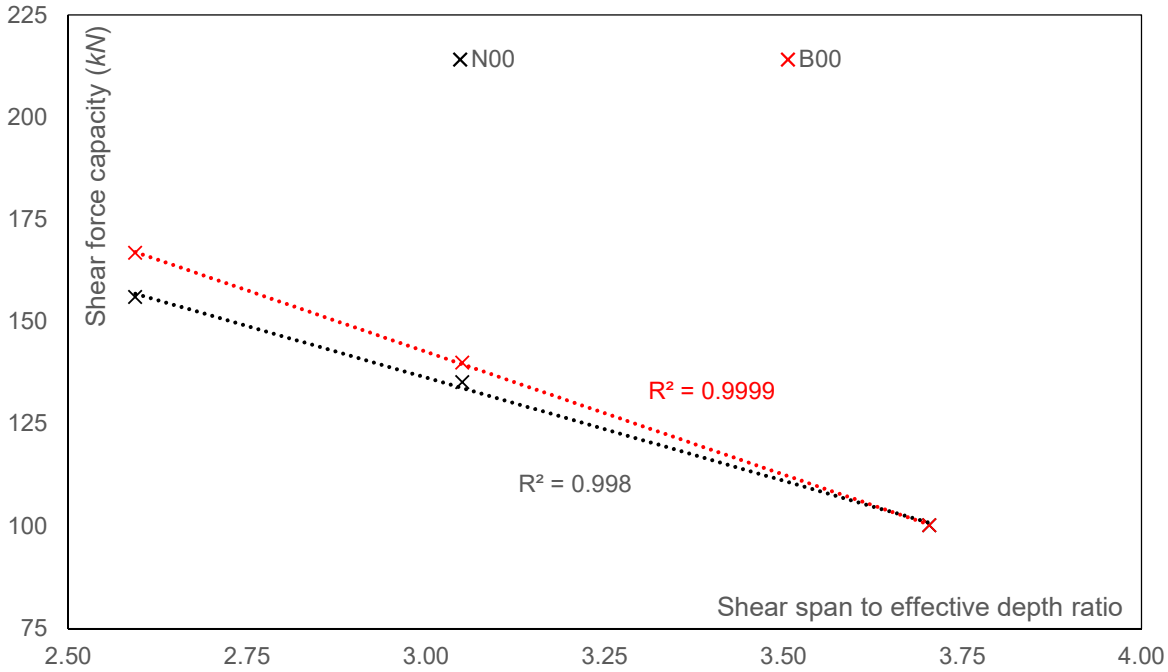

Figure 6.3.7: Effect of shear span-to-effective depth ratio on shear capacity

Figure 6.3.8 shows the influence of a_v/d ratio on predicted CFRP shear contribution. The FE predicted shear force gain decreased approximately linearly with the increase in a_v/d ratio where R^2 was 0.9729. It should be noted that the CFRP rods contribution to shear capacity at an a_v/d ratio of 3.70 was insignificant (towards 0 *kN*). TR-55 (2012) predictions increased linearly from 20 *kN* to 34 *kN* when the a_v/d ratio was increased from 2.59 to 3.70 (R^2 = 0.9897). Figure 6.3.8 suggests that the CFRP contribution was significantly overestimated by TR-55 as the a_v/d ratio increased. TR-55 did not take into account the effect of shear span-to-effective depth ratio. It underestimates the effective bonded length, and hence, the predictions increased as

the depth of the beams increased.

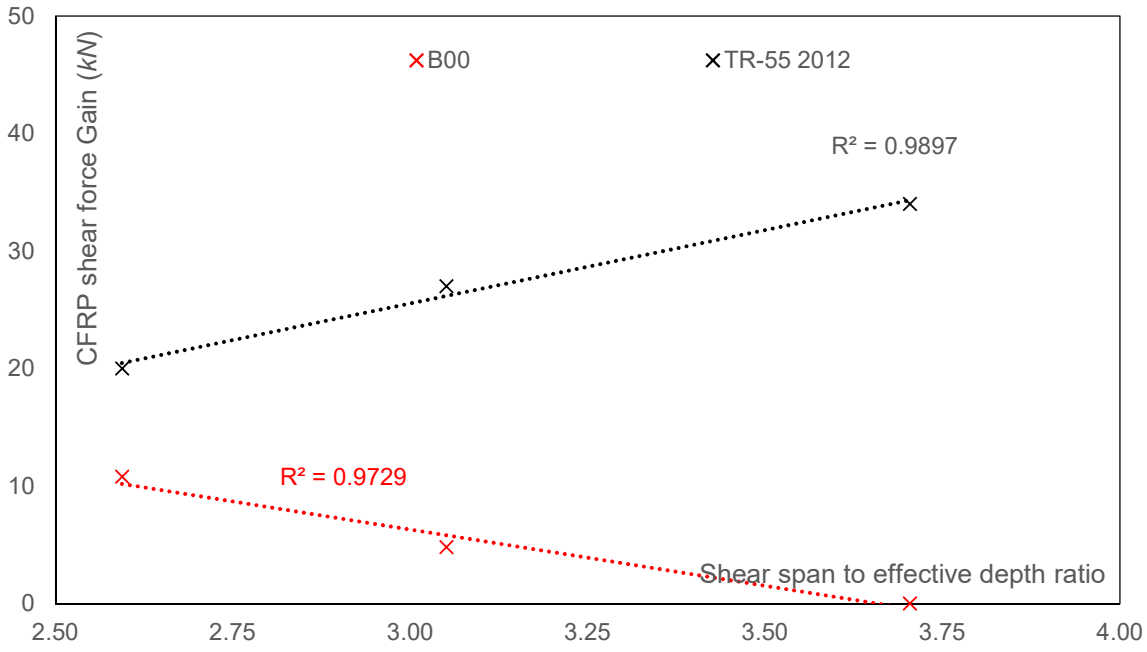

Figure 6.3.8: Effect of shear span-to-effective depth ratio on shear force gain

6.4. Comparison between FE and TR-55 predictions

Section 6.2 reviewed TR-55 published by the Concrete Society in 2012. Comparisons between TR-55 (2012) predictions and the experimental results of the 15% corroded RC beam strengthened with DE CFRP rods showed that TR-55 (2012) overestimates the experimental result. Due to the limited number of experimental tests, the predictions of TR-55 were compared with the parametric study results.

Table 6.4.1 gives the DE CFRP rod shear contributions predicted by TR-55 (2012), $V_{TR\text{-}55}$, and the FE predictions, V_{FE}. For beam notation, please refer to the designation explained in Section 6.3. TR-55 (2012) had higher predictions than the FE models, with an average ratio of 3.96 and a standard deviation of 2.07.

Table 6.4.1: Comparison between TR-55 and FE-predicted shear force gain due to DE CFRP rods

Beam designations	Prediction use TR-55, V_{TR-55} (*kN*)	Prediction use FE model, V_{FE} (*kN*)	Ratio of predictions, V_{TR-55}/V_{FE}
B/25/2.12/3.05	27	4	6.75
B/37/2.12/3.05	27	5	5.40
B/50/2.12/3.05	27	6	4.50
B/37/0.67/3.05	35	23	1.52
B/37/1.19/3.05	27	31	0.87
B/37/2.12/3.05	27	5	5.40
B/37/2.12/2.59	20	11	1.82
B/37/2.12/3.05	27	5	5.40
B/37/2.12/3.70	34	0	N/A
		Average	3.96
		Standard deviation	2.07

In order to further investigate the accuracy of TR-55 (2012), Table 6.4.2 presents the CFRP shear contributions predicted by TR-55 (2012), V_{TR-55}, and experimental results, V_{EXP}, reported by Chaallal et al (2011) and Mofidi et al (2012). Chaallal et al (2011) tested three RC T-beams strengthened with DE CFRP rods of diameter 12.7 *mm* and spacing of 130 *mm* c/c. Mofidi et al (2012) tested six RC T-beams repaired with DE CFRP rods. The investigated parameters included the diameter (either 9.5 *mm* or 12.7 *mm*), spacing (either 130 *mm* or 260 *mm*), and coating (either sand-coated or plain) of the DE CFRP rods. Table 6.4.2 also shows that TR-55 (2012) had higher predictions than the experimental results, with an average ratio of 1.92 and a standard deviation of 0.84.

Table 6.4.2: Comparison between experimental results and TR-55 predictions for the shear force gain due to DE CFRP rods

Experimental	Beam designations	Prediction use TR-55, V_{TR-55} (kN)	Experimental result, V_{EXP} (kN)	Ratio of prediction to experimental results, V_{TR-55}/V_{EXP}
Chaallal et al (2011)	S1-ETS	90	30.7	2.93
Mofidi et al (2012)	S0-12d130s*	90	99.5	0.90
Mofidi et al (2012)	S1-9d260s	35	14.0	2.50
Mofidi et al (2012)	S1-12d260s	45	20.3	2.22
Mofidi et al (2012)	S1-12d130s	90	31.4	2.87
Mofidi et al (2012)	S1-9d260p	35	34.4	1.02
Mofidi et al (2012)*	S3-12d130s*	90	87.1	1.03
			Average	**1.92**
			Standard deviation	**0.84**

* S0-12d130s and S3-12d130s are referenced as S0-ETS and S3-ETS in Chaallal et al (2011), respectively.

Table 6.4.1 and Table 6.4.2 suggest that TR-55 (2012) overestimates the shear contribution of the DE CFRP rods. This might be attributable to the relatively high FRP-to-concrete bond strength (15 N/mm^2) assumed by TR-55 (2012). Such an underestimation will overestimate the width over which deep embedded rods effectively carry shear force, and consequently TR-55 overestimated the shear contribution of CFRP rods.

6.5. Conclusions

The aim of this chapter was to compare the TR-55 predicted DE CFRP shear contribution to the predictions of NLFE models and experimental results. TR-55 proposed the design formula of the shear contribution of DE CFRP rods based on the truss analogy method. The composite effect of concrete and steel reinforcement is

not taken into consideration.

This chapter reviewed the latest FRP design guidance (TR-55), particularly on the shear contribution of DE CFRP rods. Predictions of TR-55 were compared with selected experimental results. Due to the limited number of experimental tests, TR-55 (2012) predictions were also compared with the predictions of FE models.

A parametric study was carried out to investigate the effects of concrete compressive strength, steel-to-CFRP shear reinforcement ratio and shear span-to-effective depth ratio, on the predicted shear strength and shear force gain.

Based on the results, the following conclusions were drawn.

1. Concrete compressive strength had a moderate influence on the concrete contribution to overall shear capacity. However, the CFRP shear contribution was not influenced by the variation of concrete compressive strength. Shear resistance increased linearly by 7% and 8% for unstrengthened and strengthened FE models respectively, when the concrete compressive strength was increased from 25 N/mm^2 to 50 N/mm^2.
2. Total shear resistance increased by 8% (10 *kN*) when the steel-to-CFRP shear reinforcement ratio was increased from 0.67 to 2.12. However, the CFRP contribution decreased by 79% (18 *kN*) when the same ratio increased from 0.67 to 2.12.
3. The predicted CFRP contributions decreased linearly from 10.8 *kN* to 0 *kN* with the increase in shear span-to-effective depth ratio from 2.59 to 3.70 respectively.
4. TR-55 (2012) had higher predictions than the FE models, with an average ratio of 3.96 and a standard deviation of 2.07. A similar result was found when comparing the predictions of TR-55 (2012) with selected experimental results, where TR-55 overestimated the shear contribution of DE CFRP rods, with an average ratio of 1.92 and a standard deviation of 0.85. The higher predictions

of TR-55 (2012) might be explained by overestimation of the average bond strength (15 N/mm^2).

5. This research has been completed in a limited time frame, and hence, limited experimental tests can be carried out. Although the numerical models were verified by experimental tests, more experimental tests are recommended to validate the above claims.

CHAPTER 7: CONCLUSIONS

7.1. Introduction

This chapter summarises the findings from the experimental tests, numerical simulations, parametric study of deep embedded (DE) CFRP rod strengthened RC T-beams and TR-55 accuracy evaluation. The main conclusions are listed in Section 7.2 and recommendations for future work are given in Section 7.3.

7.2. Conclusions

The aim of this study was to investigate the shear behaviour of corroded and uncorroded RC T-beams strengthened with different CFRP composites and the critical factors affecting shear contribution of DE CFRP rods, and to review the accuracy of TR-55 which estimates shear contribution of DE CFRP rods at the ultimate limit state. The following conclusions were drawn.

7.2.1. *Conclusions from experimental results*

The objective of the experimental tests was to identify the effect of monotonic loading on shear capacity and failure modes of un-strengthened, as well as CFRP-strengthened, RC T-beams with corroded shear links. The following conclusions can be drawn:

1. Both the mechanical and physical properties of the shear links deteriorated with increasing corrosion levels. The deterioration of the shear link properties resulted in a reduction in the shear contribution of the corroded shear links. Consequently, the normalised shear resistances of the corroded beams were less than those of the uncorroded beams. The experimental results showed

that the unstrengthened RC T-beams with shear link corrosion levels of 7% and 12% had normalised shear strengths that were 11% and 14% respectively less than the normalised shear strength of the un-corroded, unstrengthened RC T-beams, due to deterioration in the shear links.

2. A shear link corrosion level of 7% did not have a significant effect on the normalised shear strength of the strengthened RC T-beams, when compared with the normalised shear strength of the corresponding un-corroded RC T-beams strengthened with deep embedment (DE) or externally bonded (EB) CFRP systems. Both strengthening techniques were effective in re-instating the normalised shear strength of the beams with shear link corrosion levels of 7%. For a 12% corrosion level, the strengthening systems were almost effective at returning the beams to their un-corroded, unstrengthened normalised shear strength: about 96% and 95% for DE and EB strengthened methods respectively.
3. It can be seen that the effectiveness of both strengthening systems decreased with increasing shear link corrosion levels. It should be noted that the effectiveness of the EB method has been investigated by many researchers. However, this research is the first time the effectiveness of the DE method has been investigated.
4. In general, corrosion had a limited effect on the deflection response of the strengthened beams. The stiffness of the unstrengthened beams decreases with increasing corrosion levels. The beams strengthened with the EB technique had a stiffer response and less strain in the shear links compared with the corresponding beams strengthened with the DE technique. The deflections at failure are between 9 *mm* to 11 *mm* and 8 *mm* to 10 *mm*, for DE CFRP rods and EB CFRP sheets strengthened RC T-beams respectively.
5. The un-anchored EB CFRP sheets debonded from the concrete surface at failure. The debonding of EB CFRP sheets resulted in limited strain in the CFRP sheets (less than 0.0013). On the other hand, the embedded CFRP rods did not show signs of debonding and developed higher strain (0.0013 – 0.0027) compared with the EB sheets. Strain analysis suggests that steel contribution to total shear resistance decreased with increasing corrosion

levels.

6. The un-anchored EB CFRP sheets did not contribute significantly to total shear resistance, whereas the concrete contributed about 46% to total shear resistance of the strengthened beams with a 12% corrosion level. The DE CFRP rods started to contribute to shear resistance once the shear links were activated. Shear resistance of the DE CFRP rods increased until failure took place. The contribution of the DE CFRP rods was about 15% of total shear resistance of the strengthened beams with a 12% corrosion level.

7.2.2. *Conclusions from finite element modelling results*

The objective of numerical simulation was to develop non-linear finite element (NLFE) predictive tools capable of modelling the behaviour of the experimental specimens. The following conclusions can be drawn:

1. The FE-predicted shear capacities were in fair agreement with the experimental results. The mean experimental/predicted capacity ratios were 1.12, 1.13 and 1.19, with standard deviations of 0.02, 0.02, and 0.05, for the unstrengthened, DE strengthened and EB strengthened beams respectively.
2. The results showed that the FE models generally had stiffer deflection response prior to crack formation than the experimental beams. Once the crack forms, the stiffness was comparable between the FE predictions and experimental results.
3. All the tested beams were characterised by shear failure. The FE models also captured the same failure crack patterns. However, post-failure behaviour was not simulated as it was out of research interest.
4. The NLFE analysis simulated less cracks compared with experimental results for the corresponding RC T-beams. This may be because the numerical model cannot simulate the heterogeneous nature of the concrete. However, the predicted failure crack patterns were in good agreement with the crack patterns of the tested beams, where the main inclined cracks followed a path from the support to the load point in the web.

7.2.3. *Conclusions from parametric study results*

The objective of the parametric study was to identify the effect of concrete strength, steel-to-CFRP shear reinforcement ratio and shear span-to-effective depth ratio on the shear strength enhancement offered by DE CFRP rods. The following conclusions can be drawn:

1. Concrete compressive strength had a moderate influence on concrete contribution to the overall shear force resistance. However, DE CFRP shear contribution was less influenced by the variation in concrete compressive strength. The DE CFRP shear contributions increased linearly, from 3.8 *kN* to 5.8 *kN,* when the concrete compressive strength increased from 25 N/mm^2 to 50 N/mm^2, but overall shear capacity increased from 132.4 *kN* to 142.8 *kN* for DE CFRP strengthened RC T-beams.
2. Total shear capacity increased by 8% (10 *kN*) when the steel-to-CFRP shear reinforcement ratio was increased from 0.67 to 2.12. However, the DE CFRP shear contribution decreased by 79% (18 *kN*) when the same ratio increased from 0.67 to 2.12.
3. Total shear capacity decreased from 166.8 *kN* to 100.2 *kN* when the shear span-to-effective depth ratio was increased from 2.59 to 3.70. The predicted DE CFRP shear contribution also decreased from 10.8 *kN* linearly to 0 *kN* when the same ratio increased from 2.59 to 3.70.

7.2.4. *Conclusions from comparison with TR-55 predictions*

The last objective was to evaluate the accuracy of TR-55 predictions using experimental and numerical results for the shear contribution of the DE CFRP rods. The following conclusions can be drawn:

1. Due to the limited number of experimental results of un-corroded RC T-beams strengthened with DE CFRP rods, the predicted DE CFRP rod shear contribution of TR-55 was compared with experimental tests carried out by

Chaallal et al (2011) and Mofidi et al (2012). This showed that TR-55 overestimated the CFRP shear contribution. The average ratio of TR-55/experimental results was 3.96 with a standard deviation of 2.07.

2. Comparing predicted DE CFRP rod shear contribution of TR-55 to the predictions of the validated NLFE models in this research, the average ratio of TR-55/FE predictions was 1.92 with a standard deviation of 0.85.
3. The higher TR-55 predictions might be caused by the relatively high value of average bond strength suggested by TR-55 (2012), which is 15 N/mm^2.
4. It should also be noted that TR-55 does not consider the effect of concrete compressive strength and shear span-to-effective depth ratio on the shear contribution of DE CFRP rods. More critically, the NLFE analysis showed that the DE CFRP shear force gain reduced from 10.8 *kN* to 0 *kN* as the shear span-to-effective depth increased from 2.59 to 3.70, whereas TR-55 predicted an increase in the CFRP shear contribution as the embedded length was increased.
5. Predicted DE CFRP rod shear contribution of TR-55 was decreased from 35 *kN* to 27 *kN* when the steel-to-CFRP shear reinforcement ratio was increased from 0.67 to 2.12. However, the NLFE analysis showed that the effect of the steel-to-CFRP shear reinforcement ratio on shear contribution was less than that considered by TR-55 as the increase in the ratio.

7.3. Recommendations for future research

Currently, the DE CFRP rod strengthening method has not been used in practice, although the concept was demonstrated and approved by Valerio et al. (2009). This research has demonstrated that the DE CFRP rod strengthening method is an efficient strengthening method, but it has limitations. It cannot be used if the as-built reinforcement details are missing or where drilling through a deep depth structure is required. Based on the findings and conclusions of this study, recommendations pertaining to physical tests, numerical simulations and design standards are

suggested.

7.3.1. *Recommendations for experimental tests*

A limited number of parameters were investigated in the current research. To deepen the understanding of the shear behaviour of corroded RC T-beams strengthened with FRP composites, the influence of the following parameters should be further identified via physical tests: the effect of the corrosion level of shear links above 12%, beam size, boundary conditions, longitudinal reinforcement and shear span-to-effective depth ratio less than 3.00.

It should be noted that laboratory specimens should have practical dimensions. The strengthening effectiveness of FRP has to be investigated in the case of short shear spans in which arch action behaviour governs failure.

Different types of FRP composite materials are required to investigate the shear strengthening of RC beams, such as glass and aramid FRP composites. Finally, an experimental programme to investigate the bond characteristics of DE FRP rods is highly recommended.

7.3.2. *Recommendations for numerical investigation*

The parameters recommended in the preceding section are also applicable for numerical investigations. The FE models predicted the crack patterns well. However, there were limitations regarding the stiffness and deflection predictions. Moreover, the analysis was time-consuming. It is therefore recommended both the accuracy and efficiency of the developed FE models should be improved. It is also recommended that more comparison of modelling data should be carried out to

strengthen the numerical claims.

7.3.3. *Recommendations for design standards*

Chapter 6 reviewed current design guidance for strengthening concrete structures using fibre composite materials (TR-55). TR-55 overestimates the shear contribution of the DE CFRP rods. It is therefore recommended that TR-55 should be reviewed according to the research outcomes. Finally, the shear span-to-effective depth ratio that lower than or greater than the selected range (the shear span-to-effective depth in this research is a range from 2.59 to 3.07) should be investigated especially when considering the effects on corroded steel reinforcements.

REFERENCES

AASHTO, (2012). “AASHTO LRFD bridge design specifications.” 6th ed. Washington, American Association of State Highway and Transportation Officials.

ACI-ASCE Committee 326 Report, (1962). “Shear and diagonal tension.” Journal ACI, 59, pp 1-30, 277-334 and 352-396.

ACI-ASCE Committee 429, (1973). “The shear strength of reinforced concrete members.” ASCE Journal, Struct. Div., 99, 1091-1187.

ACI Committee 318, (2011). “318-11: Building code requirements for structural concrete and commentary.” MI USA, 503p.

ACI Committee 440, (2015). “Fiber-reinforced polymer reinforcement.” MI USA.

Kallias, Alexandros N. and Imran Rafiq, M. (2010). “Finite element investigation of the structural response of corroded RC beams.” Engineering Structures, 32(9), 2984-2994.

Almusallam, A.A. (2001). “Effect of degree of corrosion on the properties of reinforcing steel bars.” Constr. Built. Mater. 15 (8), 361-368.

Al-Sulaimani, G.J., Kaleemullah, M., Basunbul, I.A., and Rasheeduzzafar. (1990). “Influence of corrosion and cracking on bond behaviour and strength of reinforced concrete members.” ACI Structural Journal, 87(2), 220-231.

Andrade, C., Alonso, C. Garcia, D. and Rodriguez, J. (1991). “Remaining lifetime of reinforced concrete structures: effect of corrosion in the mechanical properties of the steel, life predication of corrodible structures.” NACE, Cambridge, UK, 23-26, 12/1-12/11.

ASTM International. (2011). “Standard practice for preparing, cleaning, and evaluating corrosion test specimens.” *ASTM G1-03*, West Conshohocken, PA.

Azad, A.K., Ahmad, S., and Azher, S.A. (2007). “Residual strength of corrosion-damaged reinforced concrete beams.” ACI Materials Journal, 104(1), 40-47.

Balaguru, P., Nanni, A., and Giancaspro, J. (2009). “FRP composites for reinforced and prestressed concrete structures.” Taylor & Francis, Abingdon, England.

Bažant, A.P., and Oh, B.H. (1983). “Crack band theory for fracture of concrete.”

Materials and Structures, 16, 155-177.

Bažant, Z.P., and Kim, J.K. (1984). “Size effect in shear failure of longitudinally reinforced beams.” J. of ACI, 81(5), 456-468, 82(4), 579-583.

Bažant, Z.P. (1984). “Size effect in blunt fracture: concrete, rock, metal.” Journal of engineering mechanics, 110(4), 518-535.

Belarbi, A., Bae, S.W., and Brancaccio, A. (2012). “Behavior of full-scale RC T-beams strengthened in shear with externally bonded FRP sheets.” Construction and Building Materials, 32 (2012), 27-40.

Bédard, C., and Kotsovos, M.D. (1986). “Fracture processes of concrete for NLFEA methods.” Journal of Structural Engineering, 112(3), 573-587.

Bhal, N. S. (1968). “Über den Einfluss der Balkenhöhe auf Schubtragfähighkeit von einfeldrigen Stalbetonbalken mit und ohne Schubbewehrung.” Dissertation, Universität Stuttgart.

Bonacci, J., and Maalej, M. (2001). “Behavioural trends of RC beams strengthened with externally bonded FRP.” J. Compos. Constr., 5(2), 102-103.

Bousselham, A., and Chaallal, O. (2006). “Behaviour of reinforced concrete T-beams strengthened in shear with Carbon Fiber-Reinforced Polymer – an experimental study.” ACI Structural Journal, 103(3), 339-347.

Breveglieri, M., Aprile, A., and Barros, J.A.O. (2015). “Embedded Through-Section shear strengthening technique using steel and CFRP bars in RC beams of different percentage of existing shear links.” Composite Structures, 126, 101-113.

BS EN 12390-1 (2000), “Testing Hardened Concrete - Shape, dimensions and other requirements for specimens and moulds.” British Standards Institution.

BS EN 12390-4 (2000), “Testing Hardened Concrete - Compressive strength specification for testing machines.” British Standards Institution.

BS 4449:2005 (2005), “Steel for the reinforcement of concrete – Weldable reinforcing steel – Bar, coil and decoiled product – specification.” British Standards Institution.

BS EN 12390-2 (2009), “Testing Hardened Concrete – Making and curing specimens for strength tests.” British Standards Institution.

BS EN 12390-3 (2009), “Testing Hardened Concrete - Compressive strength of test

specimens.” British Standards Institution.

BS EN 12390-5 (2009), “Testing Hardened Concrete - Flexural strength of test specimens.” British Standards Institution.

BS EN 12390-6 (2009), “Testing Hardened Concrete - Tensile splitting strength of test specimens.” British Standards Institution.

BS EN 12390-7 (2009), “Testing Hardened Concrete – Density of hardened concrete.” British Standards Institution.

BS EN ISO 15630-1 (2010), “Steel for the reinforcement and prestressing of concrete – test methods – reinforcing bars, wire rod and wire.” British Standards Institution.

BS EN 197-1 (2011), “Cement, composition, specifications and conformity criteria for common cements.” British Standards Institution.

Cairns, J. (1995), “Strength in shear of concrete beams with exposed reinforcement, Proceedings of the Institution of Civil Engineers.” Structures and Buildings 110 (1995) 176–185.

Cairns, J., Plizzari, G., Du, Y., Law, D.W. and Franzoni, C. (2005). “Mechanical properties of corrosion-damaged reinforcement.” ACI Materials Journal, 102(4), 256-264.

Chaallal, O., Nollet, M.J., and Perraton, D. (1998). “Strengthening of reinforced concrete beams with externally bonded fibre-reinforced-plastic plates: design guidelines for shear and flexure.” Canadian Journal of Civil Engineering, 25(4), 692-704.

Chaallal, O., Mofidi, A., Benmokrane, B., and Neale, K. (2011). “Embedded through-section FRP rod method for shear strengthening of RC Beams: performance and comparison with existing techniques.” J. Compos. Constr., 15(3), 374-383.

Chajes, M.J., Januszka, T.F., Mertz, D.R., Thomson, T.A., Jr, and Finch, W.W., Jr (1995). “Shear strengthening of reinforced concrete beams using externally applied composite fabrics.” ACI Structural Journal, 92(3), 295-303.

Chen, G.M., Teng, J.G., and Chen, J.F. (2011). "Finite element modelling of intermediate crack debonding in FRP-plated RC beams." J. Compos. Constr., 15(3), 339–353.

Chen, G.M., Chen, J.F., and Teng, J.G. (2012). "On the finite element modelling of RC beams shear-strengthened with FRP." Constr. Build. Mater., 32(1), 13–26.

Chen, J.F., and Teng, J.G. (2001). "Anchorage strength models for FRP and steel plates attached to concrete." Journal of Structural Engineering, ASCE, 127(7), 784-791.

Chen, J.F., and Teng, J.G. (2003a). "Shear capacity of FRP strengthened RC beams: FRP rupture." Journal of Structural Engineering, 129(5), 615-625.

Chen, J.F., and Teng, J.G. (2003b). "Shear capacity of FRP strengthened RC beams: FRP debonding." Structural Applications of FRP Composites, 17(1), 27-41.

Concrete Society. (2012). "Technical Report 55 (TR-55): Design guidance for strengthening concrete structures using fibre composite materials." Crowthorne, United Kingdom, 203.

Craig, B., and Soudki, K. A. (2005). "Post-repair performance of bond critical corrosion damaged concrete beams repaired with CFRP." ACI SP 230, FRPRCS-7, Farmington Hills, Mich., 563-578.

Denton, S.R., Shave, J.D., and Porter, A.D. (2004). "Shear strengthening of reinforced concrete structures using FRP composite." Advanced Polymer Composites for Structural Applications in Construction, Hollaway, LC, Chryssanthopoulos, MK and Moy, SSJ (Eds), Woodhead Publishing Limited, Abington, Cambridge, 134–143.

DIANA. (2012), User's Manual, Version 9.4.4., TNO DIANA BV, Delft, The Netherlands.

Dirar, S., Lees, J., and Morley, C. (2012). "Precracked reinforced concrete T-beams repaired in shear with bonded carbon fiber-reinforced polymer sheets." ACI Struct. J., 109(2), 215-224.

Dirar, S., Lees, J. M., and Morley, C. T. (2013). "Precracked reinforced concrete T-beams repaired in shear with prestressed carbon-fiber reinforced polymer straps." *ACI Struct. J.*, 110(5), 855-866.

Du, Y. G. (2001). "Effect of reinforcement corrosion on structural concrete ductility." PhD thesis, University of Birmingham, England, UK, 318.

Du, Y. G., Clark, L. A. and Chan, A. H. C. (2005), "Residual capacity of corroded

reinforcing bars." Magazine of Concrete Research, 57(3), 135-147.

El-Maaddawy, T.A., and Soudki, K.A. (2003). "Effectiveness of impressed current technique to simulate corrosion of steel reinforcement in concrete." J. Mater. Civ. Eng., 15 (1), 41-47.

El Maaddawy, T.A., and Soudki, K. (2005). "Carbon-fiber-reinforced polymer repair to extend service life of corroded reinforced concrete beams." J. Compos. Constr., 9(2), 187-194.

El Maaddawy, T.A., and Soudki, K. (2007). "Performance evaluation of carbon fiber-reinforced polymer-repaired beams under corrosive environmental conditions." ACI Struct. J., 104(1), 3-11.

El-Maaddawy, T.A., and Chekfeh, Y. (2013). "Shear strengthening of T-Beams with corroded shear links using composites." ACI Struct. J., 110(5), 779-790.

Eshwar, N., Nanni, A., and Ibell, T. J. (2008). "Performance of two anchor systems of externally bonded fiber-reinforced polymer laminates." ACI Mater. J., 105(1), 72-80.

Eurocode 2, (2004). "Design of concrete structures – Part 1-1: General rules and rules for buildings", Brussels, 225p.

Evans, R.H., and Kong, F.K. (1987). "Reinforced and prestressed concrete." 3rd ed. New York, Taylor and Francis Group.

Fib Task Group 9.3, (2001). "Bulletin 14: externally bonded FRP reinforcement for RC structures." International Federation for Structural Concrete (fib), Lausanne, Switzerland, 138.

Ge, Y., Elshafie, Z.E.B.M., Dirar, S., and Middleton, R.C. (2014). "The response of embedded strain sensors in concrete beams subjected to thermal loading." Construction and Building Materials, 70(2014), 279-290.

Godat, A., Labossière, P., Neale, K.W., and Chaallal, O. (2012). "Behavior of RC members strengthened in shear with EB FRP: Assessment of models and FE simulation approaches." Computers & Structures, Volumes 92–93, 269-282,

Harajli, M.H., Hamad, B.S., and Rteil, A.A. (2004). "Effect of confinement on bond strength between steel bars and concrete." Structural Journal, 101(5), 595-603.

Hee, S.C., and Jefferson, A.D. (2008). “A new model for simulating cracks in cementitious composites.” Proceedings of the Institution of Civil Engineers – Engineering and Computational Mechanics, 161(1), 3-16.

Heffernan, P. J., and Erki, M. A. (2004). “Fatigue behaviour of reinforced concrete beams strengthened with carbon fibre reinforced plastic laminates.” J. Compos. Constr., 8(2), 132-140.

Higgins, C., and Farrow, W.C. (2006), “Tests of reinforced concrete beams with corrosion damaged shear links.” ACI Struct. J. 103 (1) 133–141.

Hill, K.O., Fujii, Y., Johnson, D. C., and Kawasaki, B. S. (1978). "Photosensitivity in optical fiber waveguides: application to reflection fiber fabrication". Appl. Phys. Lett. 32 (10): 647.

Hordijk, D.A., Reinhardt, H.W., and Cornelissen, H.A.W. (1986). “Tensile tests and failure analysis of concrete.” J. of Structural Engineering, ASCE, 112, 2462-2477.

Kallias, A.N., and Rafiq, M.I. (2010). “Finite element investigation of the structural response of corroded RC beams.” Engineering Structures, 32(9), 2984-2994.

Kani, G.N.J. (1967). “How safe are our large reinforced concrete beams?” Proc., J. Am. Concr. Inst., 64(31), 128-141.

Kani, G., Huggins, M.W., and Wittkopp, R.R. (1979). “Kani on shear in reinforced concrete.” Department of Civil Engineering, University of Toronto, Canada, 225 pp.

Khayat, K.H., and De Schutter, G. (2014). “Mechanical properties of self-compacting concrete – Final draft report of RILEM Technical Committee 228-MPS.” Springer, Report Volume 14.

Kong F.K. (2002). “Reinforced concrete deep beams.” New York, Taylor and Francis Group.

Koutas, L., and Triantafillou, T. C. (2013). “Use of anchors in shear strengthening of reinforced concrete T-beams with FRP.” J. Compos. Constr., 17(1), 101-107.

Kreuzer, M. (2006). “Strain measurement with fiber Bragg grating sensors.” HBM, Damstadt, S2338-1.0 e.

Landolt, D. (2007). “Corrosion and surface chemistry of metals.” CRC Press.

Lau, K.T., Yuan, L., Zhou, L.M., Wu, J., and Woo, C.H. (2001). “Strain monitoring in

FRP laminates and concrete beams using FBG sensors." Composite structures, 51(1), 9-20.

Lee, H.S., Tomosawa, F., and Noguchi, T. (1996). "Effect of rebar corrosion on the structural performance of single reinforced beams." Durability of Building Materials and Components, 7, 571-580.

Loudon, N., and Bell, B. (2010). "FRP Strengthening of Concrete Road and Rail Bridges in the UK." Magazine of Concrete Research, Vol. 62, No. 4, pp. 243-252.

Lu, X.Z., Teng, J.G., Ye, L.P., and Jiang, J.J. (2005). "Bond-slip models for FRP sheets/plates bonded to concrete." Engineering Structures, 27(6), 920-937.

MacGregor, J.G. and Bartlett, F.M. (2000). "Reinforced concrete: mechanics and design." 1st ed. Englewood Cliffs: Prentice-Hall.

Malumbela, G., Moyo, P., and Alexander, M. (2012). "A step towards standardising accelerated corrosion tests on laboratory reinforced concrete specimens." J. S. Afr. Inst. Civ. Eng., 54(2), 78-85.

Matamoros, A.B., and Wong, K.H. (2003). "Design of simply supported deep beams using strut-and-tie models," ACI Structural Journal, 100(6), 704-712.

Meier, U., Deuring, M., Meier, H., and Shwelger, G. (1992). "Strengthening of structures with CFRP laminates: Research and applications in Switzerland." 1st Int. Conf. on Advanced Composite Materials in Bridges and Structures, K. W. Neale, ed., Univ. of Sherbrook, Sherbrook, Quebec.

Meier, U., Triantafillou, T.C., and Deskovic, N. (1995a). "Innovative design of FRP combined with concrete: short-term behaviour." J. Struct. Eng., 121(7), 1069-1078.

Meier, U., Triantafillou, T.C., and Deskovic, N. (1995b). "Innovative design of FRP combined with concrete: long-term behaviour." J. Struct. Eng., 121(7), 1079-1089.

Menzel, C.A., and Woods, W.M. (1952). "An investigation of bond, anchorage, and related factors in reinforced concrete beams." Bulletin No. 42, Research Dept., Research and Development Labs, Portland Cement Assn..

Middleton, C. R. (2004). "Bridge Management and Assessment in the UK." Proceedings of Austroads 5th Bridge Conference, 16pp.

Mofidi, A., and Chaallal, O. (2011). "Shear strengthening of RC beams with externally

bonded FRP composites: Effect of strip-width-to-strip-spacing ratio.” J. Compos. Constr., 15(5), 732-742.

Mofidi, A., Chaallal, O., Benmokrane, B., and Neale, K. (2012). "Experimental Tests and Design Model for RC Beams Strengthened in Shear Using the Embedded Through-Section FRP Method." J. Compos. Constr., 540-550.

Mofidi, A., Chaallal, O., Benmokrane, B., and Neale, K. (2012b). “Performance of end-anchorage systems for RC beams strengthened in shear with epoxy-bonded FRP.” J. Compos. Constr., 16(3), 322-331.

Montero, A., Ocariz, I.S, Lopez, I., Venegas, P., Gomez, J. and Zubia, J. (2011). “Fiber bragg gratings, IT Techniques and strain gauge validation for strain calculation on aged metal specimens.” Sensors, 2011, 11, 1088-1104.

Morinaga, S. (1996). “Remaining life of reinforced concrete structures after corrosion cracking.” Durability of Building Materials and Components, Edited by Sjostrom C, Published by E & FN Spon, 127-137.

Motra, H.B., Hildebrand, J., and Dimmig-Osburg, A. (2014). “Assessment of strain measurement techniques to characterise mechanical properties of structural steel.” Engineering Science and Technology, an International Journal, 17, 260-269.

Nilson, A.H. (1968). “Nonlinear analysis of reinforced concrete by the finite element method.” J. Am. Concrete Inst., 65(9), 757-766.

Park, R., and Paulary, T. (1975). “Reinfroced concrete structures.” John Wiley & Sons, New York, London, Sydney and Toronto.

Phillips, D.V., and Binsheng, Z. (1993). “Direct tension tests on notched and un-notched plain concrete specimens.” Magazine of Concrete Research, 45(162), 25-35.

Pillai, S.U., and Menon, D. (2003). “Reinforced concrete design.” 2nd ed. New Delhi, Tata McGraw-Hill Education Private Limited.

Potisuk, T., Higgins, C.C., Miller, T.H., and Yim, S.C. (2011). “Finite element analysis of reinforced concrete beams with corrosion subjected to shear.” Advances in Civil Engineering, 706803, 14 pages.

Qapo, M., Dirar, S., Yang, J., and Elshafie, M.Z.E.B. (2014). “Nonlinear finite element

modelling and parametric study of CFRP shear-strengthened prestressed concrete girders." Construction and Building Materials, 76(02), 245-255.

Rashid, Y.R. (1968). "Analysis of prestressed concrete pressure vessels." Nuclear Engng. And Design, 7(4), 334-344.

Rodríguez, J., Ortega, L., Casal, J. and Diez, J. (1996). "Corrosion reinforcement and service life of concrete structures." Durab. Build. Mater. Compon. 7(1), 117-126.

Rot, J.G. and Blaauwendraad, J. (1989). "Crack models for concrete: discrete or smeared? Fixed, multi-directional or rotating?" Heron, Rijswijk (ZH), The Netherlands.

Russo, G., and Puleri, G. (1997). "Shear links effectiveness in reinforced concrete beams under flexure and shear." ACI Structural Journal, 94(3), 227-238.

Russo, G., Venir, R., and Pauletta, M. (2005). "Reinforced concrete deep beams shear strength model and design formula." ACI Str J., 102(3), 429-437.

Saifullah, M. (1994). "Effect of reinforcement corrosion on bond strength in reinforced concrete." PhD thesis, the University of Birmingham, England.

Saifullah, M., and Clark, L.A. (1994). "Effect of corrosion rate on the bond strength of corroded reinforcement." Proc., 7th Int. Conf. on Corrosion and Corrosion Protection of Steel in Concrete, R. N. Swamy, ed. Sheffield Press, Sheffield, U.K., 591-602.

Sarsam K.F., and Phillips M.E. (1985). "The shear design of in-situ reinforced beam-column joints subjected to mono-tonic loading." Mag Concr Res 37(130):16–28

Sato, Y., Katsumata, H., and Kobatake, Y. (1997). "Shear strengthening of existing reinforced concrete beams by CFRP sheet." Non-Metallic (FRP) Reinforcement for Concrete Structures, Proceedings of the Third International Symposium, Sapporo, Japan, 507-513.

Sato, Y., and Vecchio, F. J. (2003). "Tension stiffening and crack formation in reinforced concrete members with fiber-reinforced polymer sheets." J. Struct. Eng., 129(6), 717–724.

Sayed, A.M., Wang, X., and Wu, Z. (2014). "Evaluation of effective strain of FRP sheets for shear strengthened RC beams." Proceedings of the 7th International Conference on FRP Composites in Civil Engineering, CICE

Scordelis, A.C., and Ngo, D. (1967). “Finite element analysis of reinforced concrete beams.” J. Am. Concrete Inst., 64(14), 152-163.

Shahawy, M., and Beitelman, T. (1999). “Static and fatigue performance of RC beams strengthened with CFRP laminates.” J.Struct. Eng., 125(6), 613-621.

Takahashi, E. (2013). “Shear failure behaviour of RC beam with corroded shear reinforcement.” 3rd International Conference, Sustainable Construction Materials and Technologies, Kyoto, Japan.

Taylor, H.P.J. (1972). “Shear Strength of Large Beams,” Journal of the Structural Division, ASCE, 98(11), 2473-2490.

Teng, J.G., Chen, J.F., Smith, S.T., and Lam, L. (2001). “FRP-strengthened RC structures.” John Wiley & Sons, LTD, West Sussex, England.

Thorenfeldt, E., Tomaszewicz, A., and Jensen, J.J. (1987). “Mechanical properties of high strength concrete and application in design.” Proceedings of the Symposium on Utilization of High Strength Concrete, Tapir, Trondheim, Norway, 149-159.

Triantafillou, T.C. (1998). “Shear strengthening of reinforced concrete beams using epoxy bonded FRP composites,” ACI Structural Journal, 95(2), 107-115.

Valerio, P., Ibell, T. J., and Darby, A. P. (2009). “Deep embedment of FRP for concrete shear strengthening.” Struct. Build., 162, 311-321.

Vecchio, F.J., and Collins, M.P. (1986). “The modified compression field theory for reinforced concrete elements subjected to shear.” ACI J., 83(2), 219-231.

Wang, P.T., Shah, S.P., and Naaman, A.E. (1978). “Stress-strain curves of normal and lightweight concrete in compression.” ACI Journal, 75(11), 603-611.

Xia, J., Jin, W. L., and Li, L. Y. (2011), “Shear performance of reinforced concrete beams with corroded shear links in chloride environment.” Corrosion Science, 53(2011) 1794-1805.

Xu, S.H., and Niu, D.T. (2004), “The shear behavior of corroded simply supported reinforced concrete beam.” J. Build. Struct. 25 (2004) 98–104.

Yoon, I.S., Copuroglu, O., and Park, K.B. (2007). “Effect of global climatic change on carbonation progress of concrete.” Atmos. Environ., 41(34), 7274–7285.

Yuan, Y.S., Ji, Y.S., and Shah, S.P. (2007). “Comparison of two accelerated

corrosion techniques for concrete structures.” ACI Struct. J., 104(3), 344-347.

Zakaria, M., Ueda, T., Wu, Z., and Meng, L. (2009). “Experimental investigation on shear cracking behavior in reinforced concrete beams with shear reinforcement.” J. Adv. Concr. Technol., 7(1), 79-96.

Zhang, N. and Tan, K.H. (2007). “Size effect in RC deep beams: experimental investigation and STM verification.” Journal of engineering structures, 29(12), 3241-3254.

Zhang, P.S., Lu, M., and Li, X.Y. (1995). “The mechanical behaviour of corroded bar.” Journal of Industrial